

UCSF

UC San Francisco Electronic Theses and Dissertations

Title

Identifying signaling and gene regulatory mechanisms of pathologic cardiac remodeling and heart failure pathogenesis

Permalink

<https://escholarship.org/uc/item/8nx083w3>

Author

Hsu, Austin

Publication Date

2022

Peer reviewed|Thesis/dissertation

Identifying signaling and gene regulatory mechanisms of pathologic cardiac remodeling and heart failure pathogenesis

by
Austin Hsu

DISSERTATION

Submitted in partial satisfaction of the requirements for degree of
DOCTOR OF PHILOSOPHY

in

Biomedical Sciences

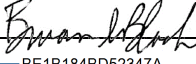
in the

GRADUATE DIVISION

of the

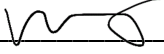
UNIVERSITY OF CALIFORNIA, SAN FRANCISCO

Approved:

DocuSigned by:

BE1B184BD52347A... Brian Black
Chair

DocuSigned by:

Benoit Bruneau

DocuSigned by:

500675FD24754FC... Biao Wang

Committee Members

Copyright 2022

by

Austin Hsu

Identifying signaling and gene regulatory mechanisms of pathologic cardiac remodeling and heart failure pathogenesis

Austin Hsu

Abstract

Heart failure is a highly prevalent and costly disease, accounting for the number one source of hospitalization and healthcare expenditures in the United States. This massive unmet medical need is further underscored by the fact that there have been no new classes of heart failure therapeutics developed in the past twenty years, highlighting the urgent need for novel biological insights to pave the groundwork for drug development. The majority of existing therapies are largely targeted at cell surface neurohormonal pathways, but fail to completely alter disease progression. Interdicting downstream signaling and gene regulatory pathways may provide an alternative and complementary therapeutic strategy. My dissertation explores the roles of two family of kinases, salt-inducible kinases (SIKs) and cyclin dependent kinases (CDKs), in the setting of heart failure pathogenesis. The data generated in this body of work implicate two salt-inducible kinase isoforms, SIK1 and SIK3, as positive and negative regulators of pathologic cardiac remodeling, respectively, that can be pharmacologically targeted with small molecule inhibitors. I also uncover a role for CDK7, 12 and 13 as positive regulators of pathologic transcription and demonstrate proof-of-concept targeting of these kinases as an effective strategy for attenuating maladaptive cardiac remodeling in heart failure. Collectively, these findings advance our fundamental understanding of mechanisms that underlie the pathogenesis of heart failure and establish novel therapeutic entry points that may be exploited for the development of drugs to treat human heart failure.

Table of Contents

| | |
|--|----|
| <i>Chapter 1: Introduction</i> | 1 |
| <i>Chapter 2: Salt-inducible kinase 1 maintains HDAC7 stability to promote pathologic cardiac remodeling</i> | 18 |
| Abstract | 19 |
| Background | 19 |
| Results..... | 21 |
| Discussion | 30 |
| Figures..... | 35 |
| Methods..... | 52 |
| References | 59 |
| <i>Chapter 3: Salt-inducible kinase 3 maintains ARHGAP21 stability to repress cardiac hypertrophy</i> | 63 |
| Abstract | 64 |
| Background | 64 |
| Results..... | 65 |
| Discussion | 71 |
| Figures..... | 75 |
| Methods..... | 80 |
| References | 88 |

| | |
|---|-----------|
| <i>Chapter 4: Targeting transcription in heart failure via inhibition of CDK7/12/13</i> | <i>91</i> |
| Abstract | 92 |
| Background | 92 |
| Results..... | 94 |
| Discussion | 102 |
| Figures..... | 107 |
| Methods..... | 123 |
| References | 136 |

List of Figures

| | |
|--|-----|
| Figure 2.1. Pan-SIK inhibitors attenuate hallmark features of cardiomyocyte hypertrophy in vitro | 35 |
| Figure 2.2. SIK1 is a positive regulator of cardiomyocyte hypertrophy | 37 |
| Figure 2.3. Global loss of SIK1 protects against pathologic cardiac remodeling in vivo | 38 |
| Figure 2.4. HDAC7 protein stability is dependent on SIK1 kinase activity | 39 |
| Figure 2.5. Loss of HDAC7 protects against pathologic cardiac remodeling in vitro | 41 |
| Figure 2.6. HDAC7 indirectly regulates c-Myc expression | 43 |
| Figure 2.7. Proposed working model | 45 |
| Supplemental Figure 2.1 | 46 |
| Supplemental Figure 2.2 | 48 |
| Supplemental Figure 2.3 | 50 |
| Supplemental Figure 2.4 | 51 |
| Figure 3.1. SIK3 represses pathologic cardiac remodeling in vitro and in vivo | 75 |
| Figure 3.2. Global transcriptional and proteomic profiling of Sik3 knockdown in NRVM | 76 |
| Figure 3.3. SIK3 regulates ARHGAP21 stability to repress pathologic cardiac remodeling | 77 |
| Figure 3.4. Nuclear enrichment of MRTF in siSik3 and siArhgap21 NRVM | 78 |
| Figure 4.1. CDK7/12/13 inhibition attenuates hallmark features of pathologic cardiomyocyte remodeling in vitro | 106 |
| Figure 4.2. THZ1 blocks stress-responsive gene programs and Pol II enrichment | |

| | |
|--|-----|
| in cultured cardiomyocytes | 108 |
| Figure 4.3. THZ1 ameliorates cardinal features of adverse cardiac remodeling and HFrEF pathogenesis in mice..... | 109 |
| Figure 4.4. THZ1 ameliorates specific pathological gene programs in diverse cardiac cellular compartments in failing mouse hearts | 111 |
| Supplementary Figure 4.1. Effects of THZ1 and THZ1-R | 113 |
| Supplementary Figure 4.2. YKL-1-116 inhibits agonist-induced hypertrophy in NRVM | 115 |
| Supplementary Figure 4.3. Effects of si-Cdk7, si-Cdk12, si-Cdk13, and si-TKD (triple knock down)..... | 116 |
| Supplementary Figure 4.4. Effects of THZ1 on hypertrophic marker gene expression in hiPSC-CM and physiological parameters in mice..... | 118 |
| Supplementary Figure 4.5. THZ1 inhibits specific gene programs in the adult mouse heart | 120 |
| Supplementary Figure 4.6. Differential gene expression from bulk RNA-seq for TAC vs. sham conditions, binned into indicated cellular compartments | 121 |

Chapter 1: Introduction

Heart Failure

Heart failure is a highly prevalent and lethal disease that carries an average 5-year mortality rate of ~40%¹, reflecting an incomplete understanding of the molecular pathogenesis of this disease and an urgent need for novel therapeutic strategies. Heart failure is characterized by a progressive interplay of structural and functional perturbations that ultimately render the heart unable to adequately pump blood to the rest of the body². Existing therapies have largely targeted cell surface neurohormonal pathways (e.g. inhibition of beta adrenergic and angiotensin signaling), which often fail to completely alter disease progression. In many cases, patients are refractory to current therapies and are treated using palliative measures as they ultimately progress to a premature death. In light of this massive unmet medical need, identification of novel molecular mechanisms underlying heart failure pathogenesis is desperately needed as a foundation for new therapeutic approaches.

Cardiac hypertrophy and remodeling

In response to diverse cardiac insults, the heart undergoes pathological remodeling, a process characterized by hypertrophic cardiomyocyte growth, fibrosis, inflammation, electrical remodeling, metabolic dysfunction and transcriptional activation of a maladaptive gene program that all converge on compromised cardiac function³.

The remarkable plasticity of the heart is well exemplified by its ability to undergo pathologic cardiac hypertrophy, a phenomenon in which cardiac myocytes in the heart initiate a maladaptive anabolic program in the absence of cell division – leading to gross enlargement of cellular mass and thickening of the myocardium⁴. Classically, cardiac

hypertrophy has been long considered as a beneficial and compensatory response to increased wall stress on the ventricular myocardium, following the Law of LaPlace⁵. However, a mounting body of literature derived from preclinical studies have demonstrated that inhibition of myocardial hypertrophy in setting of pressure overload in animal models is beneficial rather than detrimental^{6,7}. Even in the context of persistent stress, mitigation or prevention of hypertrophic growth is well-tolerated in these animal models and surprisingly does not lead to the development of ventricular dilation or reduced cardiac function. To further add to this evidence, clinical data of patients with heart failure⁸⁻¹⁰ have consistently concluded that left ventricular hypertrophy is associated with poorer outcomes in patients with an increased risk of heart failure and arrhythmias. These data suggest that cardiac hypertrophy may actually represent a maladaptive cellular stress response and underscore the need to better understand the underlying mechanisms that govern cardiomyocyte growth and plasticity. A stronger understanding of the fundamental molecular events that drive the onset of pathologic remodeling may uncover novel therapeutic entry points that can be leveraged for the development of urgently needed heart failure drugs. This work presented in this thesis sheds light on two family of kinases, salt inducible kinases (SIKs) and cyclin dependent kinases (CDKs), as potential therapeutic targets for the treatment of heart failure and regulators of the maladaptive cardiac stress response.

Class IIa histone deacetylases (HDACs)

A major molecular link between cytosolic signaling cascades and the nuclear gene control machinery in cardiac myocytes are the class IIa histone deacetylase (HDAC) family of co-

repressor proteins^{11,12}. The mammalian epigenome consists largely of two broad components: the structural features of the chromatin landscape and the molecules that alter these marks¹³. Histone deacetylases belong to the latter and are a class of enzymes that classically remove acetylation marks from histones to influence changes in chromatin accessibility and gene activation. These proteins are often divided into two distinct families: the (1) histone deacetylase family and the (2) sirtuin family¹⁴. The histone deacetylase family consists of class I, IIa, IIb, and IV HDACs and share a large degree of sequence homology within their conserved deacetylase domains. The sirtuin family proteins are demarcated as a unique subset of HDACs (class III) due to their dependence on nicotinamide adenine dinucleotide (NAD) as a cofactor to carry out their enzymatic function.

Class I HDACs, which represent HDAC1, 2, 3, and 8, have been shown experimentally to function as positive effectors of cardiac hypertrophy through regulation of fibrosis^{15,16}, inflammation¹⁷, and autophagy¹⁸. In contrast class IIa HDACs, which represent HDAC4, 5, 7, and 9, are largely considered to function as signal responsive co-repressors of cardiomyocyte transcription in the heart. Despite their nomenclature, class IIa HDACs have been demonstrated to exhibit very minimal enzymatic activity nearly 1000x less so than their class I HDAC counterparts. This discrepancy has been mapped to a significant functional amino acid change from the class I HDAC sequence: a tyrosine to histidine mutation located in the deacetylase domain of class IIa HDACs¹⁹. Class IIa HDACs are also further differentiated from class I HDACs due to the elongated N-terminal domains present in HDAC4, 5, 7, and 9. Rather than functioning through deacetylase activity, class

IIa HDACs are considered to function predominantly through protein-protein interactions facilitated by this elongated N-terminal region. One of the most well-studied interacting partners of class IIa HDACs in the heart is the transcription factor myocyte enhancer factor 2 (MEF2)¹². Under basal states in cardiac myocytes, class IIa HDACs are localized primarily to the nuclear compartment where they actively bind to and repress MEF2 transcriptional activity. In response to various neurohormonal or biomechanical stimuli, class IIa HDACs are phosphorylated on highly conserved and specific serine residues. This phosphorylation event creates a phospho-motif that is recognized by the nuclear export family of 14-3-3 proteins, which in turn bind to phosphorylated class IIa HDACs and facilitate their nuclear export into the cytoplasmic milieu. This event leads to functional de-repression of MEF2 and unbridled transcriptional activation of downstream MEF2 target genes, many of which have been extensively implicated as drivers of pathologic cardiac remodeling and hypertrophy.

The experimental evidence establishing this working model for class IIa HDACs was initially conceptualized from data derived from global mouse knock out studies of HDAC5 and 9²⁰ (HDAC4 and 7 global knockout mice are embryonic lethal^{21,22}). In these studies, HDAC5 and 9 knockout mice exhibited dramatic postnatal hypertrophic growth in the adult mouse heart, cementing the notion that class IIa HDACs function and negative regulators of cardiac growth in the mammalian heart. Conditional alleles of HDAC4 were later generated and yielded similar results²³. Despite the lack of experimental evidence implicating HDAC7 as a negative regulator of cardiac hypertrophy, it was largely assumed based on sequence homology and protein classification that it must function in a similar

MEF2 co-repressor manner. However, as discussed in chapter 2 of this thesis, our work demonstrated for the first time that HDAC7 functions uniquely as a positive driver of hypertrophic remodeling in the heart – highlighting a functional departure from the classical class IIa HDAC model that was originally built across the last 20 years of experimental data.

Due to the unique manner in which class IIa HDACs function and the implications of their positive influence in promoting cardiac hypertrophy – these proteins represent attractive therapeutic targets for heart failure therapy. However, as their primary identified function relies on direct protein-protein interaction rather than enzymatic activity – this interface represents a challenging target to develop small molecule inhibitors for, as there are no deep hydrophobic binding pockets that are amenable for targeting. Therefore, identification of upstream kinases that control the nuclear/cytoplasmic shuttling of these class IIa HDACs represent novel targets for therapeutic consideration and may expand our ability to therapeutically manipulate nuclear gene control pathways in cardiomyocytes. Chapters 2 and 3 of this thesis focuses on such a family of kinases called Salt-Inducible Kinases that had not yet been explored or implicated in the context of cardiac biology.

Salt-inducible kinases in cardiac biology

Salt-inducible kinases (SIKs) are serine/threonine kinases belonging to the AMP-activated protein kinase (AMPK) family of proteins²⁴. These kinases were first identified in 1999²⁵ after the first isoform, salt-inducible kinase 1, was cloned from the adrenal

glands of rats fed high-salt diets. Two additional mammalian isoforms have since been identified, salt-inducible kinase 2 and 3.

As part of the AMPK family, SIKs retain several similar features to other AMPK-related kinases including an N-terminal serine/threonine kinase domain and a ubiquitin associated domain²⁴. The SIK consensus substrate motif (LX(R/K/H)(S/T)XSXXXL) is also remarkably similar to that of AMPK ((L/M/I)X(R/K/H)XXSXXX(L/V/I/F))²⁶, yet SIKs have been demonstrated to phosphorylate unique substrates that are not known to be direct targets of AMPK signaling (CRTC/CREB, PME-1, HDACs)²⁷⁻²⁹.

SIKs are thought to be subject to multiple layers of regulation, including phosphorylation and spatial localization. Similar to AMPK, SIKs have been demonstrated to be direct targets of Liver Kinase B1 (LKB1) signaling³⁰. LKB1 can phosphorylate SIKs on their T-loop domains, leading to SIK activation. However, it is unclear whether this phosphorylation event by LKB1 is necessary for SIK activity, as multiple SIK isoforms have been demonstrated to harbor autophosphorylation activity independent of LKB1 signaling. SIKs are also subject to regulation by calcium/calmodulin dependent kinase (CaMK)^{31,32} and protein kinase A (PKA)³³. Phosphorylation of SIKs by CaMK similarly leads to kinase activation, however, phosphorylation by protein kinase A has been demonstrated to lead to repression of SIK activity. PKA phosphorylation of SIKs results in phospho-motifs that are recognized by the 14-3-3 nuclear export family of proteins. When bound to 14-3-3, SIKs are rendered inactive and shuttled into the cytoplasmic space.

It is becoming increasingly appreciated that this family of relatively understudied kinases harbors multifaceted and pleiotropic functions across many cellular and biological processes. Several SIK targets have been identified to date, including proteins involved in various cellular processes such as metabolism, cell growth, inflammation, and gene regulation. Among these targets include CREB, CRTC, HDACs, SREBP1-c, and p300^{27,28,34,35}.

The role that SIKs can play as class IIa HDAC kinases was intriguing, as this phenomenon had been previously demonstrated in the context of the drosophila fat body²⁷, but SIKs had not yet been shown to play any functional role in the mammalian heart. Chapters 2 and 3 of this thesis establish the first known roles of SIK1 and SIK3 in cardiac myocytes, demonstrating that these kinases act as positive and negative regulators of pathologic cardiac remodeling, respectively.

Transcription in heart failure

In addition to salt-inducible kinases, a portion of this thesis focuses on kinases involved in gene activation and transcription in heart failure. Chapter 4 focuses on how targeting a subset of cyclin dependent kinases (CDK) involved in RNA polymerase II initiation can confer protection against the establishment of heart failure.

For pathologic hypertrophy of the heart to occur, the organ must undergo a state of growth and remodeling that is supported by initiation of an anabolic cellular program³. As part of this process, there is a detectable increase in transcriptional activity that is required to

support the dramatic cellular plasticity and remodeling exhibited by cardiac myocytes. Concordant with this notion, in human patient samples derived from patients with heart failure, there are higher detectable levels of phosphorylated RNA polymerase II^{36,37} – a proxy measurement that is suggestive of greater transcriptional activity.

The process of transcription can be broken down into three broad phases: initiation, elongation, and termination. The progression and transition from one phase of transcription to the next is a highly regulated process facilitated in large part by phosphorylation of the C-terminal domain (CTD) of Rpb1³⁸, the largest subunit of RNA pol II. The RNA Pol II CTD consists of a unique heptapeptide repeat of the sequence Tyr-Ser-Pro-Thr-Ser-Pro-Ser (Y₁S₂P₃T₄S₅P₆S₇)³⁹. Each of the three serine motifs present in the CTD have been demonstrated to be involved in regulating distinct phases of the mammalian transcription cycle, although serine 2 and 5 have been most extensively studied.

Initiation encompasses the first steps of transcription in which RNA pol II is properly loaded on to the respective regions of the genome and is poised to begin transcribing its target sequence. This step of initiation is often associated with phosphorylation of serine 5 and can be facilitated by the transcription factor IIH (TFIIH) complex. The core catalytic component of the TFIIH complex is CDK7^{40,41}, one of the kinases of focus in chapter 4 of this thesis. Elongation represents the next stage of this process in which RNA Pol II is allowed to processively transcribe across the gene body. Often after initiation, RNA pol II will transcribe for a brief period of time, prior to stalling. In the stage of promoter proximal

pausing, RNA pol II requires phosphorylation on serine 2 of the CTD to trigger productive elongation and release of RNA pol II from a paused state³⁸. Several CTD kinases have been demonstrated to play a role in this process, including CDK12⁴² – another kinase of focus in chapter 4. The final stage of transcription is coined termination, during which serine 5, but not serine 2, of the CTD is dephosphorylated by various phosphatases near the end of the transcription cycle.

The roles of transcriptional CDKs in the pathogenesis of heart failure and cardiac hypertrophy are not well understood. The most notable of study of CDKs in this process has focused on CDK9^{36,37}, the core catalytic component of the positive elongation factor B (PTEFB) complex that can facilitate RNA pol II serine 2 phosphorylation and subsequent productive elongation. In this study, the authors demonstrate that inhibition of CDK9 with a chemical inhibitor (DRB) or overexpression of a dominant negative CDK9 in cultured cardiomyocytes confers protection against neurohormonal agonist induced cardiac hypertrophy. These findings were quite striking and demonstrated for the first time, that inhibition of the transcriptional kinases could have beneficial effects on disease progression. However, a caveat associated with this study was the degree of off target effects associated with the DRB chemical inhibitor which was not uniquely specific to CDK9 activity, complicating the interpretation of the data. Due to the overlapping sequence homology among many CDKs, designing inhibitors specific to individual CDKs has historically been a challenging feat.

Recently, a small molecule inhibitor called THZ1⁴³ was developed that demonstrates unique specificity for a subset of CDKs (CDK7, 12 and 13). This probe leverages a unique accessible cysteine in the CTD of these kinases remote from the active site, allowing for increased specificity via allosteric covalent binding. The development of this probe permitted a unique exploration into pharmacologically targeting specific RNA Pol II CTD kinases during heart failure pathogenesis to establish proof of concept that inhibition of transcription could be a viable approach for heart failure therapy. This study is discussed in further detail in Chapter 4 of this thesis.

Focus of Dissertation: Signaling and gene regulatory mechanisms of pathologic cardiac remodeling and heart failure pathogenesis.

My dissertation focuses on expanding our fundamental understanding of the molecular mechanisms that underlie heart failure pathogenesis. In chapter two, I present data that establishes a novel role for the salt-inducible kinase family of proteins in regulating cardiac remodeling and hypertrophy. Specifically, these data implicate SIK1 as a positive regulator of cardiac hypertrophy and establish an unexpected pro-hypertrophic role for the last uncharacterized class IIa HDAC in the heart, HDAC7. In chapter three, I expand on these initial studies of SIKs in the heart to demonstrate a role for another SIK isoform in the regulation of cardiac remodeling. These data implicate SIK3 as a negative regulator of pathologic remodeling, in part through the regulation of small Rho GTPase signaling and actin dynamics. In chapter four, I present data demonstrating that inhibition of transcription during early stages of heart failure pathogenesis potently attenuates disease establishment and progression, providing proof of concept that targeting transcription may be a viable approach for heart failure therapy.

References

1. Roger, V.L. Epidemiology of heart failure. *Circ Res* **113**, 646-659 (2013).
2. Jessup, M. & Brozena, S. Heart failure. *N Engl J Med* **348**, 2007-2018 (2003).
3. Hill, J.A. & Olson, E.N. Cardiac plasticity. *N Engl J Med* **358**, 1370-1380 (2008).
4. Ford, L.E. Heart size. *Circ Res* **39**, 297-303 (1976).
5. Grossman, W., Jones, D. & McLaurin, L.P. Wall stress and patterns of hypertrophy in the human left ventricle. *J Clin Invest* **56**, 56-64 (1975).
6. Esposito, G., *et al.* Genetic alterations that inhibit in vivo pressure-overload hypertrophy prevent cardiac dysfunction despite increased wall stress. *Circulation* **105**, 85-92 (2002).
7. Hill, J.A., *et al.* Targeted inhibition of calcineurin in pressure-overload cardiac hypertrophy. Preservation of systolic function. *J Biol Chem* **277**, 10251-10255 (2002).
8. Devereux, R.B., *et al.* Prognostic significance of left ventricular mass change during treatment of hypertension. *JAMA* **292**, 2350-2356 (2004).
9. Gardin, J.M. & Lauer, M.S. Left ventricular hypertrophy: the next treatable, silent killer? *JAMA* **292**, 2396-2398 (2004).
10. Levy, D., Garrison, R.J., Savage, D.D., Kannel, W.B. & Castelli, W.P. Prognostic implications of echocardiographically determined left ventricular mass in the Framingham Heart Study. *N Engl J Med* **322**, 1561-1566 (1990).
11. Grozinger, C.M. & Schreiber, S.L. Regulation of histone deacetylase 4 and 5 and transcriptional activity by 14-3-3-dependent cellular localization. *Proc Natl Acad Sci U S A* **97**, 7835-7840 (2000).

12. Zhang, C.L., *et al.* Class II histone deacetylases act as signal-responsive repressors of cardiac hypertrophy. *Cell* **110**, 479-488 (2002).
13. Rosa-Garrido, M., Chapski, D.J. & Vondriska, T.M. Epigenomes in Cardiovascular Disease. *Circ Res* **122**, 1586-1607 (2018).
14. Yang, X.J. & Gregoire, S. Class II histone deacetylases: from sequence to function, regulation, and clinical implication. *Mol Cell Biol* **25**, 2873-2884 (2005).
15. Williams, S.M., *et al.* Class I HDACs regulate angiotensin II-dependent cardiac fibrosis via fibroblasts and circulating fibrocytes. *J Mol Cell Cardiol* **67**, 112-125 (2014).
16. Iyer, A., *et al.* Antifibrotic activity of an inhibitor of histone deacetylases in DOCA-salt hypertensive rats. *Br J Pharmacol* **159**, 1408-1417 (2010).
17. Cardinale, J.P., *et al.* HDAC inhibition attenuates inflammatory, hypertrophic, and hypertensive responses in spontaneously hypertensive rats. *Hypertension* **56**, 437-444 (2010).
18. Cao, D.J., *et al.* Histone deacetylase (HDAC) inhibitors attenuate cardiac hypertrophy by suppressing autophagy. *Proc Natl Acad Sci U S A* **108**, 4123-4128 (2011).
19. Lahm, A., *et al.* Unraveling the hidden catalytic activity of vertebrate class IIa histone deacetylases. *Proc Natl Acad Sci U S A* **104**, 17335-17340 (2007).
20. Chang, S., *et al.* Histone deacetylases 5 and 9 govern responsiveness of the heart to a subset of stress signals and play redundant roles in heart development. *Mol Cell Biol* **24**, 8467-8476 (2004).
21. Backs, J., Song, K., Bezprozvannaya, S., Chang, S. & Olson, E.N. CaM kinase II selectively signals to histone deacetylase 4 during cardiomyocyte hypertrophy. *J Clin Invest* **116**, 1853-1864 (2006).

22. Chang, S., *et al.* Histone deacetylase 7 maintains vascular integrity by repressing matrix metalloproteinase 10. *Cell* **126**, 321-334 (2006).
23. Lehmann, L.H., *et al.* A proteolytic fragment of histone deacetylase 4 protects the heart from failure by regulating the hexosamine biosynthetic pathway. *Nat Med* **24**, 62-72 (2018).
24. Wein, M.N., Foretz, M., Fisher, D.E., Xavier, R.J. & Kronenberg, H.M. Salt-Inducible Kinases: Physiology, Regulation by cAMP, and Therapeutic Potential. *Trends Endocrinol Metab* **29**, 723-735 (2018).
25. Wang, Z., Takemori, H., Halder, S.K., Nonaka, Y. & Okamoto, M. Cloning of a novel kinase (SIK) of the SNF1/AMPK family from high salt diet-treated rat adrenal. *FEBS Lett* **453**, 135-139 (1999).
26. Kim, M.J., *et al.* Salt-Inducible Kinase 1 Terminates cAMP Signaling by an Evolutionarily Conserved Negative-Feedback Loop in beta-Cells. *Diabetes* **64**, 3189-3202 (2015).
27. Wang, B., *et al.* A hormone-dependent module regulating energy balance. *Cell* **145**, 596-606 (2011).
28. Berdeaux, R., *et al.* SIK1 is a class II HDAC kinase that promotes survival of skeletal myocytes. *Nat Med* **13**, 597-603 (2007).
29. Sjostrom, M., *et al.* SIK1 is part of a cell sodium-sensing network that regulates active sodium transport through a calcium-dependent process. *Proc Natl Acad Sci U S A* **104**, 16922-16927 (2007).
30. Patel, K., *et al.* The LKB1-salt-inducible kinase pathway functions as a key gluconeogenic suppressor in the liver. *Nat Commun* **5**, 4535 (2014).

31. Sakamoto, K., Bultot, L. & Goransson, O. The Salt-Inducible Kinases: Emerging Metabolic Regulators. *Trends Endocrinol Metab* **29**, 827-840 (2018).
32. Bright, N.J., Thornton, C. & Carling, D. The regulation and function of mammalian AMPK-related kinases. *Acta Physiol (Oxf)* **196**, 15-26 (2009).
33. Katoh, Y., *et al.* Salt-inducible kinase (SIK) isoforms: their involvement in steroidogenesis and adipogenesis. *Mol Cell Endocrinol* **217**, 109-112 (2004).
34. Jagannath, A., *et al.* The CRTCL1-SIK1 pathway regulates entrainment of the circadian clock. *Cell* **154**, 1100-1111 (2013).
35. Zhang, Z.N., *et al.* SIK2 regulates fasting-induced PPARalpha activity and ketogenesis through p300. *Sci Rep* **6**, 23317 (2016).
36. Sano, M., *et al.* Activation and function of cyclin T-Cdk9 (positive transcription elongation factor-b) in cardiac muscle-cell hypertrophy. *Nat Med* **8**, 1310-1317 (2002).
37. Sano, M., *et al.* Activation of cardiac Cdk9 represses PGC-1 and confers a predisposition to heart failure. *EMBO J* **23**, 3559-3569 (2004).
38. Phatnani, H.P. & Greenleaf, A.L. Phosphorylation and functions of the RNA polymerase II CTD. *Genes Dev* **20**, 2922-2936 (2006).
39. Corden, J.L. Tails of RNA polymerase II. *Trends Biochem Sci* **15**, 383-387 (1990).
40. Glover-Cutter, K., *et al.* TFIIH-associated Cdk7 kinase functions in phosphorylation of C-terminal domain Ser7 residues, promoter-proximal pausing, and termination by RNA polymerase II. *Mol Cell Biol* **29**, 5455-5464 (2009).
41. Shiekhattar, R., *et al.* Cdk-activating kinase complex is a component of human transcription factor TFIIH. *Nature* **374**, 283-287 (1995).

42. Tellier, M., *et al.* CDK12 globally stimulates RNA polymerase II transcription elongation and carboxyl-terminal domain phosphorylation. *Nucleic Acids Res* **48**, 7712-7727 (2020).
43. Kwiatkowski, N., *et al.* Targeting transcription regulation in cancer with a covalent CDK7 inhibitor. *Nature* (2014).

**Chapter 2: Salt-inducible kinase 1 maintains HDAC7 stability to promote
pathologic cardiac remodeling**

Abstract

Salt inducible kinases (SIKs) are key regulators of cellular metabolism and growth, but their role in cardiomyocyte plasticity and heart failure pathogenesis remains unknown. Here, we showed that loss of SIK1 kinase activity protected against adverse cardiac remodeling and heart failure pathogenesis in rodent models and human iPSC-derived cardiomyocytes. We found that SIK1 phosphorylated and stabilized histone deacetylase 7 (HDAC7) protein during cardiac stress, an event that is required for pathologic cardiomyocyte remodeling. Gain- and loss-of-function studies of HDAC7 in cultured cardiomyocytes implicated HDAC7 as a pro-hypertrophic signaling effector that can induce *c-Myc* expression, indicating a functional departure from the canonical MEF2 co-repressor function of class IIa HDACs. Taken together, our findings reveal what we believe to be a previously unrecognized role for a SIK1-HDAC7 axis in regulating cardiac stress responses and implicate this pathway as a potential target in human heart failure.

Background

In response to cardiac insults, the heart undergoes stress-dependent pathologic remodeling, a process that features hypertrophic cardiomyocyte growth and transcriptional activation of a gene program that can chronically compromise cardiac function (1). A major regulator of stimulus-coupled transcription in cardiomyocytes is the class IIa histone deacetylase (HDAC) protein family (HDAC4, 5, 7, 9), which lack significant catalytic activity and are generally thought to function as potent allosteric co-repressors of MEF2 transcriptional activity (2). In response to stress signals, a subset of intracellular kinases directly interact with class IIa HDACs and phosphorylate them on

specific, conserved serine residues – an event that promotes nuclear export of these HDACs and consequent de-repression of MEF2 transcriptional function. Consistent with this model, genetic deficiency of HDAC4, 5 or 9 is each associated with excessive myocardial MEF2 activity and heart failure in mice (2-4). In this manner, phosphorylation of class IIa HDACs by specific kinases (e.g., CaMKII, PKD) functions as a signal responsive mechanism that directly couples cytosolic stress signaling cascades with the nuclear gene control machinery. Therefore, identification of upstream kinases that regulate HDACs in the heart is essential for our mechanistic understanding of cardiac stress responses, knowledge that may inform novel therapeutic strategies for human heart failure.

Salt Inducible Kinases (SIKs; SIK1, 2, 3 in mammals) are a family of serine/threonine protein kinases that have been shown to regulate skeletal muscle homeostasis and the hepatic fasting response by modulating HDAC4 and HDAC5 function (5, 6). However, the role of SIKs in the heart is largely unknown. In this study, we establish SIK1 as an essential positive regulator of pathologic cardiac remodeling. Leveraging complementary gene-specific siRNA knockdown and chemical inhibition approaches, we demonstrate that inhibition of SIK1 blocks cardinal features of pathologic remodeling in vitro. Similarly, global SIK1 deficient mice are protected from pressure overload induced heart failure. Mechanistically, we uncover HDAC7 as a major downstream target of SIK1 phosphorylation and demonstrate that loss of this phosphorylation event leads to proteasome-mediated degradation of HDAC7. Specific siRNA mediated knockdown of *Hdac7* in cultured cardiomyocytes reveals that it functions as a positive regulator of

cardiomyocyte hypertrophy and stress-gene transactivation. This mechanism represents a function that is distinct from that of HDAC4, 5 or 9, which act as MEF2 co-repressors and negative regulators of cardiomyocyte hypertrophy and heart failure pathogenesis. In addition, we find that HDAC7 activates *c-Myc*, a well-established transcriptional driver of cardiomyocyte stress responses (7, 8), further supporting a distinct mechanism of action for HDAC7 compared to other class IIa HDACs. Taken together, these findings identify SIK1 as a critical effector of cardiomyocyte stress responses and heart failure pathogenesis and implicate HDAC7 as a major downstream target of SIK1 signaling during cardiomyocyte hypertrophy.

Results

Pan-SIK inhibition attenuates hallmark features of pathologic cardiomyocyte remodeling in vitro

To our knowledge, the role of SIKs in heart failure has not been previously explored. As SIKs have been implicated as a link between cytosolic signaling cascades and the nuclear gene control machinery in hepatocyte metabolic adaptation (6), we hypothesized that this family of kinases might regulate cardiomyocyte plasticity during heart failure related stress. We began by testing whether broad inhibition of all three SIK isoforms would have any effect on the cardiomyocyte stress response. We leveraged the neonatal rat ventricular myocyte (NRVM) cell culture model, which has been well-established to mount a stereotypic response to hypertrophic stimuli such as phenylephrine (PE), featuring an increase in cell size (hypertrophy) and activation of a heart failure related gene expression program (9). We tested the effect of two structurally distinct, potent, and relatively specific

chemical inhibitors of the SIK family (HG-09-091 and YKL-05-099) (10) on NRVMs treated with and without PE. Treatment with either SIK inhibitor potently attenuated hallmark features of pathologic cardiomyocyte remodeling in a dose-dependent manner, including cellular hypertrophy (Figure 2.1, A and B) and induction of canonical heart failure associated marker genes such as *Nppa*, *Nppb*, *Ctgf*, and *Il6* (11, 12) (Figure 2.1C and Supplemental Figure 2.1A). The effects of these inhibitors on cardiomyocyte hypertrophy and gene expression in the baseline state are shown in Supplemental Figure 2.1, B-E. To provide human relevance to our findings, we tested the effects of SIK inhibitors in an established model of Endothelin-1 (ET-1) induced hypertrophy in human iPSC-derived cardiomyocytes (13). Treatment with either SIK inhibitor suppressed ET-1 induced cellular hypertrophy, upregulation of *NPPB* mRNA, and secretion of proBNP protein into the media, in a dose-dependent manner (Figure 2.1, D-F).

SIK1 is a positive regulator of pathologic cardiomyocyte remodeling in vitro

Pan-SIK chemical probes, such as YKL-05-099, also have activity against Src kinases and cannot discriminate which SIK isoform is critical for driving cardiomyocyte hypertrophy (10) . We therefore used gene-specific siRNAs in our NRVM system to assess which SIK isoforms might be mediating the pro-hypertrophic effect. Three mammalian SIK isoforms have been identified to date: SIK1, 2, and 3 (14). In NRVM, we were unable to detect *Sik2* transcripts by qRT-PCR at baseline or after PE stimulation. *Sik1* transcripts were readily detected and strongly induced by PE stimulation, suggesting that SIK1 may play a role in the early cardiac stress response. *Sik3* transcripts were also detected in NRVM but did not change with PE stimulation (Figure 2.2A). We used specific

siRNA probes to knockdown *Sik1* or *Sik3* in NRVM and assayed for the effect of knockdown on cardiac hypertrophy. *Sik1* knockdown had no appreciable effect on cardiac myocytes under basal conditions, but potently attenuated PE-induced hypertrophy and gene induction (Figure 2.2, B-D and Supplemental Figure 2.2, A and B). In contrast, knockdown of *Sik3* induced spontaneous hypertrophy and activation of heart failure associated genes under basal conditions and further exacerbated the PE-induced stress response (Figure 2.2, B, C, and E, Supplemental Figure 2.2, A and B, and Supplemental Figure 2.4D). Taken together, these data demonstrate that SIK1 is the specific isoform that positively regulates cardiomyocyte hypertrophy and stress gene activation.

Global loss of SIK1 protects against pathologic cardiac remodeling in vivo

Prompted by these observations in cultured NRVM, we hypothesized that SIK1 would also be required for pathologic cardiac remodeling and heart failure pathogenesis in vivo. Global *Sik1*^{-/-} mice (15) and wild-type littermate controls were subject to cardiac pressure overload by transverse aortic constriction (TAC) (16). After 6 weeks of TAC, *Sik1*^{-/-} mice had less cardiomegaly and cardiac hypertrophy (Figure 2.3, A and B and Supplemental Figure 2.2C). Serial echocardiography demonstrated that *Sik1* deficiency attenuated the progressive decline in LV systolic dysfunction seen in wild-type mice (Figure 2.3C). In addition, *Sik1*^{-/-} mice exhibited attenuated features of heart failure, such as reduced LV fibrosis (Figure 2.3D), reduced cardiomyocyte hypertrophy (Figure 2.3E), and blunted induction of stereotypical heart failure related genes (Figure 2.3F). *Sik1* deficiency did not alter cardiac structure or function in the sham treated group (Figure 2.3C). These data

implicate SIK1 as a critical regulator of stress-induced pathologic cardiac remodeling and heart failure progression in vivo.

HDAC7 stability is dependent on SIK1 kinase activity

In other cellular contexts, SIK1 has been shown to phosphorylate and regulate HDAC4 and HDAC5 (5, 6). To test whether SIK1 targets class IIa HDACs in cardiomyocytes, we harvested whole cell lysates from NRVM treated with *Sik1* siRNA +/- PE and performed western blot analysis using a phospho-specific antibody that can discriminate orthologous phosphorylation status of HDAC4 (serine 246), HDAC5 (serine 259), and HDAC7 (serine 155). *Sik1* knockdown did not significantly affect phospho-HDAC4 or phospho-HDAC5 abundance in NRVM (Figure 2.4A). However, phospho-HDAC7 abundance was significantly depleted with *Sik1* knockdown. We assessed for total protein abundance of class IIa HDAC isoforms and found that total HDAC7 protein abundance was robustly and specifically decreased with *Sik1* knockdown, implicating an unexpected role for SIK1 in maintaining total HDAC7 protein concentration (Figure 2.4A). *Hdac7* transcript levels remained unchanged in the setting of *Sik1* knockdown (Figure 2.4B), indicating that SIK1-mediated regulation of HDAC7 occurs in a post-transcriptional manner. To test whether this mode of regulation is dependent on the intrinsic kinase activity of SIK1, we performed western blot analysis on NRVM treated with pan-SIK chemical inhibitors HG-09-091 and YKL-05-099. Both inhibitors phenocopied the effects of the *Sik1* siRNA on HDAC7, depleting total and phosphorylated HDAC7 abundance under both baseline and PE-stimulated conditions (Figure 2.4, C and D). Furthermore, western blot analysis on cardiac tissue samples from global *Sik1*^{-/-} mice also revealed decreased total and phospho-

HDAC7 protein at baseline and post-TAC (Figure 2.4E), demonstrating that this SIK1-HDAC7 axis is preserved in vivo and across species. The effect of SIK1 deficiency on HDAC7 protein abundance was less pronounced in the TAC treated group compared to the sham group, suggesting that pressure overload may induce the expression or activity of additional kinases or alternative mechanisms that can modulate HDAC7 stability in the adult mouse heart.

To further test whether this effect was due to a direct kinase-substrate interaction between SIK1 and HDAC7, we performed an in vitro kinase assay using recombinant SIK1 and HDAC7 protein. As expected, HDAC7 alone did not exhibit basal phosphorylation signal. However, addition of both SIK1 and HDAC7 induced phosphorylation of Ser155, which was lost upon addition of the SIK inhibitor YKL-05-099 (Figure 2.4F). We also found that SIK1 could phosphorylate Ser318 and Ser488 in this assay, two residues that have been implicated in the interaction of HDAC7 with 14-3-3 (Supplemental Figure 2.2D) (17). This evidence supporting a direct kinase-substrate interaction led us to hypothesize that loss of SIK1 kinase activity decreases phosphorylation of HDAC7, leading to proteasome-mediated HDAC7 degradation. Consistent with this hypothesis, treating NRVM with the proteasome inhibitor bortezomib rescued the SIK-inhibitor dependent depletion of HDAC7 protein (Figure 2.4G). In addition, treatment of NRVM with the SIK inhibitor YKL-05-099 increased the ratio of ubiquitinated-HDAC7 to total HDAC7 (Supplemental Figure 2.4A and B). Bortezomib also led to a relative increase in the ubiquitinated-HDAC7 to total HDAC7 ratio compared to baseline, although this ratio was not further augmented by YKL-05-099 co-treatment, possibly because potent proteasome inhibition by itself may

lead to saturating levels of ubiquitinated-HDAC7 in this context (Supplemental Figure 2.4A and B). Additionally, mutagenesis of serine 155 to alanine on HDAC7 diminished the stabilizing effects of SIK1 (Supplemental Figure 2.2E), specifically implicating Ser155 as an important residue in HDAC7 stabilization. Previous work has shown that HDAC7 can be stabilized by 14-3-3 proteins in human embryonic kidney (HEK) 293 cells (18). To test whether 14-3-3 protein also participates in HDAC7 stabilization in cardiomyocytes, we infected NRVM with adenovirus expressing full length 14-3-3 followed by treatment with SIK inhibitor YKL-05-099. Overexpression of 14-3-3 increased HDAC7 protein abundance compared to empty virus infected control (Supplemental Figure 2.4C). However, this effect was lost upon addition of the SIK inhibitor YKL-05-099, suggesting that 14-3-3 proteins may play a role in the stabilization of HDAC7, but are dependent on SIK activity to exert their stabilizing effect. Taken together, these results demonstrate that HDAC7 protein abundance in cardiomyocytes is dependent on SIK1 kinase activity and support that direct phosphorylation of HDAC7 by SIK1 is critical for HDAC7 stability.

Loss of HDAC7 protects against pathologic cardiac remodeling

Previous studies of class IIa HDACs in the heart have demonstrated roles for HDAC4, 5 and 9 as MEF2 co-repressors that function as negative regulators of cardiomyocyte hypertrophy and the transcriptional response to cardiac stress (2-4). However, to our knowledge, the role of HDAC7 in the heart has not been previously explored. As our data shows that SIK1 is a positive regulator of pathologic cardiac remodeling and can stabilize HDAC7, we hypothesized that HDAC7 may also function as a positive regulator of this response, suggesting a role that deviates from the other class IIa HDAC isoforms. We

found that siRNA-mediated knockdown of *Hdac7* in NRVM robustly attenuated PE-induced cardiac hypertrophy and induction of canonical heart failure related genes (Figure 2.5, A-C). In contrast, siRNA-mediated knockdown of *Hdac5* led to a robust induction of *Nppa* and *Nppb* transcripts at baseline and after PE stimulation (Figure 2.5C), consistent with the role of HDAC5 as a transcriptional co-repressor. Transduction of a MEF2 reporter construct into NRVM revealed that *Hdac7* knockdown had no effect on MEF2 transcriptional activity while *Hdac5* knockdown increased MEF2 activity (Figure 2.5D and Supplemental Figure 2.4E and F), further supporting that HDAC7 functions differently than other class IIa HDACs.

We have shown that SIK1 inhibition attenuates cardiomyocyte hypertrophy and heart failure pathogenesis, and is associated with loss of HDAC7 protein abundance. We have also demonstrated that HDAC7 is a positive regulator of cardiomyocyte hypertrophy. To establish a causal link between SIK1 and HDAC7, we tested whether reconstitution of HDAC7 in the setting of SIK1 inhibition would blunt the anti-hypertrophic effects of SIK1 inhibition. We generated adenoviruses expressing GFP-HDAC7 (Ad-HDAC7) or GFP alone (Ad-GFP) and infected NRVM followed by treatment with or without SIK inhibitors and PE. Under non-stimulated conditions, overexpression of HDAC7 was sufficient to induce cardiomyocyte hypertrophy and *Nppa*, *Nppb*, and *Myh7* expression compared to Ad-GFP control (Figure 2.5, E-G). SIK inhibition inhibited cardiomyocyte hypertrophy (Figure 2.5, E-G) and depleted HDAC7 protein abundance (Supplemental Figure 2.3A). Reconstitution of HDAC7 (Western blot of HDAC7 reconstitution shown in Supplemental Figure 2.3B) partially reversed the protective effects of SIK inhibition during PE-mediated

stress (Figures 2.5, E-G). To test the converse, we infected NRVM with an adenovirus expressing SIK1 followed by transfection of siRNA probes against *Hdac7*. Overexpression of SIK1 increased *Nppa* and *Nppb* expression in PE stimulated conditions, but had no appreciable effect at baseline. (Supplemental Figure 2.2, F and G). Knockdown of *Hdac7* robustly attenuated the effect of SIK1 overexpression (Supplemental Figure 2.2, F and G). These results support a model in which SIK1 promotes cardiomyocyte hypertrophy and stress-gene induction, in part, via activation of HDAC7.

HDAC7 indirectly regulates c-Myc expression

Our data show that HDAC7 is a pro-hypertrophic transcriptional regulator (Figure 2.5) and suggests that HDAC7 does not function as a MEF2 co-repressor (Figure 2.5D). These findings support the contention that HDAC7 functions in a manner that is different than other class IIa HDACs. Emerging studies have described non-canonical roles for HDAC7 in other biological contexts, including a role as an activator of *c-Myc* in cancer (19). Given the importance of *c-Myc* in establishing pathologic remodeling in the heart (7, 8, 20), we tested whether *c-Myc* expression was altered with HDAC7 perturbation in cardiomyocytes. Silencing of *Hdac7* led to a decrease in *c-Myc* RNA and robustly depleted C-MYC protein in NRVM (Figure 2.6, A and B). Conversely, overexpression of HDAC7 induced *c-Myc* expression at both the RNA and protein levels (Figure 2.6, C and D). Similarly, treatment with SIK inhibitor YKL-05-099, which robustly depletes HDAC7 (Figure 2.4D), led to a marked decrease in *c-Myc* mRNA and protein expression (Figure 2.6, E and F). Cardiac tissue samples from SIK1 KO mice also exhibited lower *c-Myc*

RNA and protein expression levels compared to WT control mice (Supplemental Figure 2.3, D and E).

To determine whether HDAC7 directly or indirectly regulates *c-Myc* expression, we first assessed the nuclear/cytoplasmic distribution of HDAC7 in NRVM. Other class IIa HDACs have been shown to shuttle between the nuclear and cytoplasmic compartments and it is thought that control of their spatial localization is a central mechanism for regulating their function. We performed nuclear/cytoplasmic fractionation on NRVM lysates treated with SIK inhibitor YKL-05-099 +/- PE stimulation. Under all conditions, total and phosphorylated HDAC7 protein was found exclusively in the cytoplasmic fraction and was notably absent in the nuclear fraction (Figure 2.6G). Treatment of NRVM with the proteasome inhibitor bortezomib, which causes accumulation of HDAC7 protein, also did not reveal any detectable levels of HDAC7 protein in the nuclear fraction (Supplemental Figure 2.3C). In contrast, HDAC5 protein was detected in both nuclear and cytoplasmic fractions as previously reported (Figure 2.6G and Supplemental Figure 2.3C) (21). The lack of detectable HDAC7 in the nuclear fraction of NRVM indicates that HDAC7 is unlikely to regulate *c-Myc* expression via direct enrichment on DNA regulatory elements in cardiomyocytes.

Overexpression of HDAC7 in NRVM induces hypertrophy and *c-Myc* expression (Figure 2.5E-G and Figure 2.6C and D). To test whether HDAC7-mediated hypertrophy is dependent on *c-Myc* induction, we infected NRVM with Ad-HDAC7 followed by transfection of siRNA probes against *c-Myc* (Supplemental Figure 2.3, F and G). *c-Myc*

knockdown had no effect on cell size in empty virus infected NRVM, but attenuated HDAC7 induced cardiomyocyte hypertrophy and *Nppa* and *Nppb* expression (Figure 2.6, H-J). Taken together, these data indicate that HDAC7 acts as a positive upstream regulator of C-MYC during cardiomyocyte hypertrophy, further suggesting that the SIK1-HDAC7 axis functions in a manner that is different from the signal-responsive MEF2 co-repressor role of related class IIa HDAC isoforms.

Discussion

Our results implicate the SIK family of kinases as key regulators of cardiac plasticity in rodent models and human cardiomyocytes, significantly expanding our fundamental understanding of how stress-signaling cascades are coupled to the cardiomyocyte gene regulatory machinery. In contrast to previously known cardiac class IIa HDAC kinases such as CaMKII and PKD, which function primarily via HDAC nuclear-cytoplasmic shuttling, we establish a unique role for SIK1 as a critical effector of HDAC7 stabilization. Our data demonstrates a mechanistic link between SIK1 and HDAC7, implicates this axis as part of a pro-hypertrophic signaling node, and provides new insights into the function of HDAC7 - one of the least well characterized HDAC family members in cardiac biology (Figure 2.7, summary diagram).

SIK1 mediates HDAC7 stability

Established cardiac class IIa HDAC kinases in the heart, such as CaMK and Protein Kinase C/D (21-23), directly phosphorylate class IIa HDACs, leading to their nuclear export and subsequent de-repression of MEF2 transcriptional activity. In contrast, our

data on SIK1 support a differentiated mode of regulation that uncovers a new layer of control at the level of HDAC7 protein stabilization. In the heart, SIK1-mediated stabilization of HDAC7 is robust and appears to be specific for HDAC7 over other class IIa family members. Why HDAC7 stability is particularly sensitive to SIK1 inhibition is unclear, especially in light of the fact that other class IIa HDAC kinases (CaMK, PKD) can phosphorylate similar epitopes. Previous studies have shown that CaMKII signals exclusively to HDAC4 through a unique CaMKII docking sequence present only on HDAC4 and is absent in other class IIa HDACs (23). It is possible that the specificity of SIK1 signaling could be achieved through a similar docking domain within HDAC7.

How exactly SIK1-mediated phosphorylation of HDAC7 promotes increased HDAC7 stability also remains unclear. Our data implicate Ser155 on HDAC7 as an important determinant of SIK1-mediated stabilization, although other serine residues may also play a role in this process. We speculate that phosphorylated HDAC7 may have increased affinity for binding to 14-3-3 proteins, protecting HDAC7 from targeted proteasomal degradation, as has been suggested from previous studies in HEK293 cells (18). In support of this mechanism, we find that overexpression of 14-3-3 in NRVM can increase HDAC7 protein abundance. Our observation that this stabilizing effect of 14-3-3 overexpression is abrogated by SIK inhibition suggests a model in which SIK-mediated phosphorylation of HDAC7 is a dominant trigger for protein stabilization, while 14-3-3 further facilitates the protection of HDAC7 from the protein degradation machinery. While our study identifies HDAC7 as an important downstream target of SIK1 activity, there are likely additional substrates of SIK1 signaling that play a role in cardiac remodeling. Future

studies leveraging unbiased approaches, such as phospho-proteomics, may identify additional downstream effectors of SIK1 signaling that participate in cardiac homeostasis and stress responses.

HDAC7 is a pro-hypertrophic HDAC

The contention that class IIa HDACs in the heart function primarily as transcriptional co-repressors of MEF2 are derived from studies focused exclusively on HDAC4, HDAC5, and HDAC9. This prior work has shown that loss of function of these HDACs leads to excessive MEF2 activity and heart failure (2, 3), consistent with the role of these HDAC isoforms as transcriptional repressors and negative regulators of cardiomyocyte hypertrophy. In contrast, the role of HDAC7 in the heart has been largely unexplored. Using cultured cardiomyocytes, we find that HDAC7 functions as a positive regulator of cardiomyocyte hypertrophy, suggesting major mechanistic differences with the other class IIa HDACs. Recent studies have demonstrated highly specific roles of HDAC4 signaling, including the identification of a proteolytically cleaved N-terminal fragment of HDAC4, suggesting that significant functional specificity exists even between proteins as closely related as HDAC4 and 5 (4, 24). Consistent with this deviation in function, we also find that HDAC7 can strongly induce *c-Myc* expression – a robust and established driver of stress-dependent cardiac gene expression and pathologic remodeling. Surprisingly, we find that HDAC7 resides exclusively in the cytoplasm of NRVM and is notably absent in the nuclear compartment. It will be important to understand the precise mechanisms by which HDAC7 regulates *c-Myc* expression, as such regulation is unlikely to involve direct enrichment of HDAC7 on *c-Myc* regulatory loci in cardiomyocytes. The absence of

detectable HDAC7 in the cardiomyocyte nucleus implicates that class IIa HDACs may have many functions outside of direct regulation of gene expression (19, 25-27). Further studies to explore the HDAC7-dependent transcriptome and protein interactome in cardiomyocytes will shed important light on the detailed mechanisms of HDAC7 function.

The role of SIK1 in non-myocyte cells

Our studies using chemical probes and siRNAs in cultured cardiomyocytes supports a cell-autonomous role for SIK1 in these tissues. While we have shown that SIK1 null mice are protected from pressure overload-induced heart failure, it remains possible that SIK1 expression in non-cardiomyocyte cell types are influencing the phenotype in vivo. Similar to our observations in cultured cardiomyocytes, we find that the hearts of SIK1 null mice are depleted in HDAC7 protein, implicating that the SIK1-HDAC7 axis in cardiomyocytes is also operative in vivo. Silencing of HDAC7 has also been shown to inhibit myofibroblast differentiation (28), suggesting that SIK1 expression in fibroblasts may also contribute to heart failure pathogenesis. While our current work establishes a role for SIKs in heart failure pathobiology, in the future it will be informative to annotate the role of SIK1 in other relevant cellular compartments that populate the stressed myocardium using a conditional gene-deletion approach.

In summary, we show that SIK1 is a previously unrecognized effector of stress-mediated hypertrophic remodeling and gene induction in rodent and human cardiomyocytes, in part through its ability to regulate HDAC7 protein stability. We establish a new role for HDAC7 as a pro-hypertrophic effector, a target of SIK1, and an upstream regulator of *c-Myc*

expression in cardiomyocytes, reflecting functions that are distinct from those of related class IIa HDAC family members. Our findings in rodent models and human iPSC-derived cardiomyocytes suggest that interdicting the SIK1-HDAC7 signaling cascade may be a therapeutic approach in human heart failure.

Figures

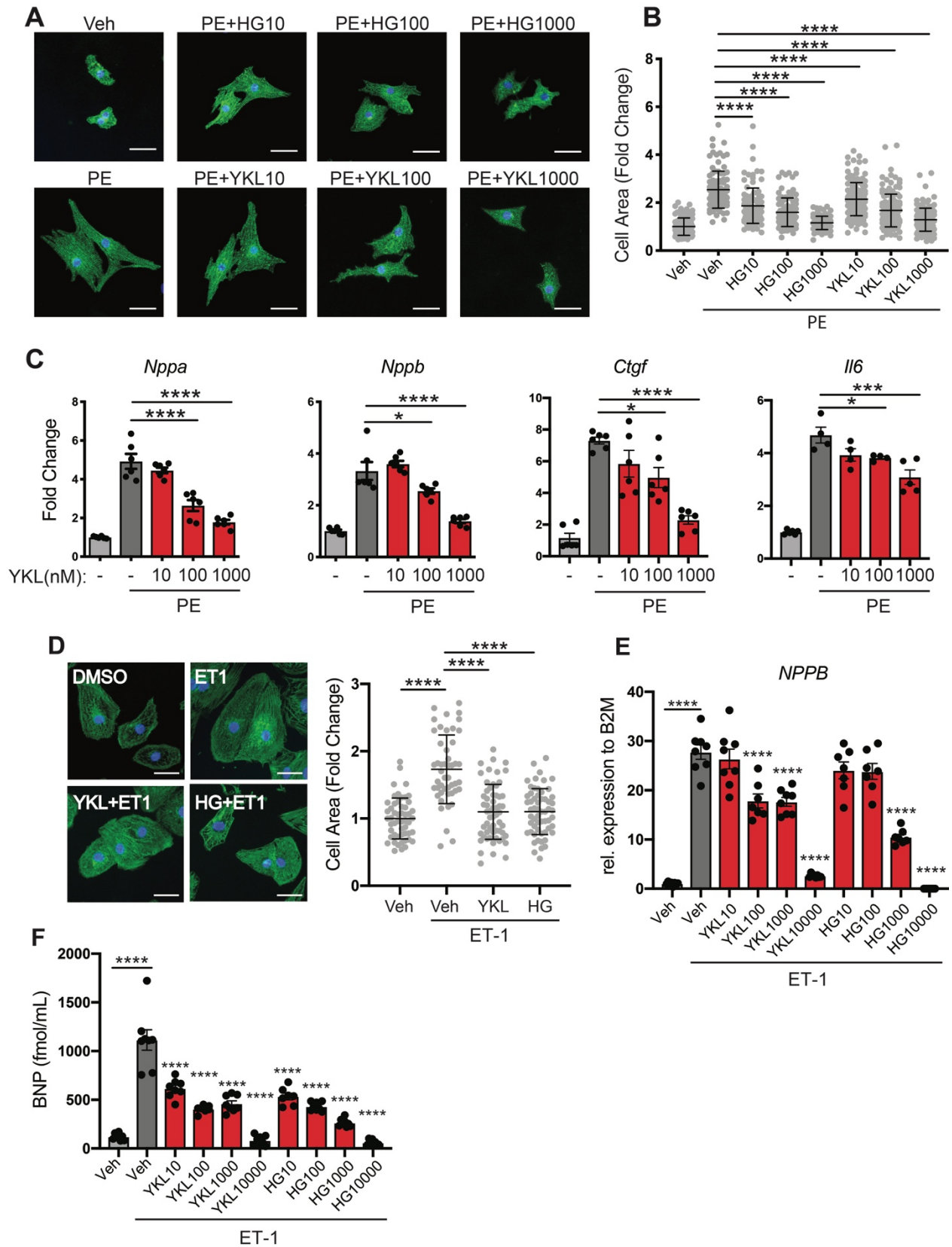


Figure 2.1. Pan-SIK inhibitors attenuate hallmark features of cardiomyocyte hypertrophy in vitro. (A) NRVM immunostained for α -actinin (green) and nuclei (blue) Scale = 40um. (B) Cell area of NRVM treated with 100uM phenylephrine (PE) for 48 hours \pm pan-SIK small molecule inhibitors, HG 9-91-01 (HG) and YKL-05-099 (YKL) (nM concentrations) (n=100-130). Bars designate mean \pm SD. (C) qRT-PCR expression for canonical heart failure associated genes. (n=4-6). (D) iPSC-cardiomyocytes (CM) immunostained for α -actinin (green) and nuclei (blue) Scale = 40um. (n=48-59). (E) qRT-PCR expression of *NPPB* in iPSC-CM. (n=7-8). (F) Elisa for proBNP protein secretion into culture medium of iPSC-CM. (n=7-8). Data are shown as means \pm SEM unless noted. *P<0.05, **P<0.01, ***P<0.001, ****P<0.0001 by one-way ANOVA with Tukey's multiple comparisons test.

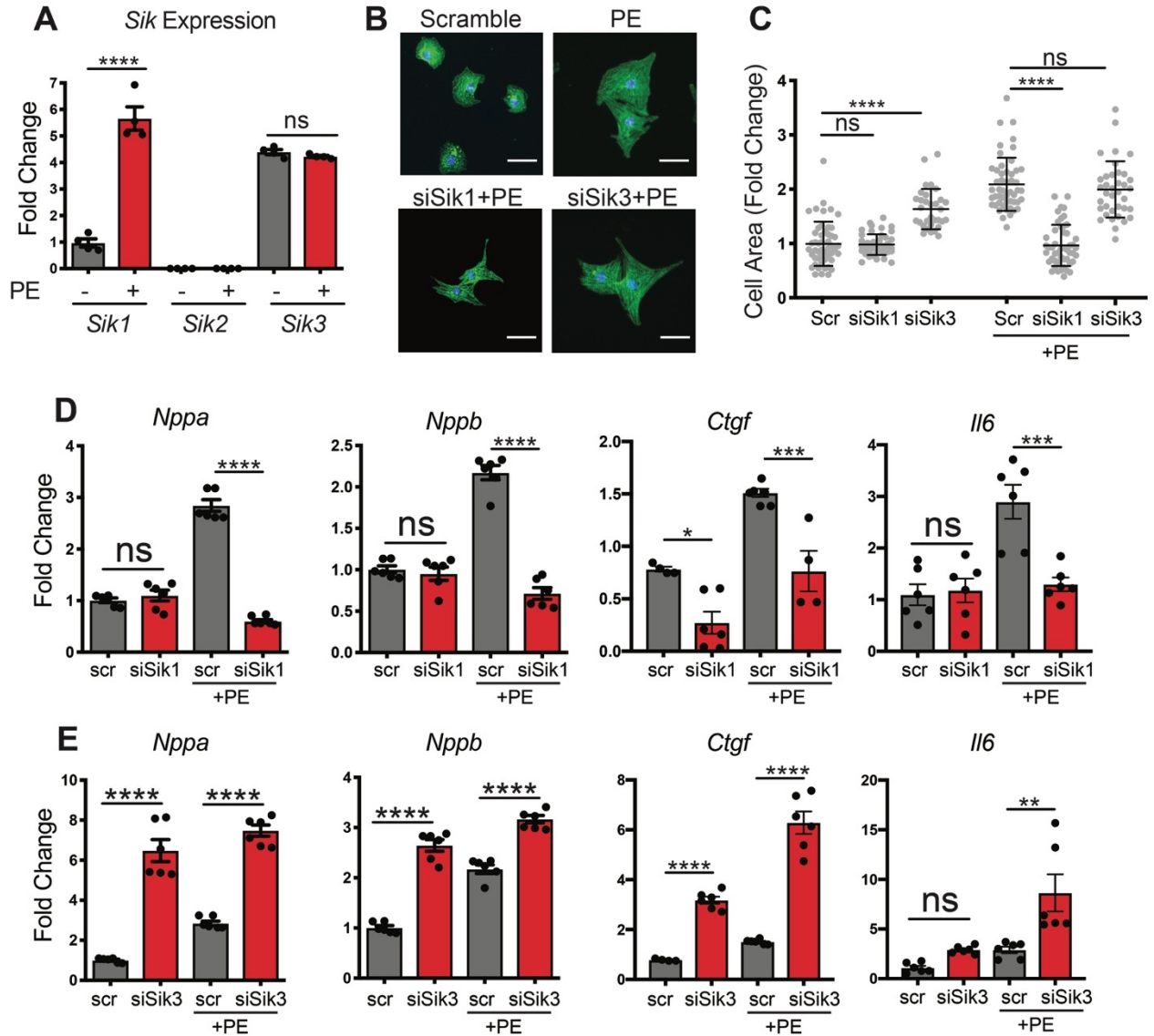


Figure 2.2. SIK1 is a positive regulator of cardiomyocyte hypertrophy. (A) qRT-PCR expression of *Sik* transcripts in NRVM treated \pm PE (100uM, 48hrs). (n=4). (B) NRVM treated with siRNAs against *Sik1* or *Sik3* and immunostained for α -actinin (green) and nuclei (blue) Scale = 40um (C) Cell area of NRVM (n=30-50). Bars denote mean \pm SD. (D,E) qRT-PCR expression for canonical HF-associated genes. (n=4-6) Data are shown as means \pm SEM unless noted. * $P < 0.05$, ** $P < 0.01$, *** $P < 0.001$, **** $P < 0.0001$ by one-way ANOVA with Tukey's multiple comparisons test.

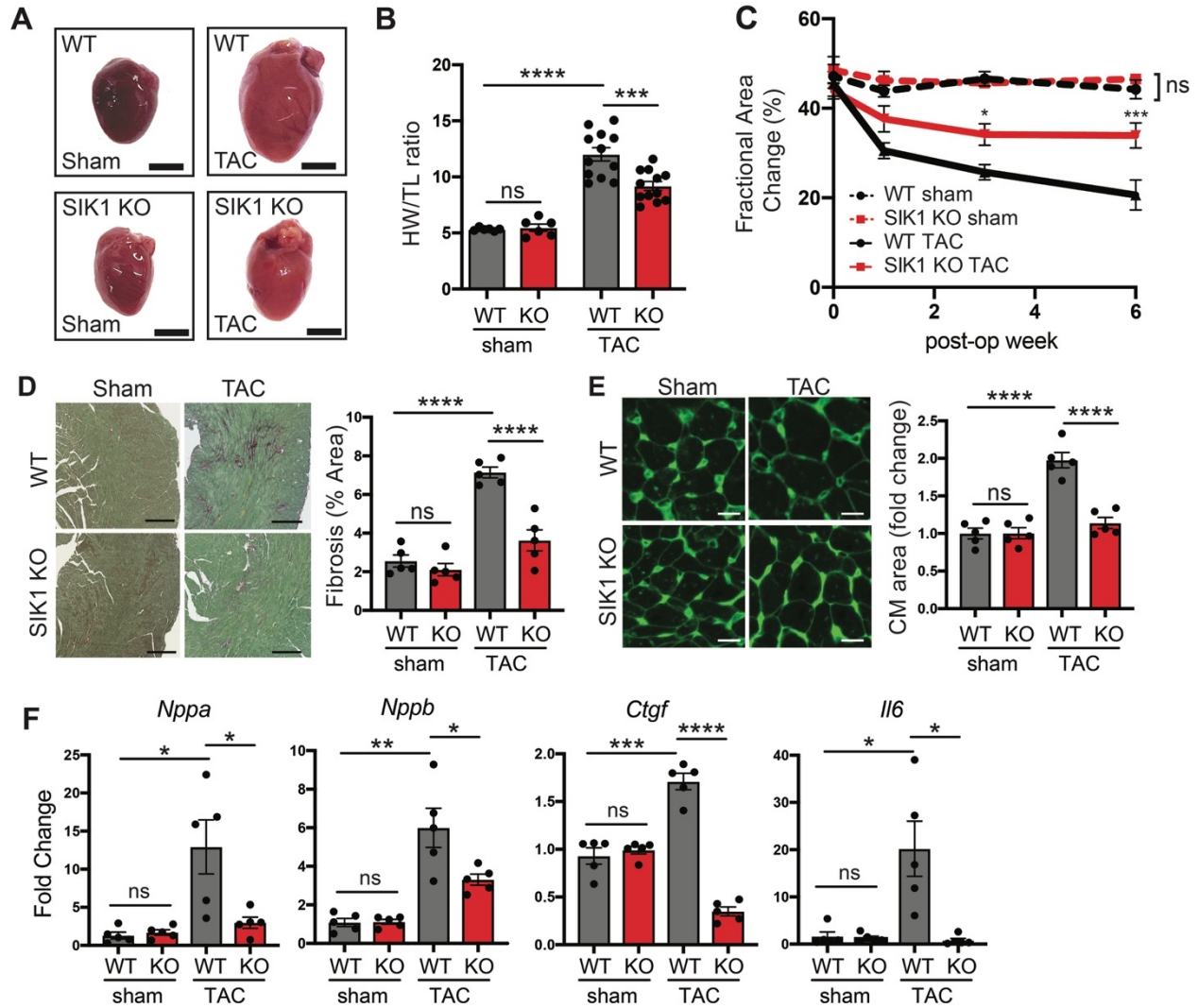
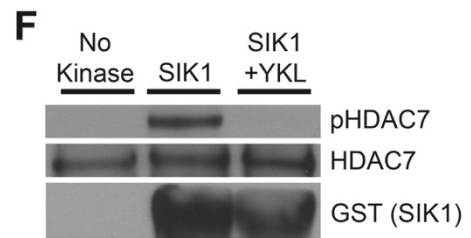
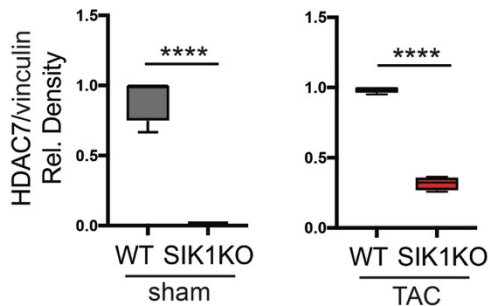
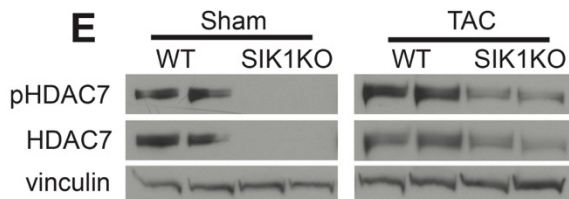
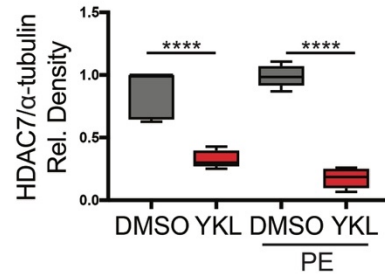
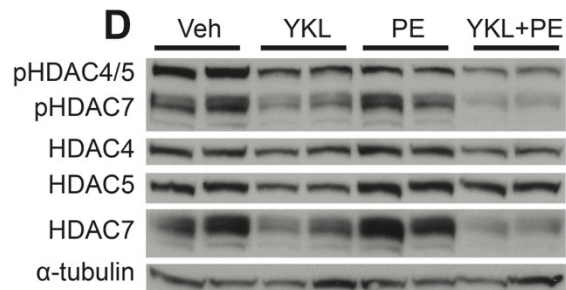
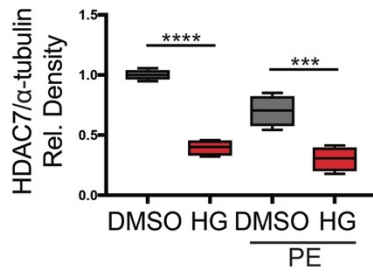
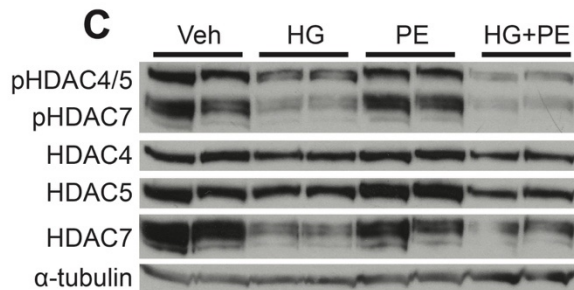
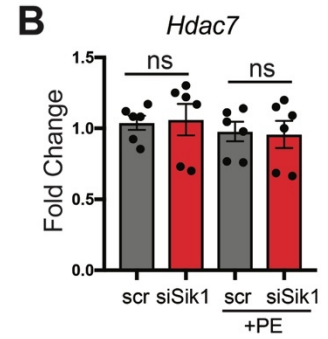
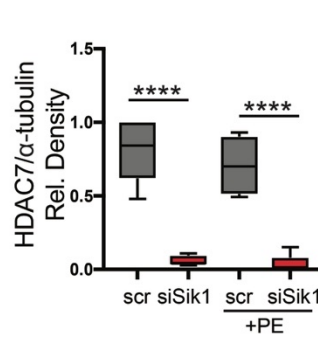
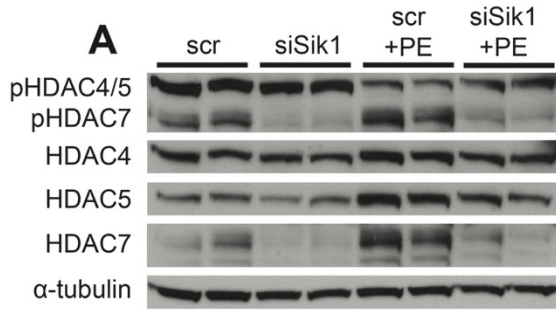


Figure 2.3. Global loss of SIK1 protects against pathologic cardiac remodeling in vivo. (A) Representative photos of freshly excised hearts. Scale=3mm. (B) Heart weight to tibial length ratio. (n=6 for sham, n=12 for TAC). (C) Echocardiographic measurements of fractional area change. (n=6 for sham, n=12 for TAC). *P<0.05, ****P<0.001 for SIK1KO TAC vs WT TAC by two-way ANOVA with Tukey's multiple comparisons test. (D) Picrosirius red staining of heart sections. (n=5) Scale=300um. (E) Wheat germ agglutinin staining of heart sections. (n=5). Scale=20um. (F) qRT-PCR expression for canonical heart failure associated genes. (n=5) Data are shown as means \pm SEM unless noted. *P<0.05, **P<0.01, ***P<0.001, ****P<0.0001 by one-way ANOVA with Tukey's multiple comparisons test.



SIK1 Consensus: L-x-R-S/T-x-S-x-x-x-L
 HDAC7 (Ser155): L-R-K-T-V-S-E-P-N-L

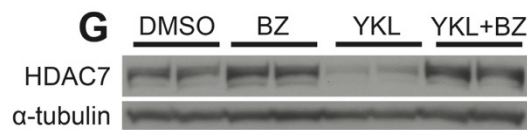


Figure 2.4. HDAC7 protein stability is dependent on SIK1 kinase activity. (A) Western blot for total and phosphorylated HDAC4, 5, and 7 in NRVM treated \pm siRNA against *Sik1* \pm PE (100uM, 24hr). α -tubulin used as loading control (n=5). (B) qRT-PCR expression for *Hdac7*. (n=6). Bars designate mean \pm SEM. (C,D) Western blot for total and phosphorylated HDAC4, 5, and 7 in NRVM treated \pm HG-9-91-01 (1uM) or YKL-05-099 (1uM). α -tubulin used as loading control (n=4). (E) Western blot for total and phosphorylated HDAC7 in WT and SIK1 KO sham/TAC left ventricular cardiac tissue. Vinculin used as loading control (n=4). (F) In vitro kinase assay with recombinant HDAC7 and GST-tagged SIK1 + YKL-05-099 (1uM). SIK1 consensus sequence shown below (representative western blots, n=3). (G) Western blot from NRVM treated with YKL-05-099 (1uM) and proteasome inhibitor bortezomib (BZ) (5nM, 16 hours) (representative western blots, n=3). All box plots show minimum, maximum, and median with 25th to 75th percentile range. ***P<0.001, ****P<0.0001 by one-way ANOVA with Tukey's multiple comparisons test.

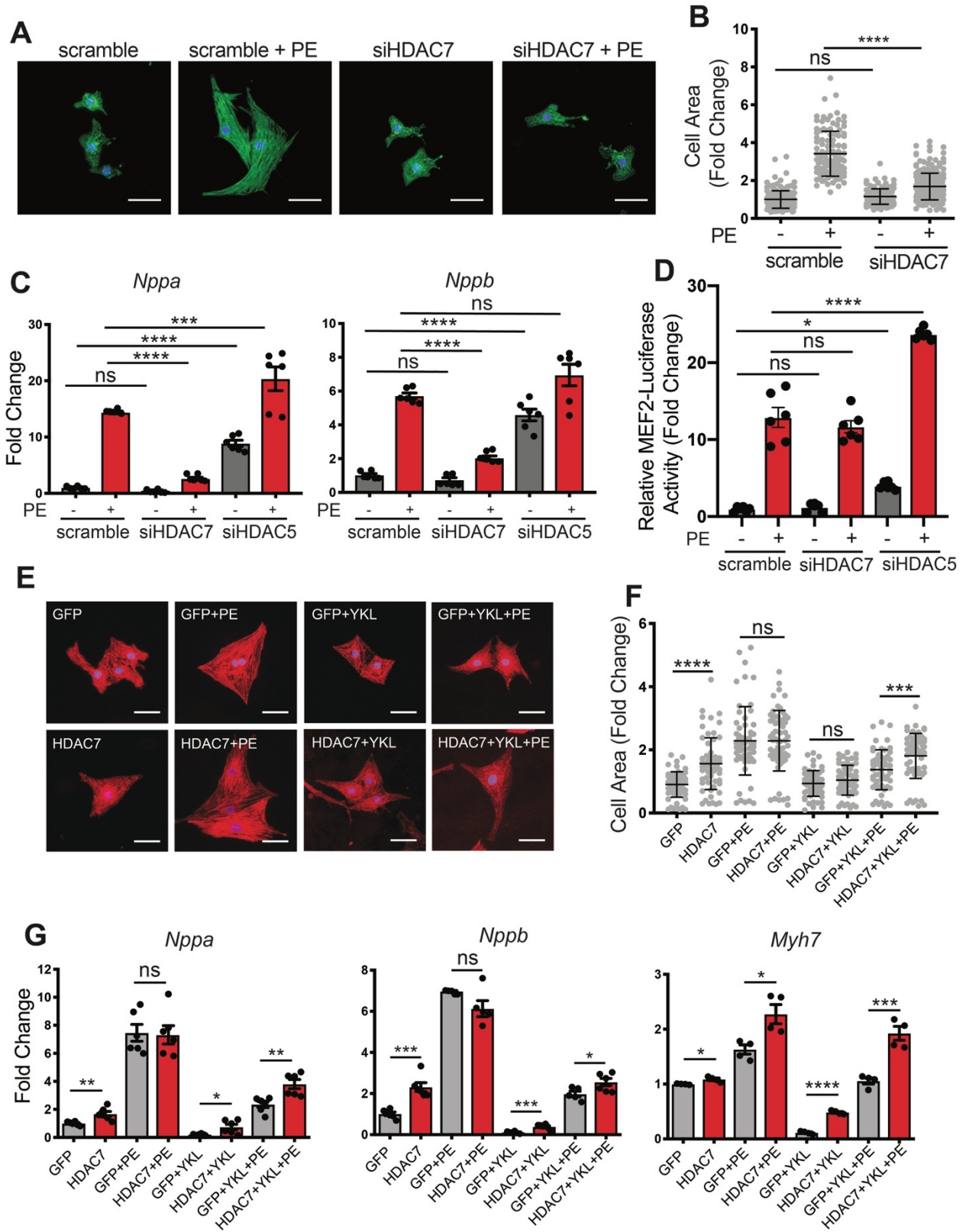


Figure 2.5. Loss of HDAC7 protects against pathologic cardiac remodeling in vitro. (A) NRVM treated with siRNA against *Hdac7* and immunostained for α -actinin (green) and nuclei (blue) Scale = 40um. (B) Cell area of NRVM. (n=108). Bars denote mean \pm SD (C) qRT-PCR expression for *Nppa* and *Nppb*. (n=6). (D) MEF2 dual luciferase reporter assay. Values normalized to renilla luciferase control. (n=6). (E) NRVM infected with adenovirus harboring GFP-HDAC7 or GFP alone and immunostained for α -actinin (red) and nuclei (blue). Scale = 40um. (F) Cell area of NRVM. (n=58-63). Bars denote mean \pm SD (G) qRT-PCR expression for canonical HF-associated genes. (n=6). Data are shown as means \pm SEM unless noted. *P<0.05, **P<0.01, ***P<0.001, ****P<0.0001 by one-way ANOVA with Tukey's multiple comparisons test.

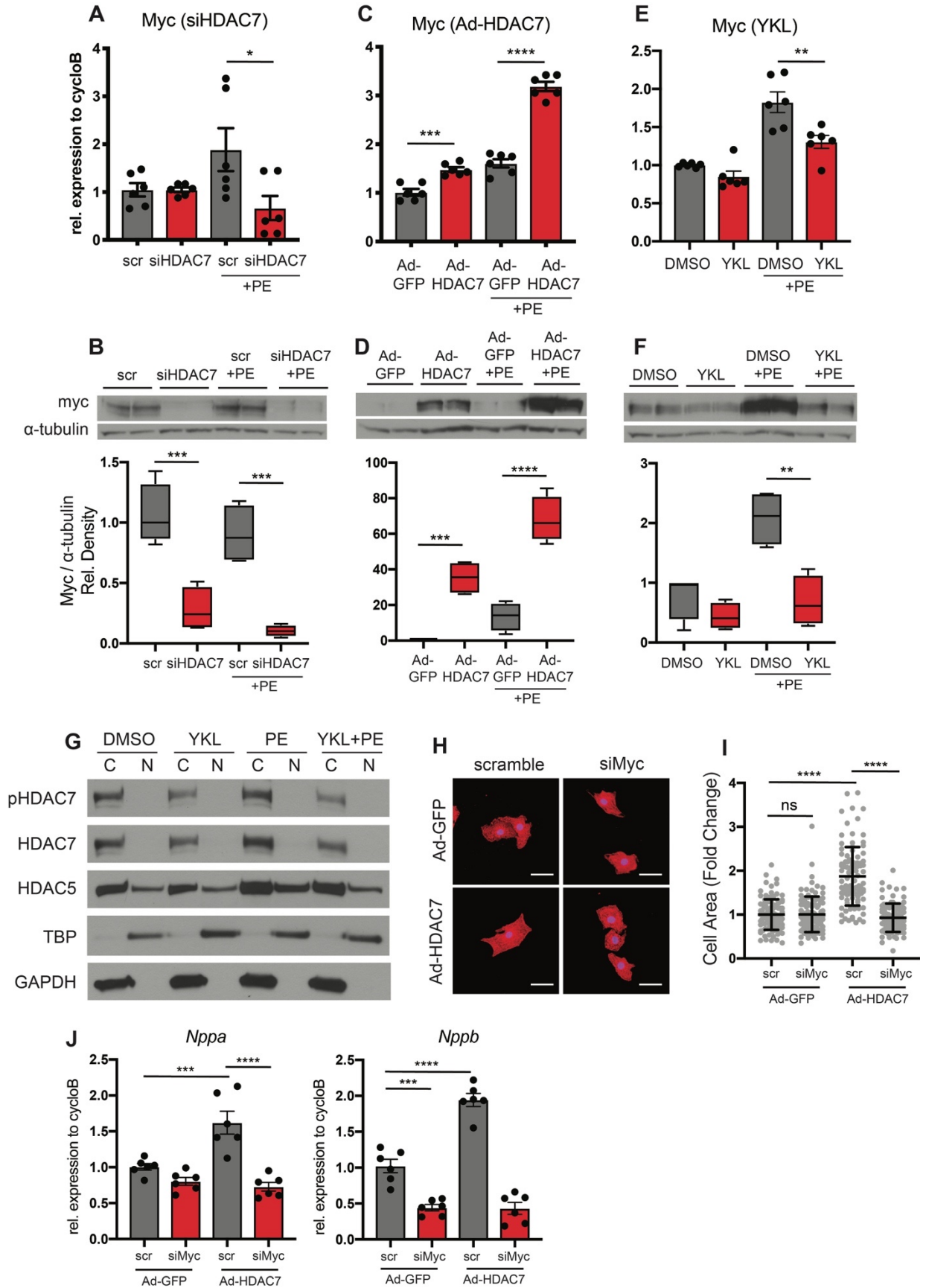


Figure 2.6. HDAC7 indirectly regulates c-Myc expression. qRT-PCR (n=6) and western blotting (n=4) for c-Myc expression in NRVM treated with (A and B) siRNA against *Hdac7*, (C and D) Ad-HDAC7, or (E and F) YKL-05-099 (1uM). All box plots show minimum, maximum, and median with 25th to 75th percentile range. (G) Western blotting of cytoplasmic (C) and nuclear (N) fractions of NRVM treated with 1uM YKL-05-099 + 100uM PE. TATA-box binding protein (TBP) and GAPDH used as nuclear and cytoplasmic markers, respectively (representative western blots, n=3). (H) NRVM treated with adenovirus harboring GFP-HDAC7 or GFP alone, followed by transfection of siRNA probes against *c-Myc* or scramble control. Immunostained for α -actinin (red) and nuclei (blue). Scale = 40um. (I) Cell area of NRVM. (n=100). Bars denote mean \pm SD (J) qRT-PCR expression for *Nppa* and *Nppb*. (n=6). Data are shown as means \pm SEM unless noted. *P<0.05, **P<0.01, ***P<0.001, ****P<0.0001 by one-way ANOVA with Tukey's multiple comparisons test.

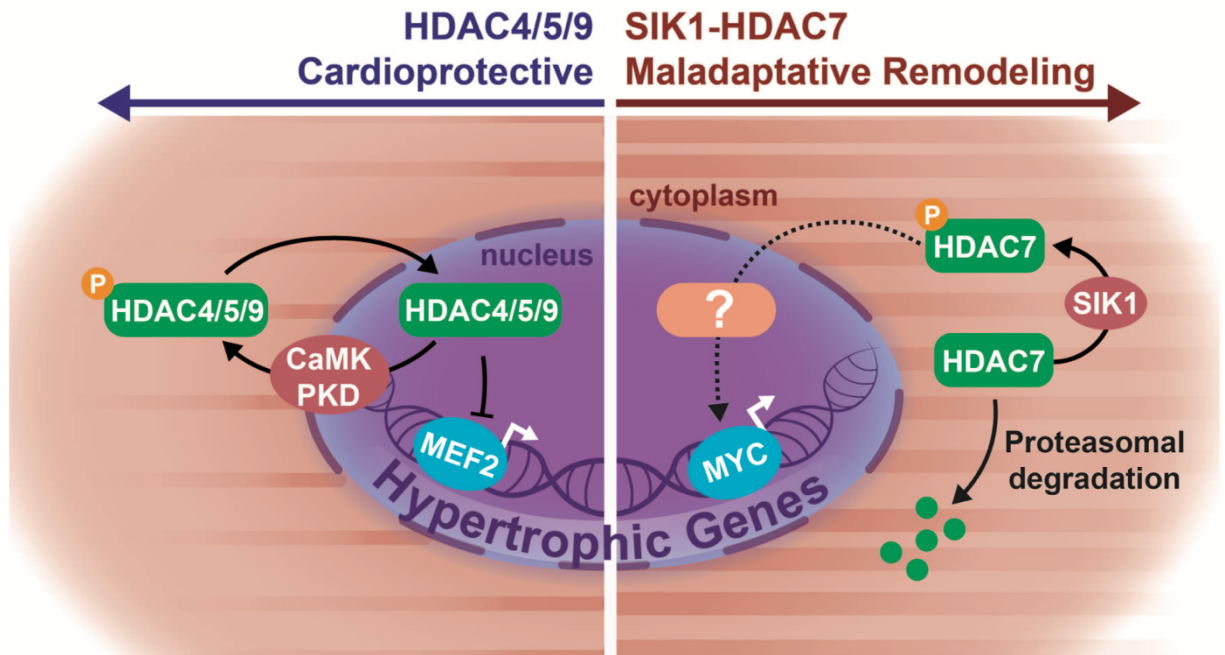
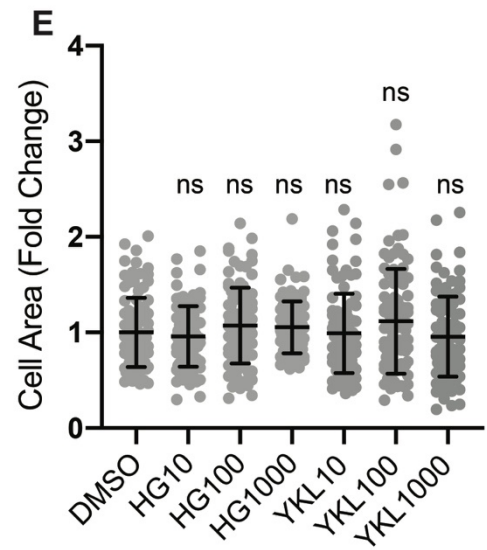
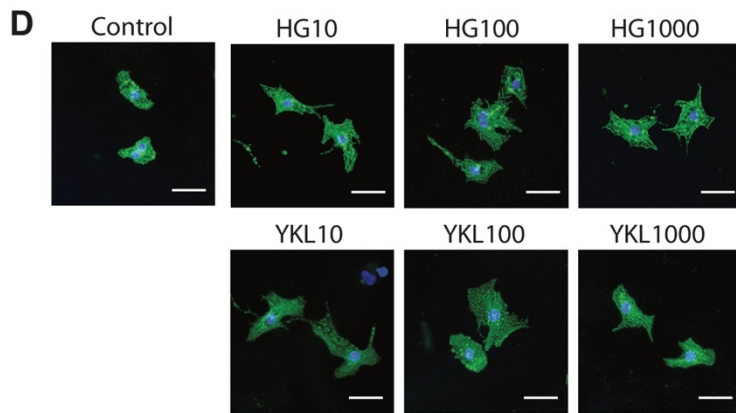
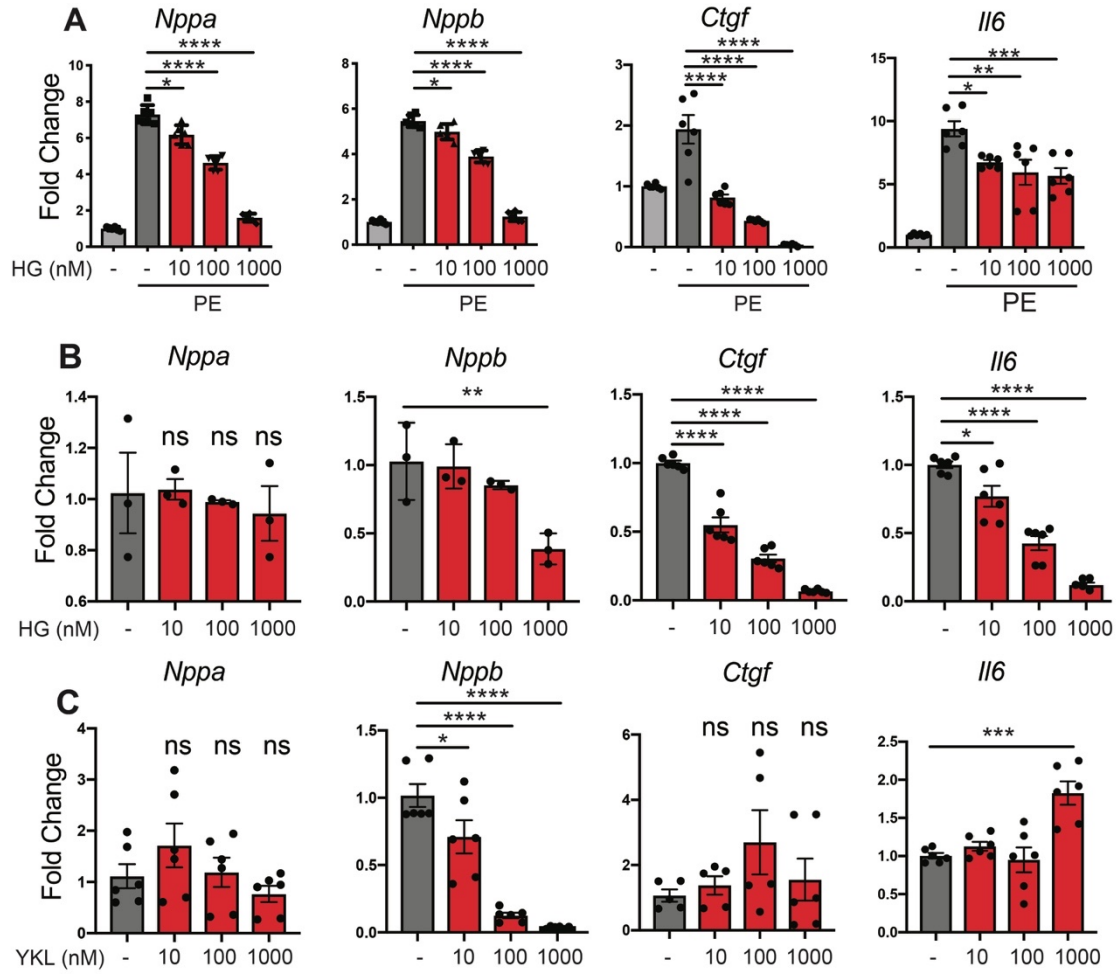
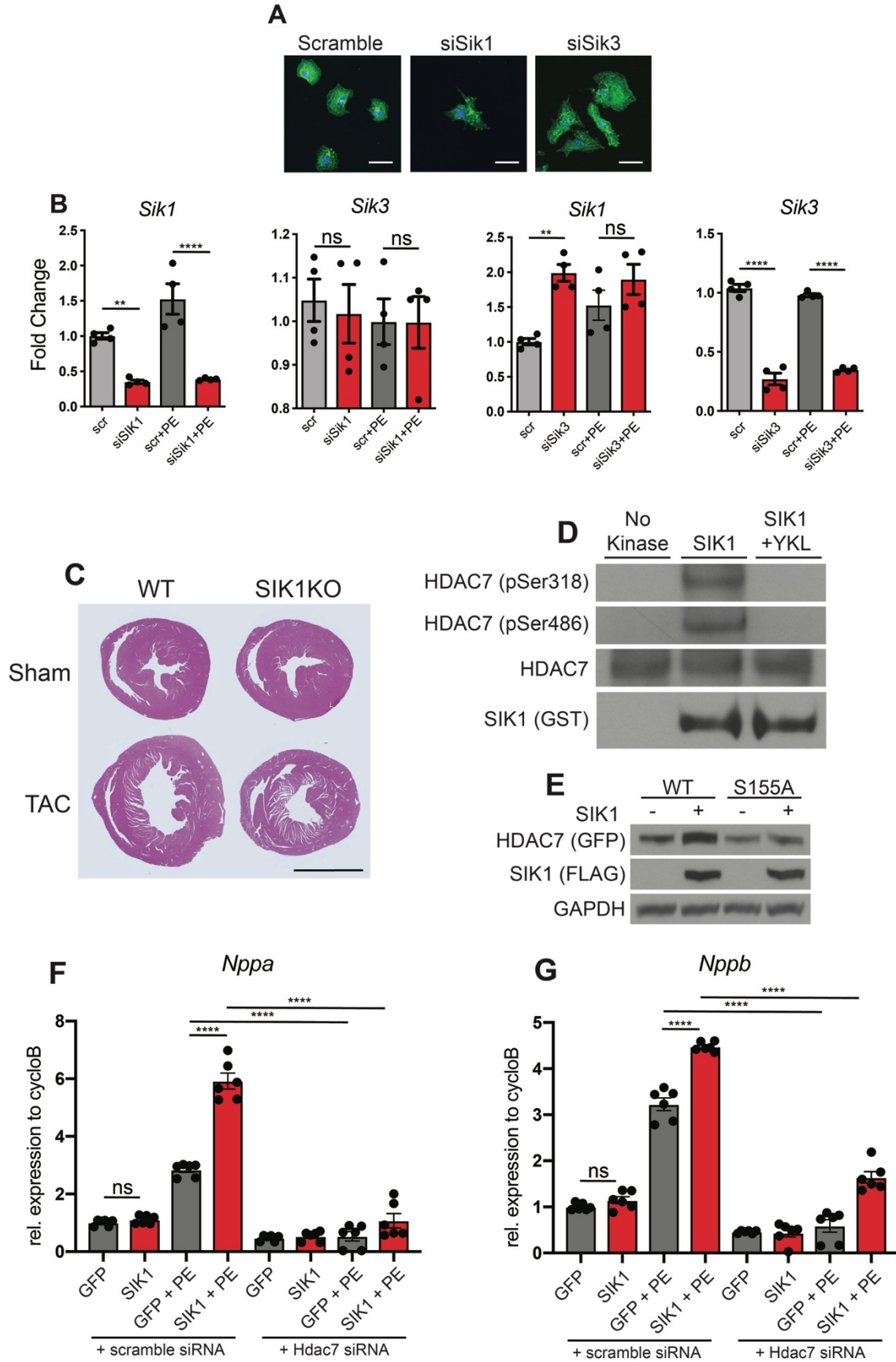


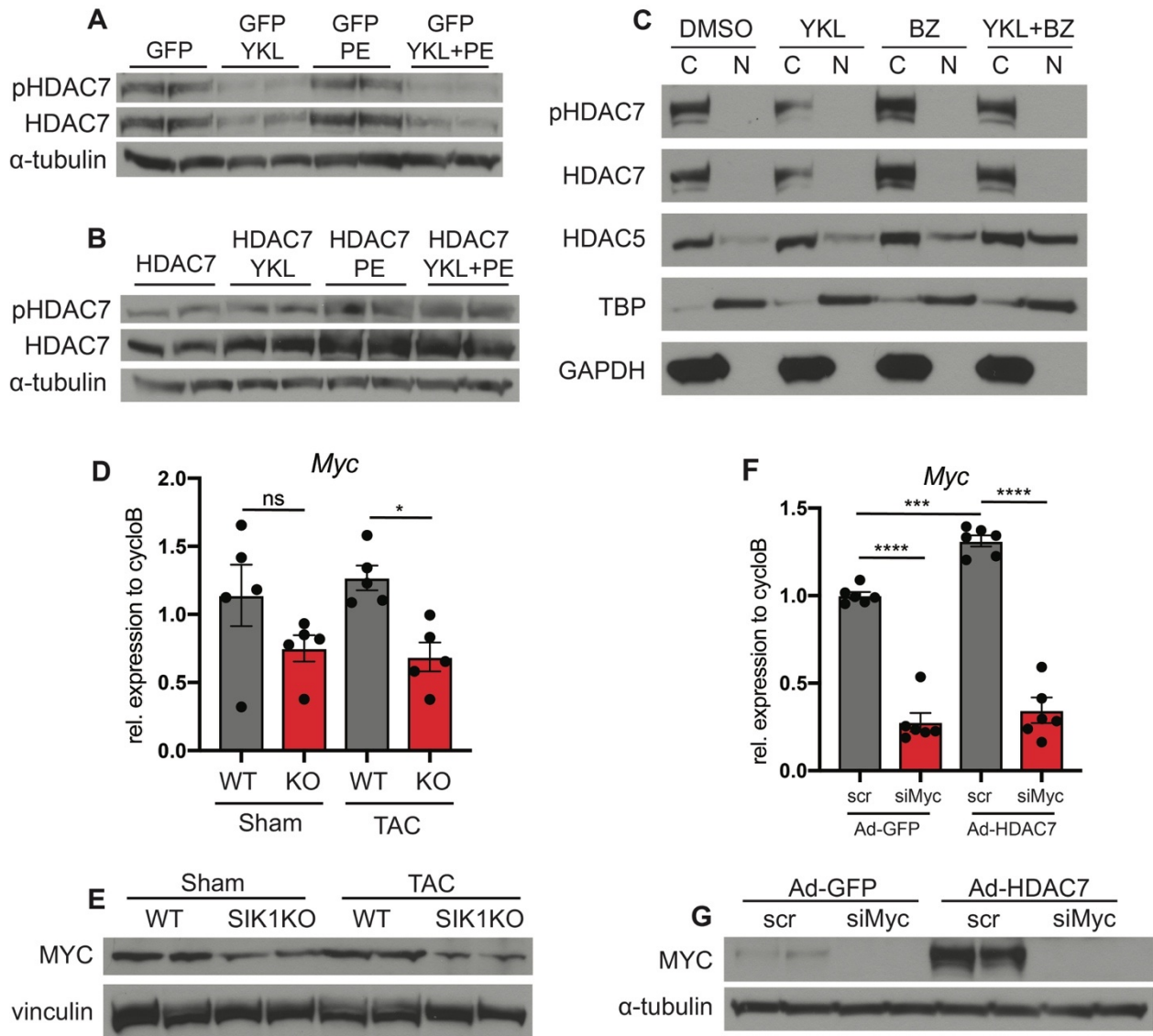
Figure 2.7: Proposed working model. Our proposed working model implicates a pro-hypertrophic SIK1-HDAC7 signaling axis in cardiac myocytes and a departure from the canonical model of class II HDAC function.



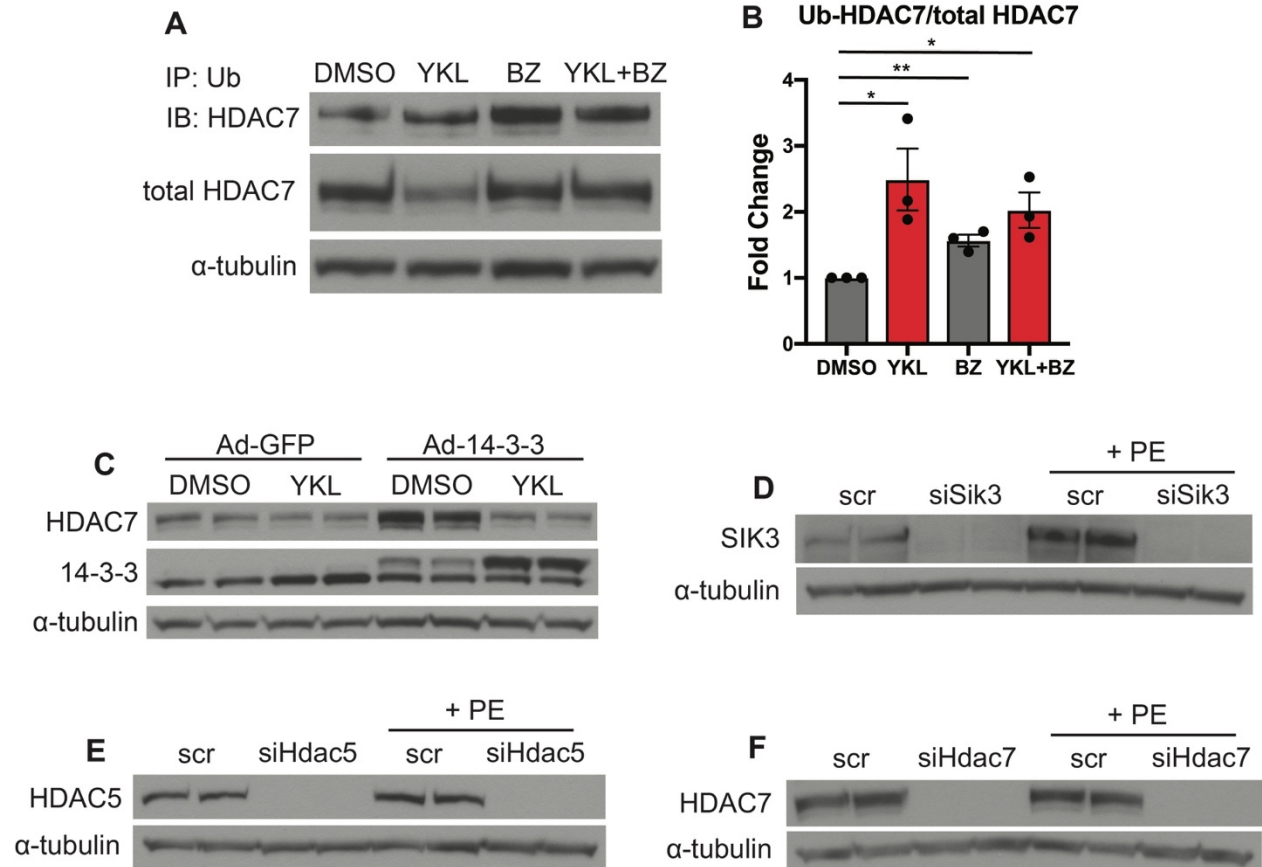
Supplemental Figure 2.1: (A-C) qRT-PCR expression for canonical heart failure associated genes. (n=4-6). Bars denote mean \pm SEM. (D) NRVM treated with HG or YKL (nM doses pictured) and immunostained for α -actinin (green) and nuclei (blue) Scale = 40 μ m. (E) Cell area of NRVM. (n=100 per condition). Bars denote mean \pm SD *P<0.05, **P<0.01, ***P<0.001, ****P<0.0001 by one-way ANOVA with Tukey's multiple comparisons test.



Supplemental Figure 2.2: (A) NRVM treated with siRNAs against *Sik1* or *Sik3* and immunostained for α -actinin (green) and nuclei (blue) Scale = 40um. (B) qRT-PCR expression for *Sik1* and *Sik3* in setting of siSik1 or siSik3 transfection. (C) Representative H&E staining on cardiac tissue from WT or *Sik1*^{-/-} mice. Scale=3mm. (D) In vitro kinase assay with recombinant HDAC7 and GST-tagged SIK1 + YKL-05-099 (1uM). (E) Cos7 cells were co-transfected with either WT HDAC7 or S155A HDAC7 + WT SIK1 plasmid or empty carrier plasmid. Cells were lysed 48 hours post transfection and assayed by western blotting. (F, G) qRT-PCR from NRVM infected with adenovirus expressing SIK1 followed by transfection of siRNA probes against *Hdac7* or scramble control. (n=6 per condition). Data are shown as means \pm SEM unless noted. **P<0.01, ***P<0.001, ****P<0.0001 by one-way ANOVA with Tukey's multiple comparisons test.



Supplemental Figure 2.3: (A, B) Western blotting for total and phosphorylated HDAC7 in NRVM treated with adenovirus expressing HDAC7 or GFP control. α -tubulin used as loading control. (C) Western blotting of cytoplasmic (C) and nuclear (N) fractions of NRVM treated with 1 μ M YKL-05-099 + 5nM bortezomib (BZ). TATA-box binding protein (TBP) and GAPDH used as nuclear and cytoplasmic markers, respectively. (D) qRT-PCR expression for *c-Myc* (n=5) in WT and SIK1 KO sham/TAC left ventricular cardiac tissue. (E) Western blot for C-MYC in WT and SIK1 KO sham/TAC left ventricular cardiac tissue. (F) qRT-PCR (n=6) and (G) western blotting (n=4) for *c-Myc* expression in NRVM infected with Ad-GFP or Ad-HDAC7 followed by transfection of siRNA against *c-Myc* or scramble control. Data are shown as means \pm SEM. * P <0.05, ** P <0.01, *** P <0.001, **** P <0.0001 by one-way ANOVA with Tukey's multiple comparisons test.



Supplemental Figure 2.4: (A) Immunoprecipitation of NRVM lysates with ubiquitin affinity beads followed by immunoblotting of HDAC7. NRVM were treated with YKL-05-099 (1 μ M) and bortezomib (5nM). (B) Ratio of ubiquitinated-HDAC7 to total-HDAC7. (C) Western blot for HDAC7 in NRVM infected with Ad-14-3-3 or Ad-GFP followed by treatment with YKL-05-099 (1 μ M). (D-F) Western blot for verification of SIK3 (D), HDAC5 (E), and HDAC7 (F) knockdown. Data are shown as means \pm SEM. *P<0.05, **P<0.01 by one-way ANOVA with Tukey's multiple comparisons test.

Methods

NRVM isolation and culture

NRVM were isolated from hearts of 2 day old Sprague-Dawley rat pups (Charles River) under aseptic conditions as previously described (29). Cells were pre-plated for 2 hours on tissue culture plates followed by 48 hours of exposure to BrdU in culture medium to remove contaminating non-myocytes. NRVM were plated in growth media (DMEM, 5% FBS, 100U/mL penicillin-streptomycin) for 48 hours and switched to serum free media thereafter (DMEM, 0.1% BSA, 1% insulin-transferring-selenium, 100U/mL penicillin-streptomycin). Prior to stimulation with PE, NRVM were maintained in serum free media for 48-72 hours. NRVM were treated with SIK inhibitors at the indicated concentrations for 16 hours prior to PE stimulation (100uM).

For siRNA treatments, NRVM were transfected with RNAiMax (Invitrogen) and 50nM of siRNA in serum free media for 48 hours prior to PE stimulation (100uM). siRNAs were purchased from Sigma-Aldrich (Scramble control siRNA; SIC001, *Sik1* siRNA; SASI_Rn01_00053040, *Sik3* siRNA; SASI_Rn02_00326476, *Hdac5* siRNA; SASI_Rn02_00372147, *Hdac7* siRNA; SASI_Rn02_00277288, *c-Myc* siRNA; SASI_Rn01_00089127).

Western Blotting

To prepare whole cell extracts, NRVM were lysed in RIPA buffer supplemented with protease and phosphatase inhibitors (Roche). Protein concentrations were quantified by BCA assay (Thermo Fisher 23225). Lysates were diluted in 4x reducing Laemmli buffer,

boiled at 95 °C for 5 minutes and resolved on a 4-12% Bis-Tris SDS PAGE gel. Resolved proteins were transferred onto a PVDF membrane. Membranes were then blocked with 5% milk in TBST for 1 hour at room temperature followed by primary antibody incubation overnight at 1:1000 dilution in 5% BSA or milk. After overnight incubation, secondary HRP conjugated antibody was added for 1 hour at a dilution of 1:1000-1:5000 in 5% milk in TBST. Membranes were incubated with Amersham ECL Prime Western Blotting Detection Reagent (GE Life Sciences RPN2232) and exposed to autoradiography film at various time intervals.

Catalog numbers for antibodies used in this study: phospho-HDAC4(Ser246) / HDAC5(Ser259) / HDAC7(Ser155) (CST, 3443), phospho-HDAC4(Ser632) / HDAC5(Ser661) / HDAC7(Ser486) (CST, 3424), phospho-HDAC7(Ser318) (Novus Biologicals, NBP2-03978), HDAC4 (CST, 7628), HDAC5 (CST, 20458) , HDAC7 (CST, 33418), alpha-tubulin (Sigma, 05829), vinculin (Sigma, V9131), c-Myc (CST, 5605), GST (CST, 2625), SIK3 (MRCPPU, DU39537), 14-3-3 (CST, 8312), GAPDH (CST, 5174), TBP (Abcam, ab51841).

qRT-PCR from NRVM and mouse tissue

Total RNA was extracted from NRVM using the High Pure RNA Isolation Kit (Roche) according to manufacturer's instructions. For cardiac tissue, a 10- to 20-mg piece of mouse LV tissue was collected and preserved in RNAlater (Qiagen) followed by mechanical disruption/homogenization in PureZOL (BioRad) on a TissueLyser II (Qiagen). The RNA containing aqueous phase was extracted with chloroform and further

purified using the Aurum Total RNA Fatty and Fibrous Tissue Kit (BioRad). First-strand cDNA synthesis was performed using iScript Reverse Transcription Supermix (BioRad). TaqMan based qRT-PCR was performed using SsoAdvanced Universal Probes Supermix (BioRad), labeled probes from the Universal Probe Library (Roche), and gene specific oligonucleotide primers on a CFX384 Touch Real-Time PCR Detection System (BioRad). A list of qRT-PCR primers and TaqMan probes are provided in Supplemental Tables 1 and 2. Relative expression was calculated using the $2^{-\Delta\Delta Ct}$ method with normalization to *Ppib*.

Mouse model of cardiac hypertrophy and heart failure

All mice were aged 8-10 weeks prior to surgery. Sham and TAC surgeries were performed as previously described (29). Briefly, mice were anesthetized with isoflurane, mechanically ventilated, and subjected to thoracotomy. For TAC surgery, the aortic arch was constricted between the left common carotid and the brachiocephalic arteries using a 7-0 silk suture and a 25-gauge needle. In sham surgeries, thoracotomy was performed as above and the aorta was surgically exposed without further intervention.

Transthoracic echocardiography

Mice were anesthetized with 1% inhalational isoflurane and imaged using the Vevo 770 High Resolution Imaging System (FujiFilm VisualSonics Inc.) and the RMV-707B 30-MHz probe. Measurements were obtained from M-mode sampling and integrated electrocardiogram-gated kilohertz visualization (EKV) images taken in the LV short axis view at the mid-papillary muscle level as previously described (29).

Histology and immunofluorescence

For cellular immunofluorescence studies, NRVM were seeded on glass coverslips coated with 0.1% gelatin. NRVM were fixed in 2% paraformaldehyde for 20 minutes at room temperature followed by permeabilization with PBST + 0.1% Triton X. NRVM were incubated in PBST + 5% horse serum for 1 hour and then stained with primary antibody against alpha-actinin at 1:800 (Sigma, A7811) for 1 hour. NRVM were washed with 3x with PBST followed by staining with secondary antibody at 1:1000 for 1 hour. Cells were washed 3X with PBST and mounted with Vectashield Hardset mounting media with DAPI. For cardiac tissue samples, mid-ventricular short axis cross sections were fixed in 10% neutral buffered formalin overnight at 4 °C and transferred to 100% ethanol for 24 hours. Samples were embedded in paraffin blocks, sectioned, and stained with Picrosirius Red (Polysciences) or Wheat Germ Agglutinin 488 (Thermo Fisher, W11261) according to manufacturers' instructions. Fibrosis area and cardiomyocyte cross sectional area were quantified as previously described (29).

Luciferase Assay

NRVM were infected with adenovirus harboring MEF2 firefly luciferase and renilla luciferase (Seven Hills Bioreagents) at MOI of 1 for 2 hours, followed by PBS wash and culture in serum free media. 24 hours post infection, NRVM were transfected with siRNAs against *Hdac5*, *Hdac7*, or scramble control. 48 hours post siRNA transfection, cells were then treated with PE (100uM) for 48 hours and harvested using the Dual Luciferase Reporter Assay (Promega) according to manufacturer's instructions. MEF2 luciferase reporter values were normalized to internal renilla luciferase signal.

Adenovirus

Adenoviruses were generated by cloning target fragments into the Gateway entry vector pENTR2B, followed by LR recombination into Gateway destination vector pAd-CMV-V5 DEST and transfection into 293A cells according to manufacturer's protocol. We thank Jeroen Roose (UCSF, San Francisco CA) for providing the GFP-HDAC7 plasmid. Cells plaques were observed as early as 1 week post transfection and were fully lysed no later than 2 weeks post transfection. 293A cells were then infected with serially diluted crude adenoviral lysate and overlaid with SeaPlaque Agarose to allow for plaque formation. Single plaques were isolated and tested for protein expression. Validated plaques were amplified on 293A cells and titered using a standard plaque formation assay to calculate plaque forming units (PFU). Ad-14-3-3 and Ad-SIK1 viruses were purchased from Vector Biolabs. To infect NRVM, cells were incubated in low volume of serum free media containing adenoviral particles (MOI of 1) for 2 hours in 37 °C 5% CO₂, rocking every 30 min. NRVM were washed with PBS without Ca²⁺ or Mg²⁺ and cultured in fresh serum free media.

qRT-PCR and BNP ELISA from iPSC cardiomyocytes

iPSC cardiomyocytes were purchased from Cellular Dynamics and maintained according to manufacturer's protocols. Cells were seeded on 96 well culture plates coated with 5ug/mL of fibronectin and maintained in William's E Media supplemented with 1:25 of Cell Maintenance Cocktail B (Thermo Fisher, CM4000). For hypertrophic stimulation, cells were pre-treated with SIK inhibitors for 16 hours, followed by stimulation with 10nM of endothelin-1 for 18 hours. RNA was isolated and reverse transcribed using the Taqman

Cells-to-CT kit (Life Technologies, AM1278) according to manufacturer's instructions. qRT-PCR was performed using Life Technologies TaqMan assays for human *NPPB* and *B2M* (housekeeping) (*NPPB*, Hs00173590_m1; *B2M*, Hs000984230_m1). ELISA for BNP protein was performed using 6uL of spent media from each well of a 96 well plate as previously described (29) using the following antibodies: anti-proBNP capture antibody (Abcam, ab13111), anti-proBNP detection antibody (Abcam, ab13124) and N-term pro-BNP peptide standard (Phoenix Pharmaceuticals, 011-42).

Cell area measurements for iPSC cardiomyocytes

For cell size assays, cells were plated on Ibidi 8 well chamber slides and pre-treated with SIK inhibitors for 16 hours, followed by stimulation with 10nM ET-1 (Sigma, E7764) for 18 hours. Cells were fixed in 2% paraformaldehyde for 20 minutes, permeabilized with PBST + 0.1% Triton X-100 for 20 minutes, and blocked with PBST + 5% horse serum for 1 hour at room temperature. Primary antibody against sarcomeric alpha-actinin was used at a dilution of 1:800 in PBST +5% horse serum for 1 hour at room temperature. Secondary anti-mouse antibody was used at a dilution of 1:1000 in PBST + 5% horse serum for 1 hour at room temperature. Cells were imaged and quantified as previously described (29).

In vitro kinase assay

10ng of recombinant SIK1 (Thermo Fisher) and 100ng of recombinant HDAC7 (Origene) were incubated in a final volume of 40uL containing 1X kinase buffer (CST) supplemented with 100uM ATP. 1uM of YKL-05-099 was added for inhibition of SIK1 activity. Reactions

were incubated for 30 minutes at 30 °C, followed by addition of 4X Laemmli buffer. Samples were boiled at 95 °C for 5 minutes and resolved by SDS-PAGE.

Nuclear/Cytoplasmic Fractionation

Nuclear and cytoplasmic fractions were prepared from NRVM using the NE-PER Nuclear and Cytoplasmic Extraction Reagents (Thermo Fisher, 78833) according to manufacturer's instructions.

Statistics

Data were evaluated by one-way and two-way ANOVA with Tukey's multiple comparisons test. Differences with a *P* value of less than or equal to 0.05 were considered statistically significant.

Study Approval

All protocols concerning animal use were approved by the Institutional Animal Care and Use Committees at the University of California, San Francisco and conducted in strict accordance with the National Institutes of Health Guide for the Care and Use of Laboratory Animals (30). Mice were housed in a temperature- and humidity-controlled pathogen-free facility with 12-hour light/dark cycle and ad libitum access to water and standard laboratory rodent chow.

References

1. Hill JA, and Olson EN. Cardiac plasticity. *N Engl J Med.* 2008;358(13):1370-80.
2. Zhang CL, McKinsey TA, Chang S, Antos CL, Hill JA, and Olson EN. Class II histone deacetylases act as signal-responsive repressors of cardiac hypertrophy. *Cell.* 2002;110(4):479-88.
3. Chang S, McKinsey TA, Zhang CL, Richardson JA, Hill JA, and Olson EN. Histone deacetylases 5 and 9 govern responsiveness of the heart to a subset of stress signals and play redundant roles in heart development. *Mol Cell Biol.* 2004;24(19):8467-76.
4. Lehmann LH, Jebessa ZH, Kreusser MM, Horsch A, He T, Kronlage M, et al. A proteolytic fragment of histone deacetylase 4 protects the heart from failure by regulating the hexosamine biosynthetic pathway. *Nat Med.* 2018;24(1):62-72.
5. Berdeaux R, Goebel N, Banaszynski L, Takemori H, Wandless T, Shelton GD, et al. SIK1 is a class II HDAC kinase that promotes survival of skeletal myocytes. *Nat Med.* 2007;13(5):597-603.
6. Wang B, Moya N, Niessen S, Hoover H, Mihaylova MM, Shaw RJ, et al. A hormone-dependent module regulating energy balance. *Cell.* 2011;145(4):596-606.
7. Jackson T, Allard MF, Sreenan CM, Doss LK, Bishop SP, and Swain JL. The c-myc proto-oncogene regulates cardiac development in transgenic mice. *Mol Cell Biol.* 1990;10(7):3709-16.
8. Ahuja P, Zhao P, Angelis E, Ruan H, Korge P, Olson A, et al. Myc controls transcriptional regulation of cardiac metabolism and mitochondrial biogenesis in response to pathological stress in mice. *J Clin Invest.* 2010;120(5):1494-505.

9. Simpson P, McGrath A, and Savion S. Myocyte hypertrophy in neonatal rat heart cultures and its regulation by serum and by catecholamines. *Circ Res.* 1982;51(6):787-801.
10. Sundberg TB, Liang Y, Wu H, Choi HG, Kim ND, Sim T, et al. Development of Chemical Probes for Investigation of Salt-Inducible Kinase Function in Vivo. *ACS Chem Biol.* 2016;11(8):2105-11.
11. Chen HH, and Burnett JC. Natriuretic peptides in the pathophysiology of congestive heart failure. *Curr Cardiol Rep.* 2000;2(3):198-205.
12. Sugden PH, and Clerk A. Cellular mechanisms of cardiac hypertrophy. *J Mol Med (Berl).* 1998;76(11):725-46.
13. Zhi D, Irvin MR, Gu CC, Stoddard AJ, Lorier R, Matter A, et al. Whole-exome sequencing and an iPSC-derived cardiomyocyte model provides a powerful platform for gene discovery in left ventricular hypertrophy. *Front Genet.* 2012;3:92.
14. Wein MN, Foretz M, Fisher DE, Xavier RJ, and Kronenberg HM. Salt-Inducible Kinases: Physiology, Regulation by cAMP, and Therapeutic Potential. *Trends Endocrinol Metab.* 2018;29(10):723-35.
15. Paulo E, Wu D, Wang Y, Zhang Y, Wu Y, Swaney DL, et al. Sympathetic inputs regulate adaptive thermogenesis in brown adipose tissue through cAMP-Salt inducible kinase axis. *Sci Rep.* 2018;8(1):11001.
16. Rockman HA, Ross RS, Harris AN, Knowlton KU, Steinhilper ME, Field LJ, et al. Segregation of atrial-specific and inducible expression of an atrial natriuretic factor transgene in an in vivo murine model of cardiac hypertrophy. *Proc Natl Acad Sci U S A.* 1991;88(18):8277-81.

17. Kao HY, Verdel A, Tsai CC, Simon C, Juguilon H, and Khochbin S. Mechanism for nucleocytoplasmic shuttling of histone deacetylase 7. *J Biol Chem.* 2001;276(50):47496-507.
18. Li X, Song S, Liu Y, Ko SH, and Kao HY. Phosphorylation of the histone deacetylase 7 modulates its stability and association with 14-3-3 proteins. *J Biol Chem.* 2004;279(33):34201-8.
19. Zhu C, Chen Q, Xie Z, Ai J, Tong L, Ding J, et al. The role of histone deacetylase 7 (HDAC7) in cancer cell proliferation: regulation on c-Myc. *J Mol Med (Berl).* 2011;89(3):279-89.
20. Starksen NF, Simpson PC, Bishopric N, Coughlin SR, Lee WM, Escobedo JA, et al. Cardiac myocyte hypertrophy is associated with c-myc protooncogene expression. *Proc Natl Acad Sci U S A.* 1986;83(21):8348-50.
21. Vega RB, Harrison BC, Meadows E, Roberts CR, Papst PJ, Olson EN, et al. Protein kinases C and D mediate agonist-dependent cardiac hypertrophy through nuclear export of histone deacetylase 5. *Mol Cell Biol.* 2004;24(19):8374-85.
22. Harrison BC, Kim MS, van Rooij E, Plato CF, Papst PJ, Vega RB, et al. Regulation of cardiac stress signaling by protein kinase d1. *Mol Cell Biol.* 2006;26(10):3875-88.
23. Backs J, Song K, Bezprozvannaya S, Chang S, and Olson EN. CaM kinase II selectively signals to histone deacetylase 4 during cardiomyocyte hypertrophy. *J Clin Invest.* 2006;116(7):1853-64.
24. Backs J, Worst BC, Lehmann LH, Patrick DM, Jebessa Z, Kreusser MM, et al. Selective repression of MEF2 activity by PKA-dependent proteolysis of HDAC4. *J Cell Biol.* 2011;195(3):403-15.

25. Salian-Mehta S, Xu M, McKinsey TA, Tobet S, and Wierman ME. Novel Interaction of Class IIb Histone Deacetylase 6 (HDAC6) with Class IIa HDAC9 Controls Gonadotropin Releasing Hormone (GnRH) Neuronal Cell Survival and Movement. *J Biol Chem.* 2015;290(22):14045-56.
26. Bakin RE, and Jung MO. Cytoplasmic sequestration of HDAC7 from mitochondrial and nuclear compartments upon initiation of apoptosis. *J Biol Chem.* 2004;279(49):51218-25.
27. Gupta MP, Samant SA, Smith SH, and Shroff SG. HDAC4 and PCAF bind to cardiac sarcomeres and play a role in regulating myofilament contractile activity. *J Biol Chem.* 2008;283(15):10135-46.
28. Kang DH, Yin GN, Choi MJ, Song KM, Ghatak K, Minh NN, et al. Silencing Histone Deacetylase 7 Alleviates Transforming Growth Factor-beta1-Induced Profibrotic Responses in Fibroblasts Derived from Peyronie's Plaque. *World J Mens Health.* 2018;36(2):139-46.
29. Duan Q, McMahon S, Anand P, Shah H, Thomas S, Salunga HT, et al. BET bromodomain inhibition suppresses innate inflammatory and profibrotic transcriptional networks in heart failure. *Sci Transl Med.* 2017;9(390).
30. Council NR. Washington, DC: The National Academies Press; 2011.

**Chapter 3: Salt-inducible kinase 3 maintains ARHGAP21 stability to repress
cardiac hypertrophy**

Abstract

Salt-inducible kinase 3 is the last uncharacterized SIK isoform expressed in the mammalian heart. Here, we show that loss of SIK3 expression led to induction of adverse cardiac remodeling and hypertrophy in cultured neonatal rat cardiomyocytes and adult mouse hearts. Through unbiased proteomic profiling, we found that ARHGAP21 protein levels were greatly depleted in the setting of *Sik3* knockdown and that loss of ARHGAP21 led to spontaneous induction of hypertrophy under basal conditions. Loss of SIK3 and ARHGAP21 expression led to nuclear enrichment of MRTF-A and downstream activation of hypertrophic gene programs. Taken together, our findings reveal a previously unrecognized role for a SIK3-ARHGAP21 signaling axis in regulating cardiac homeostasis and repression of pathologic cardiac remodeling.

Background

Salt-inducible kinases (SIKs; SIK1, 2, and 3 in mammals) are a class of threonine/serine kinases that have become increasingly appreciated as emerging regulators of key processes such as metabolism, signaling transduction, and cellular homeostasis¹. Our group has previously uncovered the first demonstrated role for SIKs in regulating pathologic cardiac remodeling in the mammalian heart². We showed that salt-inducible kinase 1 (SIK1) functions as a pro-hypertrophic effector and drives remodeling events in part through stabilization of a class IIa HDAC, HDAC7. However, whether any of the remaining SIK isoforms also play a role in regulation cardiac hypertrophy and remodeling remains unknown.

In the mammalian heart, only SIK1 and SIK3 appear to be expressed whereas SIK2 expression is notably undetectable². In this study, we characterize the last remaining SIK isoform to be interrogated in the mammalian heart. Surprisingly, we find that SIK3 functions in the opposite manner to SIK1 – acting as a negative regulator and repressor of cardiac hypertrophy and remodeling in both cultured cardiomyocytes and adult mouse hearts. Mechanistically, we found that SIK3 maintains cardiac homeostasis in part through the stabilization of ARHGAP21 protein which in turn tightly regulates MRTF-A spatial localization and activation. Taken together, our results uncover a new SIK3-ARHGAP21 signaling axis that implicates SIK3 as a critical repressor of hypertrophic events – highlighting the diverging and complex roles of the SIK family in the regulation of cardiac remodeling and homeostasis.

Results

SIK3 represses pathologic cardiac remodeling in vitro and in vivo

We previously demonstrated a novel role for the salt-inducible kinase protein family in regulating pathologic cardiac remodeling. Specifically, we showed that one isoform called salt-inducible kinase 1 (SIK1) functions as a positive driver of cardiac remodeling and hypertrophy. We now sought to test whether the other SIK isoform expressed in the heart, salt inducible kinase 3 (SIK3), also harbors a functional role in regulating cardiac remodeling. To test the role of SIK3 in the heart, we leveraged a well-established in vitro model utilizing primary neonatal rat ventricular myocytes (NRVM), which features a well-characterized hypertrophic response and induction of a stereotypic heart failure associated transcriptional changes in response to neurohormonal agonists³. We used a

siRNA probe to knock down *Sik3* mRNA in NRVM and assayed for characteristics of hypertrophy, with and without hypertrophic stimulation with the alpha 1 adrenergic agonist, phenylephrine (PE). Knockdown of *Sik3* in the absence of PE stimulation resulted in spontaneous induction of cellular hypertrophy and concomitant induction of two canonical heart failure associated transcripts, *Nppa* and *Nppb*⁴ (Figure 3.1A). PE stimulation alone was sufficient to induce a hypertrophic response which was exacerbated with the addition of *Sik3* knockdown (Figure 3.1B), suggesting the existence of SIK3 specific hypertrophic pathways which are not fully activated by PE stimulation.

We next wanted to test whether *Sik3* also represses cardiac hypertrophy in vivo. We generated cardiomyocyte restricted conditional *Sik3* knockout mice by crossing alpha-MHC^{MerCreMer} mice with *Sik3*^{lox/lox} mice. Peritoneal injection of tamoxifen led to efficient depletion of SIK3 protein in the cardiomyocyte fraction of the murine heart, as measured by western blotting. alpha-MHC^{MerCreMer}; *Sik3*^{lox/lox} (*Sik3* cKO) and control alpha-MHC^{MerCreMer}; *Sik3*^{+/+} (Cre) mice were subjected to either sham surgery or pressure overload induced heart failure by transverse aortic constriction (TAC). Using non-invasive serial echocardiography, we did not observe a significant change in left ventricular systolic function, as measured by fractional area change, between Cre and *Sik3* cKO cohorts in either sham or TAC conditions across the 6 week period following surgical intervention. After 6 weeks of banding, Cre and *Sik3* cKO mouse hearts were harvested and assayed for hallmarks of pathologic remodeling and hypertrophy. *Sik3* cKO mice exhibited significant cardiomegaly (measured as a ratio of heart weight to tibia length) compared to their Cre controls under both sham and TAC conditions (Figure 3.1C and D). Concordant

with increased heart weight, Sik3 cKO mice exhibited additional enhanced features of heart failure compared to Cre controls, such as increased cardiac hypertrophy (Figure 3.1E), and increased LV fibrosis (Figure 3.1F). Taken together, these data support the assertion that SIK3 functions as a negative regulator of cardiac hypertrophy in vitro and in vivo.

Unbiased transcriptional and proteomic profiling of Sik3 knockdown cells

To determine the mechanism by which Sik3 represses hypertrophy, we turned to unbiased transcriptional profiling by bulk RNA sequencing in siSik3 treated NRVMs. In an effort to dissect Sik3 specific transcriptional effects from transcriptional changes associated with a general hypertrophic cell state, we performed clustering analysis to ascertain clusters where the directionality of transcriptional changes were concordant in both siSik3 and siSik3 + PE treated conditions but remained unaffected in the scramble conditions. We identified two clusters, cluster 4 and cluster 7, that represented genes uniquely downregulated and upregulated with Sik3 knockdown, respectively. (Figure 3.2A) Transcripts downregulated by Sik3 knockdown in cluster 4 were determined by Gene Ontology analysis to be enriched for genes involved in protein ubiquitination whereas transcripts enriched by Sik3 knockdown in cluster 7 were involved in hypertrophic cardiomyopathy. We interpret these Sik3 specific transcriptional changes to be concordant with the anabolic, hypertrophic phenotype observed in both cultured cardiomyocytes and Sik3 cKO mice.

We then performed abundance and phospho-enriched proteomics on lysates generated from siSik3 treated NRVMs (Figure 3.2B and C). Given that SIK3 harbors intrinsic kinase activity and function, we reasoned that identifying targets which lose phosphorylation status in the setting of Sik3 knockdown may represent novel substrates of SIK3 kinase activity. Importantly, abundance proteomics would also allow us to determine whether the changes in protein phosphorylation status reflect a specific loss of phosphorylation versus general depletion of total protein levels. After clustering analysis we focused our attention on cluster 5 of the phospho-enriched proteomics dataset, which represents proteins which lost phosphorylation in the setting of Sik3 knockdown. In this cluster, the most highly differential phospho-protein signal was due to lower detection of phosphorylated ARHGAP21 at Serine 621 in the Sik3 knockdown condition compared to scramble control (Figure 3.2D). This finding was particularly striking, as a prior study interrogating the interactome of wild-type and a constitutively active mutant of SIK3 in the mouse brain identified ARHGAP21 as an interacting partner of SIK3⁵. Notably, we were unable to detect ARHGAP21 in the abundance proteomics dataset. This is likely due to the relatively low abundance of ARHGAP21 protein in the total cellular lysate. Enrichment of phosphorylated peptides reduces the sample complexity, allowing for lower abundance phosphorylated proteins, such as ARHGAP21, to become readily detectable.

To determine whether the loss of ARHGAP21 pSer621 signal resulted from a decrease in phosphorylation status or in total protein abundance levels, we performed western blotting using an antibody against ARHGAP21 in NRVM lysates treated with Sik3 siRNA (Figure 3.3A). We found that ARHGAP21 protein levels were dramatically depleted in the

setting of Sik3 knockdown, suggesting an unexpected role for SIK3 in regulating ARHGAP21 protein abundance. *Arhgap21* transcript levels were slightly decreased in Sik3 knockdown conditions but were not concordant with the magnitude of effect observed at the protein level, suggesting that SIK3-mediated regulation of ARHGAP21 may predominantly occur in a post-transcriptional manner (Figure 3.3B). To test whether SIK3 regulates protein stability, we concomitantly treated NRVM with siRNA against Sik3 and a proteasome inhibitor, bortezomib (BZ). Treating NRVM with bortezomib rescued the Sik3 knockdown mediated depletion of ARHGAP21 protein levels, indicating that SIK3 plays a critical role in maintaining stability of ARHGAP21 protein (Figure 3.3C).

ARHGAP21 is a negative regulator of cardiac hypertrophy

To our knowledge, the role of ARHGAP21 in regulating cardiac hypertrophy and remodeling has not been previously explored. As our data demonstrate that SIK3 is a negative regulator of cardiac hypertrophy and plays a critical role in stabilizing ARHGAP21 protein levels, we hypothesized that ARHGAP21 may also function as a negative regulator of pathologic cardiac remodeling. We found that siRNA-mediated knockdown of ARHGAP21 induced significant hypertrophy and expression of heart failure associated genes, *Nppa* and *Nppb* (Figure 3.3D and E). To establish a causal link between SIK3 and ARHGAP21, we tested whether reconstitution of ARHGAP21 in the setting of Sik3 knockdown would blunt the hypertrophic effects of Sik3 loss of function. To this end, we generated adenovirus overexpressing ARHGAP21 (Ad-21) or GFP (Ad-GFP) and infected NRVM followed by treatment with Sik3 or scramble siRNAs. Reconstitution of ARHGAP21 was sufficient to significantly blunt the hypertrophy induced

by Sik3 knockdown (Figure 3.3F and G), supporting a model in which SIK3 functions to repress hypertrophy and maintain cardiac homeostasis in part through stabilization of ARHGAP21 protein levels.

Loss of ARHGAP21 leads to nuclear enrichment of MRTF-A

Our data show that ARHGAP21 is a negative regulator of cardiac hypertrophy. Extensive studies have demonstrated that ARHGAP21 functions as a Rho GTPase activating protein, functioning as a molecular switch to inactivate the Rho family of small GTPases⁶⁻⁸. One of the well-established functions of the Rho GTPases is to promote actin polymerization, serving as a tight regulator of monomeric G-actin levels in the cytoplasmic milieu. Previous studies have demonstrated that the activity of a unique transcription factor called myocardin related transcription factor A (MRTF-A) is regulated through a nuclear-cytoplasmic shuttling mechanism that is sensitive to the levels of free monomeric G actin in the cytoplasm^{9,10}. In basal conditions, monomeric G actin levels exist at a steady state and bind to MRTF-A in the cytoplasm, preventing its translocation into the nuclear compartment. When actin polymerization is triggered, G actin levels are depleted as the actin monomers are converted into filamentous F actin. This drop in monomeric G actin levels consequently permits the nuclear translocation of MRTF-A into the nuclear, where it can bind to cardiac co-factors such as serum response factor (SRF) to transactivate a subset of hypertrophic cardiac gene programs^{11,12}. We hypothesized that cardiac hypertrophy induced by Arhgap21 knockdown may be a result of altered actin dynamics and MRTF-A localization. To test whether MRTF-A may be implicated in this process, we started by interrogating the spatial localization of MRTF-A in NRVMs in Sik3

or Arhgap21 knockdown settings. After treating NRVMs with siRNAs against Sik3 or Arhgap21, we performed nuclear/cytoplasmic fractionation of the cellular lysates and probed for MRTF-A protein levels by western blotting. Consistent with our hypothesis, we observed nuclear enrichment of MRTF-A in both Sik3 and Arhgap21 knockdown conditions (Figure 3.4A and B). To further test whether this nuclear enrichment of MRTF-A contributed to the hypertrophic phenotype, we performed concomitant knockdown of Mrtf-a with Sik3 or Arhgap21 using siRNA probes. We found that knockdown of Mrtf-a was sufficient to robustly blunt Sik3 and Arhgap21 knockdown-mediated hypertrophy and induction of *Nppa* and *Nppb* (Figure 3.4 C and D), suggesting a causal link between MRTF-A and SIK3/ARHGAP21.

Discussion

Our previous study implicated a novel role for the SIK family of kinases in regulating cardiac plasticity and demonstrated that SIK1 functions as a positive regulator of cardiac hypertrophy and remodeling². Our current study builds on our initial findings and has elucidated an antithetical role for another SIK family member in the regulation of cardiac homeostasis, implicating SIK3 as a repressor of hypertrophy and remodeling. Through unbiased phospho-proteomic profiling, we uncovered ARHGAP21 as an effector of SIK3 signaling that, in part, serves to tightly regulate actin dynamics and downstream hypertrophic transcriptional programs. Our data demonstrate a role for SIK3 in regulating ARHGAP21 protein stability, implicate this axis as part of an anti-hypertrophic signaling node, and provide new insight into the last uncharacterized SIK isoform expressed in the mammalian heart.

SIK3 represses cardiac hypertrophy

Specific knockdown of Sik3 in cultured cardiomyocytes or condition genetic deletion in the adult mouse led to the induction of cardiac hypertrophy and canonical features of heart failure. This is a clear departure from the pro-hypertrophic effects of SIK1 we previously observed. Despite sharing near identical kinase domains and consequence target sequences^{1,13}, the functional effect of Sik1 and Sik3 knockdown are in opposition to one another. To what extent SIK1 and SIK3 share overlapping or distinct targets would be interesting to explore and would be best facilitated by the engineering of SIK1 and SIK3 mutants capable of utilizing radiolabeled bulky-analog ATP¹⁴. Additionally, epistatic experiments involving dual knockout or knockdown of Sik1 and Sik3 would shed light on the mechanistic relationship between these two proteins and whether therapeutic targeting of salt-inducible kinases for heart failure therapy would require generation of isoform specific SIK inhibitors.

SIK3 regulates ARHGAP21 stability

Our unbiased phospho-proteomic profiling uncovered a subset of proteins which lost phosphorylation status in the setting of Sik3 knockdown. It is possible that novel direct substrates of SIK3 activity are represented in this subset of identified proteins. As the consensus sequence for SIKs has been mapped¹⁵, we had sought to determine whether ARHGAP21 contained any putative SIK3 motifs that could be candidate for direct phosphorylation. Interestingly, we were unable to detect any motifs that matched the kinase consensus sequence, which raise two possibilities: (1) SIK3 does not directly

phosphorylate ARHGAP21 or (2) SIK3 phosphorylates ARHGAP21 on a non-consensus motif. Future studies utilizing biochemical approaches and in vitro kinase assays would be important to understanding the mechanistic biochemical link between SIK3 and ARHGAP21. It is also unclear whether phosphorylation of ARHGAP21 is critical for its stability. While we have shown that knockdown of SIK3 leads to degradation of ARHGAP21 in a proteasome dependent manner, it is unclear whether the loss of a phosphorylation event is responsible for driving the destabilizing effect. Generation of phospho-deficient point mutants of ARHGAP21 would shed light on the importance of phosphorylation for maintaining ARHGAP21 stability.

ARHGAP21 represses cardiac hypertrophy

The Rho family of small GTPases encompassing Rho, Rac, and Cdc42 have been well established as molecular switches of many key cellular processes such as cytoskeletal organization, muscle contraction, cell cycle progression, proliferation, and differentiation¹⁶. Of the three, RhoA has been most extensively studied in the context of cardiac hypertrophy and remodeling, yet its definitive role in regulating pathologic remodeling in the heart has been difficult to ascertain due to conflicting results from various studies that demonstrate both cardioprotective¹⁷ and detrimental¹⁸⁻²⁰ effects. Cdc42 has previously been noted as an antihypertrophic regulator²¹ whereas Rac1 has been demonstrated to be a pro-hypertrophic regulator in the heart²². One of the proteins of focus in our study, ARHGAP21, has been shown to negatively regulate all three members of the Rho family⁷. While our data have demonstrated a link between ARHGAP21 expression levels and MRTF-A localization, it will be important to interrogate

the activation levels of Rho, Rac, and Cdc42 to better understand which Rho GTPases are most sensitive to ARHGAP21 depletion. These data also raise the question of why depletion of ARHGAP21 has such a dramatic effect on cardiac hypertrophy, when there exists over 60 identified mammalian RhoGAP containing proteins. The lack of functional redundancy observed in our NRVM model suggests specialized roles for each RhoGAP protein, despite the shared sequence homology. These data pointing to ARHGAP21 as a negative regulator of hypertrophy also suggest that its functionally antithetical family of proteins, Rho guanine nucleotide exchange factors (RhoGEFs) may function as positive regulators of this process. Indeed, evidence implicating RhoGEF12 as a positive driver of cardiac remodeling have been published and suggest that targeting of regulators upstream of Rho GTPases may be a source of potential novel therapeutic targets in the treatment of heart failure.

In summary, we have uncovered a role for the last uncharacterized SIK isoform expressed in the mammalian heart and demonstrated its function as a negative regulator of cardiac hypertrophy and pathologic gene induction in rodent cardiomyocytes, in part through its ability to regulate ARHGAP21 protein stability. We establish a new role for ARHGAP21 as an antihypertrophic effector in cardiomyocytes and an important upstream regulator of MRTF-A localization and activity. These data uncover a SIK3-ARHGAP21 signaling axis that is necessary for proper maintenance of cardiac homeostasis in both cultured cardiomyocytes and adult mice.

Figures

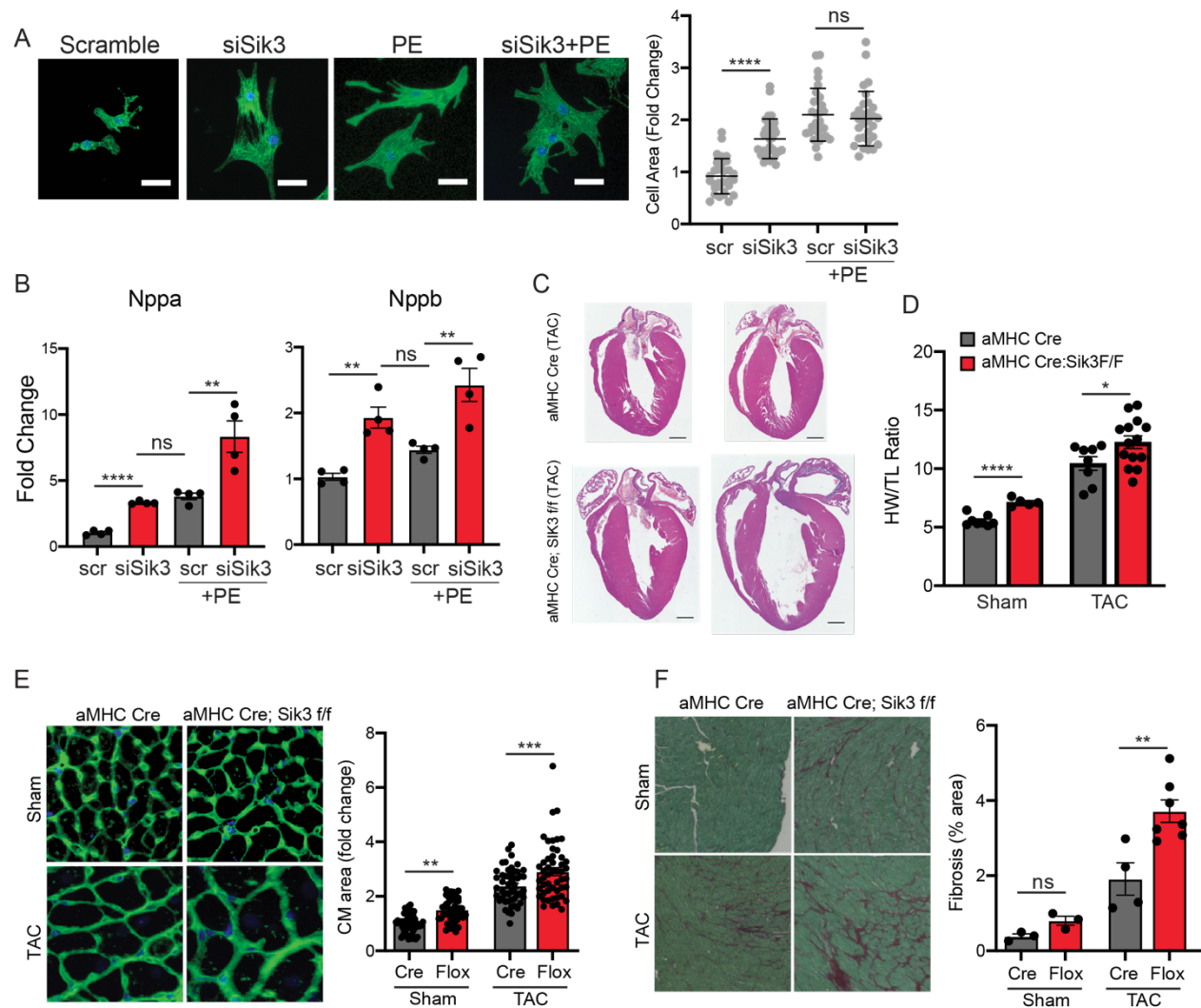


Figure 3.1. SIK3 represses pathologic cardiac remodeling in vitro and in vivo. (A) NRVM immunostained for α -actinin (green) and nuclei (blue) Scale = 40um. Cell area quantification on right, n=30. (B) qRT-PCR expression for canonical heart failure associated genes. (n=4). (C) Four chamber heart sections stained with H&E. Scale = 1mm. (D) Heart weight to tibial length ratio. (n=5-8 for sham, n=8-14 for TAC). (E) Wheat germ agglutinin staining of heart sections (n=50). (F) Picosirius red staining of heart sections (n=3 for sham, n=4-7 for TAC). Data are shown as means + SEM unless noted. * $P < 0.05$, ** $P < 0.01$, *** $P < 0.001$, **** $P < 0.0001$ by one-way ANOVA with Tukey's multiple comparisons test.

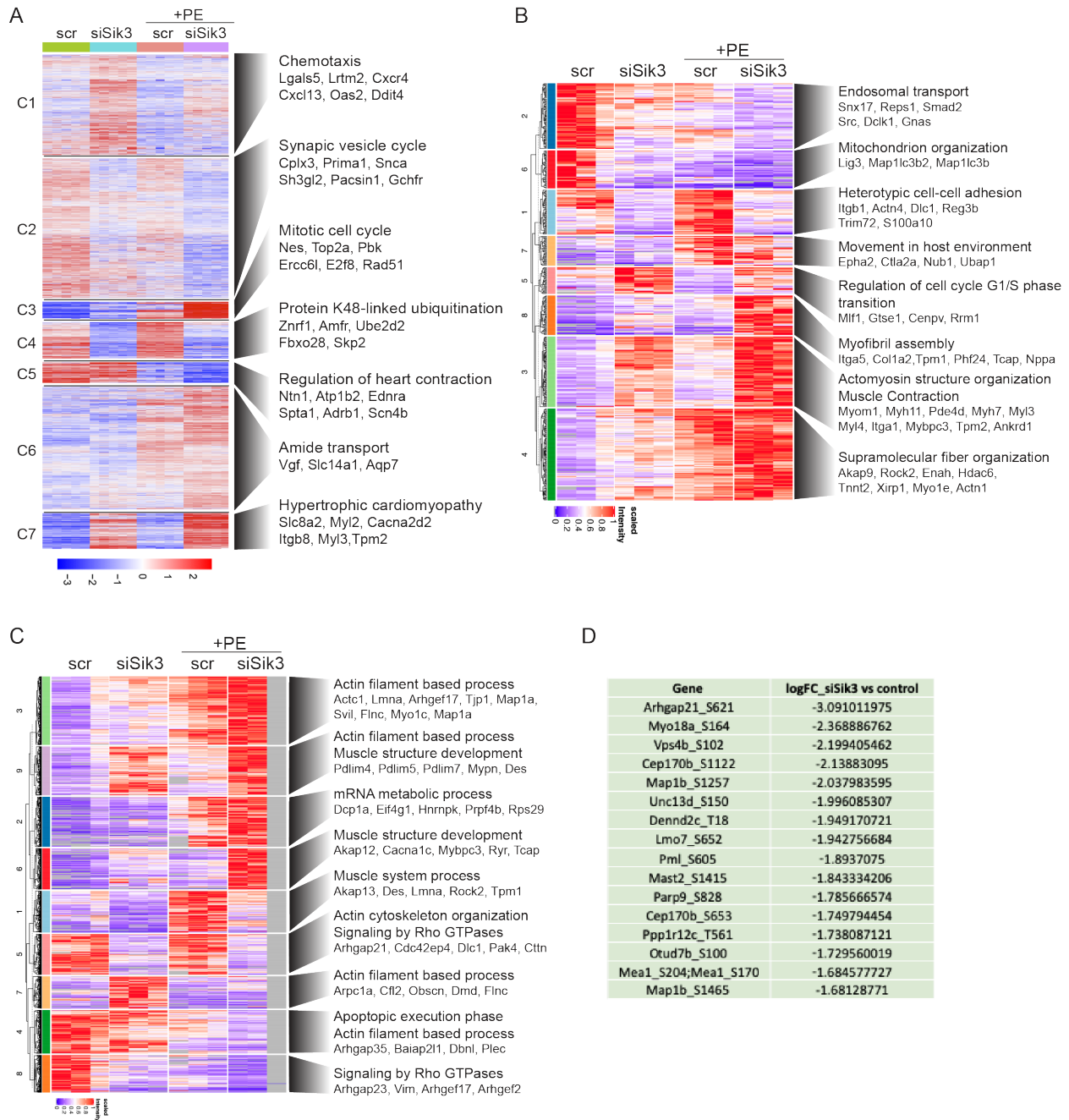


Figure 3.2. Global transcriptional and proteomic profiling of Sik3 knockdown in NRVM. (A) Heatmap showing clustered, row normalized genes from bulk RNA-sequencing of NRVM treated with siRNA against Sik3 (n=5 per condition). (B) Total abundance proteomics and (C) Phospho-enriched proteomics of NRVM treated with siRNA against Sik3. n=3 for all conditions except for siSik3 + PE, phosphoproteomics. n=2). (D) Top phospho peptide hits from cluster 5 in (D), ranked by ascending logFC.

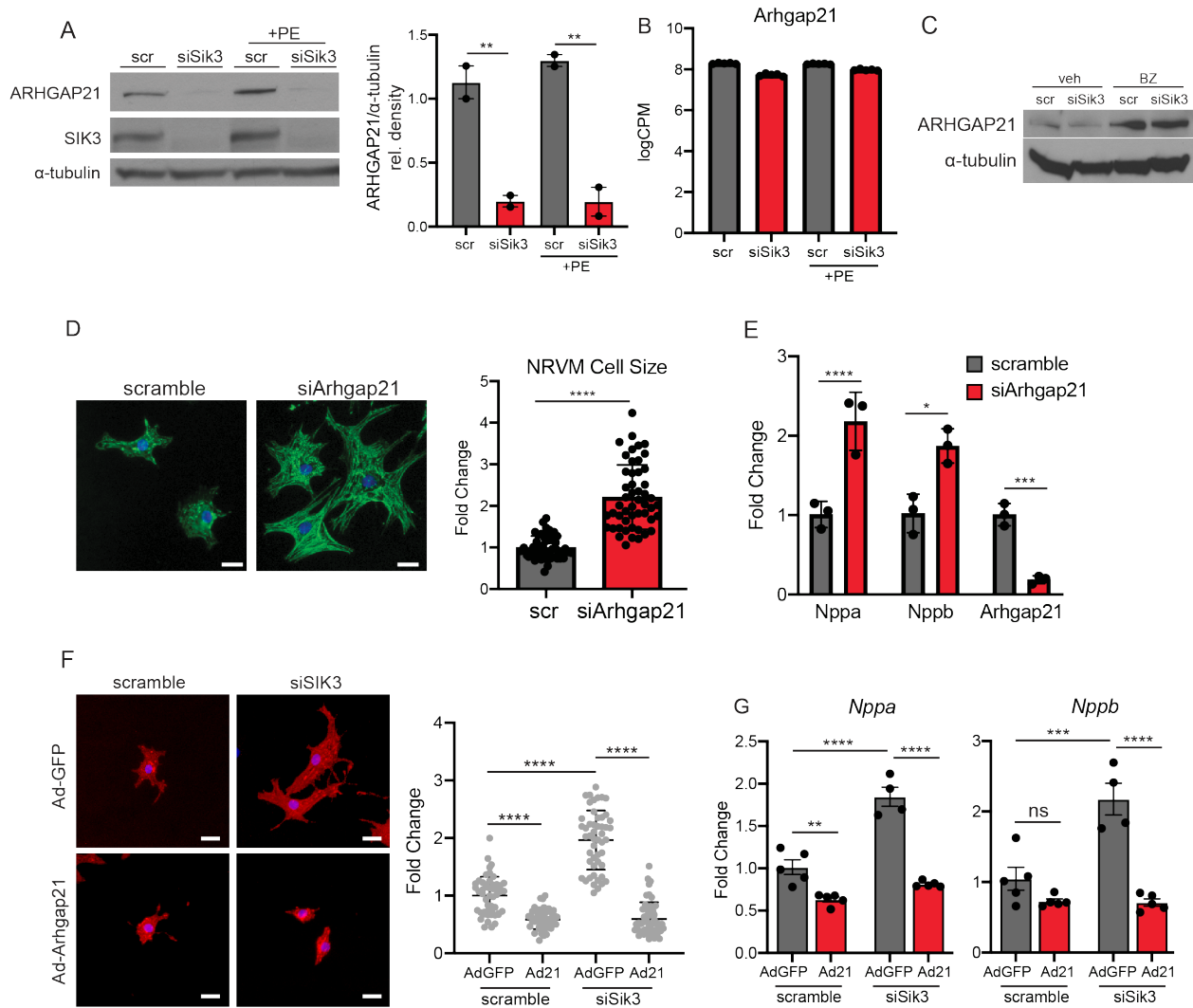


Figure 3.3. SIK3 regulates ARHGAP21 stability to repress pathologic cardiac remodeling. (A) Western blotting of ARHGAP21 from NRVM lysates treated \pm siRNA against Sik3 and \pm PE. Densitometry on right. (B) logCPM values of Arhgap21 derived from bulk RNA-seq in Figure 3.2A. (C) Western blotting of ARHGAP21 from NRVM lysates treated \pm siRNA against Sik3 and \pm bortezomib (BZ, 5nM for 16 hours). (D) NRVM immunostained for α -actinin (green) and nuclei (blue) Scale = 40um. Cell area quantification on right, n=50. (E) qRT-PCR expression for canonical heart failure associated genes. (n=3). (F) NRVM immunostained for α -actinin (red) and nuclei (blue) Scale = 40um. Cell area quantification on right, n=50. (G) qRT-PCR expression for canonical heart failure associated genes. (n=4-5). Data are shown as means + SEM unless noted. *P<0.05, **P<0.01, ***P<0.001, ****P<0.0001 by one-way ANOVA with Tukey's multiple comparisons test.

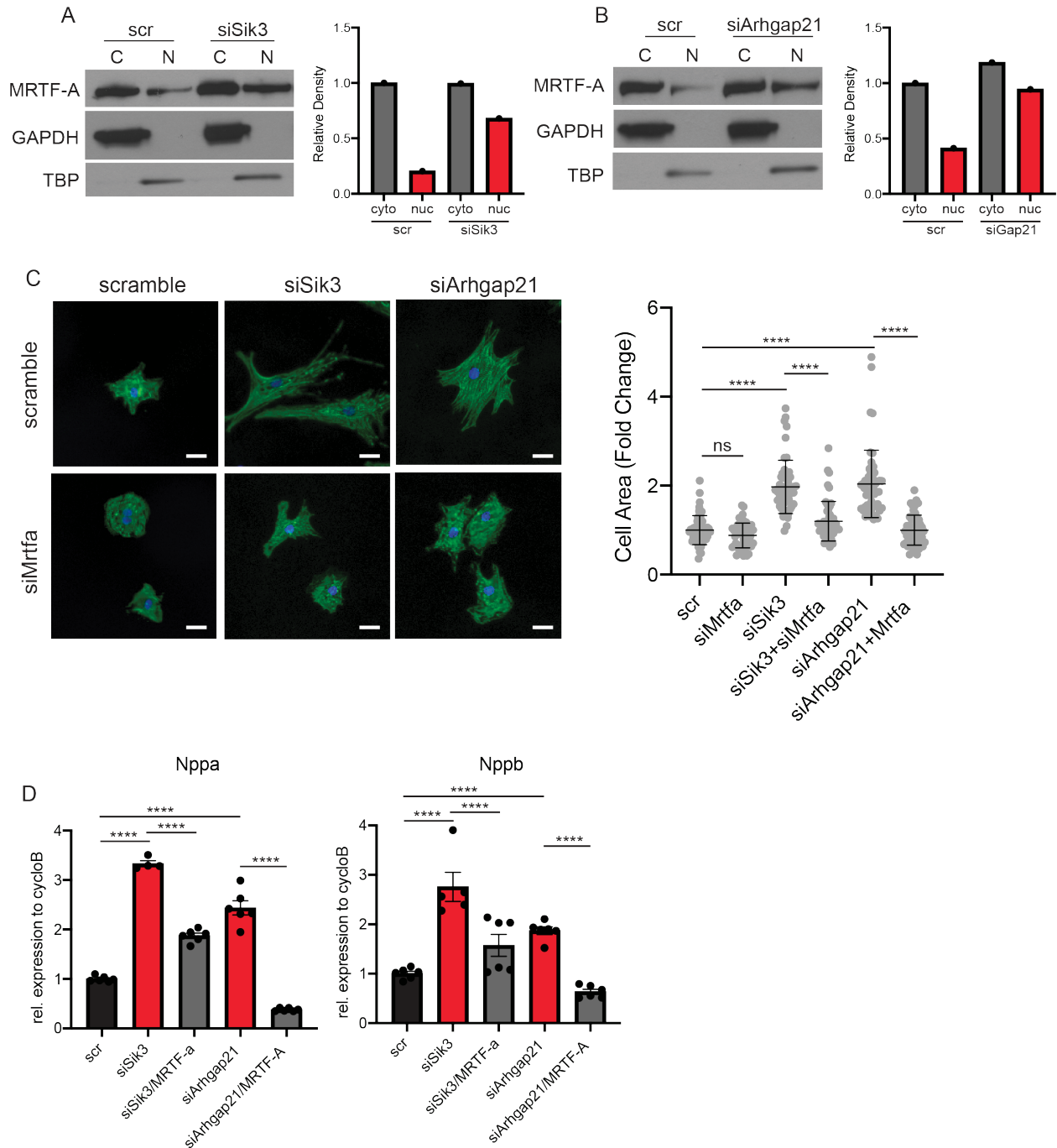


Figure 3.4. Nuclear enrichment of MRTF in siSik3 and siArhgap21 NRVMs. Western blotting of MRTF-A in cytoplasmic (C) and nuclear (N) fractions of NRVM treated with siRNA against (A) Sik3 or (B) Arhgap21. (C) NRVM immunostained for α -actinin (green) and nuclei (blue) Scale = 40um. Cell area quantification on right, n=50. (D) qRT-PCR expression for canonical heart failure associated genes. (n=6). Data are shown as means + SEM unless noted. *P<0.05, **P<0.01, ***P<0.001, ****P<0.0001 by one-way ANOVA with Tukey's multiple comparisons test.

Methods

NRVM isolation and culture

Neonatal rat ventricular myocytes (NRVM) were isolated as previously described². Briefly, hearts from 1-2 day old Sprague-Dawley Rat pups were harvested, atria removed, and mechanically digested into 1-2 mm sized pieces of tissue. Tissue was digested in 0.25% Trypsin-EDTA overnight at 4C. After overnight digestion, cardiomyocytes were isolated using 10 minute serial digestions with 300U/mL Collagenase II (Worthington) until no tissue remained. Cells were preplated on 15cm plates for 2-3 hours to remove fibroblasts. The remaining NRVM were seeded in feeding medium (DMEM, 5% FBS, 100U/mL Pen/Strep, 100uM BrdU) for 48 hours. NRVM were then washed with PBS w/o Ca²⁺ or Mg²⁺ and replaced with fresh starving media (DMEM, 0.1% BSA, 100U/mL Pen/Strep, 1:100 ITS, 10uM BrdU).

Conditional deletion of SIK3 with tamoxifen

Tamoxifen (Sigma) solution was dissolved overnight at 37C in corn oil at a concentration of 20mg/mL. Mice were injected intraperitoneally with 75mg/kg of tamoxifen at 28 weeks of age, for 3 consecutive days.

Mouse Echocardiography

Mice were anesthetized with 1% inhalational isoflurane and imaged using the Vevo 770 High Resolution Imaging System (FujiFilm VisualSonics Inc.) and the RMV-707B 30-MHz probe. Measurements were obtained from M-mode sampling and integrated

electrocardiogram-gated kilohertz visualization (EKV) images taken in the LV short axis view at the mid-papillary muscle level as previously described²³.

Histology and Immunofluorescence

For NRVM studies, cells were plated on glass coverslips coated with 0.1% gelatin. Cells were fixed in 2% paraformaldehyde for 20 minutes at room temperature, with gentle rocking. Fixed cells were permeabilized in PBST + 0.1% Triton X for 20 minutes, blocked in PBST + 5% horse serum for 1 hour, and incubated with primary antibody against alpha actinin (Sigma, A7811) diluted at 1:800 in PBST + 5% horse serum for 1 hour at room temperature with gentle rocking. Cells were washed 3X with PBST followed by incubation with secondary antibody diluted to 1:1000 in PBST + 5% horse serum at room temperature for 1 hour. Cells were washed 3x with PBST and mounted with Vectashield Hardset mounting media with DAPI.

For cardiac tissues samples, mid-ventricular short axis cross sections were fixed overnight in 10% neutral buffered formalin at 4C with gentle rocking. Samples were washed with PBS and transferred to 70% ethanol for 24 hours. Samples were embedded in paraffin blocks, sectioned, and stained with wheat germ agglutinin 488 (Thermo Fisher, 11261) or Picrosirius Red (Polysciences) according to manufacturers' instructions. Quantification of cardiomyocyte cross sectional area and fibrosis area were quantified as previously described²³.

Adenovirus generation and titering

Adenoviruses were generated as previously described². Briefly, full length Arhgap21 containing plasmid was obtained from Origene (NM_020824). Arhgap21 was cloned into the Gateway Entry vector pENTR2B using the Gibson Assembly strategy, followed by LR recombination into the Gateway destination vector pAd-CMV-V5-DEST. Sequence verified plasmid was linearized and transfected into 293A cells according to manufacturer's protocol. Cells were incubated for up to 2 weeks to allow for plaque formation and complete lysis of the culture plate. Crude lysate was harvested and sterile filtered using a 0.22µm syringe filter (Millipore EMD). 293A cells were plated in 6 well plates, infected with serial dilutions of crude lysate, and overlaid with SeaPlaque Agarose to allow for localized plaque formation. Individual plaques were observed, isolated, and amplified prior to testing for ARHGAP21 protein expression. Plaques demonstrating strong expression were further amplified using 293A cells and titered using a plaque formation assay.

To infect NRVM, cells were incubated with ARHGAP21 adenovirus or GFP control at an MOI of 1 in low volumes of serum free media for 2-3 hours with gentle rocking every 30 minutes. NRVM were washed with PBS without Ca²⁺ or Mg²⁺ and cultured in fresh serum free media.

RNA Sequencing

A bioinformatics tool, Nextflow version 20.04.1 and nf-core/rnaseq version 1.4.2, was used to preprocess and perform sequence alignments (<https://doi.org/10.5281/zenodo.1400710>). The input sequence was formatted as FASTQ

and gene-level counts were estimated using NCBI GTF gene annotation. Trim-galore (http://www.bioinformatics.babraham.ac.uk/projects/trim_galore/) was used to remove contaminated adapters and low-quality regions and the sequence quality was calculated and controlled with FastQC (<http://www.bioinformatics.babraham.ac.uk/projects/fastqc>). Then sequence reads were aligned to the Rnor6 reference assembly using STAR 2.6.1d²⁴ and gene-level counts were measured using "featureCounts"²⁵, part of the Subread suite (<http://subread.sourceforge.net/>). Gene filtering was performed based on a threshold of at least 5 (raw) reads in at least 2 samples prior to performing differential expression gene analysis. After filtering, the expression values were re-normalized using calcNormFactors in EdgeR.

The design matrix modeled for Sik3 siRNA treatment, PE stimulation, and the interaction of these two, and additionally we controlled for batch effect was controlled by including a batch variable in the model. Gene-wise dispersion values for the DEG model were estimated using a quasi-likelihood (QL) method implemented in glmQLFit in EdgeR²⁶ then an empirical Bayes quasi-likelihood F-based test (glmQLFTest) was used to find DEGs²⁷. Significant DEGs were determined based on an FDR threshold of 0.05.

To visualize the genes' expression patterns, genes that passed the 0.05 FDR threshold were clustered using the R package hopach and $\log_2(\text{Counts Per Million} + 1)$ values were used to make a heatmap using the pheatmap package (<https://CRAN.R-project.org/package=pheatmap>). Principal Component Analysis was performed using the R function prcomp.

Cell lysis and digestion for proteomics

Cells were lysed in 6M Guanidine HCl in 100mM Tris-HCl (pH = 8) followed by heating at 95 degrees for 5 min. DNA was sheared via probe sonication, on ice, at 20% amplitude for 20 seconds, followed by 10 seconds of rest. This process was repeated three times.

Following sonication, protein concentration was determined using Bradford assay. Disulfide bond reduction and carbamidomethylation of cysteines was performed by the addition of a 1:10 volume of reduction/alkylation buffer (100 mM tris(2-carboxyethyl)phosphine (TCEP) and 400 mM 2-chloroacetamide (CAA)) to the lysate. Samples were then incubated for 5 min at 45 °C with shaking (1500 rpm). Samples were then diluted with 100mM Tris-HCl (pH = 8) to a final urea concentration of 1M Guanidine HCl. Trypsin (Promega) and LysC (xx) were added at a 1:100 (enzyme:protein w:w) ratio and digested overnight at 37°C with rotation.

Following digestion, 10% trifluoroacetic acid (TFA) was added to each sample to a final pH ~2. Samples were desalted under vacuum using Sep Pak tC18 cartridges (Waters). Each cartridge was activated with 1 mL 80% acetonitrile (ACN)/0.1% TFA, then equilibrated with 3 × 1 mL of 0.1% TFA.

Following sample loading, cartridges were washed with 4 × 1 mL of 0.1% TFA, and samples were eluted with 4 × 0.5 mL 50% ACN/0.25% formic acid (FA). Samples were dried by vacuum centrifugation and resuspended in 0.1% TFA in 80% ACN. 50 µg of each sample was kept for protein abundance measurements, and the remainder was used for phosphopeptide enrichment.

Phosphopeptide enrichment

Phosphopeptide enrichment was performed on the Kingfisher Flex in 96-well plate format. For each sample, 75 μ L of 5% IMAC bead slurry (QIAGEN) was added to a 2 mL bio-spin column. Beads were incubated with 4 \times 500 μ L of 100 mM EDTA for 30 s, washed with 2 \times 500 μ L H₂O, incubated 4 \times 500 μ L with 15 mM FeCl₃ for 1 minute, washed 3 \times 500 μ L H₂O, and washed once with 500 μ L of 0.5% FA to remove residual Fe. Beads were resuspended in phosphopeptide binding solution to create a 5% IMAC bead slurry and 75 μ L were aliquoted into corresponding wells on a 96-well plate. Additional 75 μ L of 0.1% TFA in 80% ACN were added to each well. Digested peptide mixtures in 0.1% TFA in 80% ACN were incubated with beads followed by 3 washes of the beads with 150 μ L 0.1% TFA in 80% ACN. Phosphopeptides were eluted by incubating the beads with 50 μ L elution buffer (50:50 Acetonitrile: (1:20) ammonium hydroxide/water). The eluted phosphopeptides were then mixed with 30 μ L of 10% FA in 75% ACN solution and the peptide mix was transferred to C18 spin columns (Nest group), centrifuged for 1 min to elute the peptides and dried by vacuum centrifugation.

Mass spectrometry data acquisition

Digested samples were analyzed on an Orbitrap Exploris 480 mass spectrometry system (Thermo Fisher Scientific) equipped with an Easy nLC 1200 ultra-high pressure liquid chromatography system (Thermo Fisher Scientific) interfaced via a Nanospray Flex nanoelectrospray source. For all analyses, samples were injected on a C18 reverse phase column (25 cm \times 75 μ m packed with ReprosilPur 1.9 μ m particles). Mobile phase A consisted of 0.1% FA, and mobile phase B consisted of 0.1% FA/80% ACN. Peptides

were separated by an organic gradient from 5% to 30% mobile phase B over 112 minutes followed by an increase to 58% B over 12 minutes, then held at 90% B for 16 minutes at a flow rate of 350 nL/minute. Analytical columns were equilibrated with 6 μ L of mobile phase A. Data-independent analysis (DIA) was performed on all samples. An MS scan at 60,000 resolving power over a scan range of 390-1010 m/z, a normalized AGC target of 300%, an RF lens setting of 40%, and a maximum injection time of 60 ms was acquired, followed by DIA scans using 8 m/z isolation windows over 400-1000 m/z at a normalized HCD collision energy of 27%. Loop control was set to All.

For phosphopeptide enriched samples, data were collected using a resolving power of 30,000 and a maximum ion injection time of 40 ms. Protein abundance samples were collected using a resolving power of 15,000 and a maximum ion injection time of 22 ms. DIA data analysis was performed using the Pulsar search engine integrated into Spectronaut by searching against a database of Uniprot *Rat* sequences, including reviewed Swiss-Prot and unreviewed TrEMBL entries (downloaded July, 2020). For protein abundance samples, data were searched using the default BGS settings, variable modification of methionine oxidation, static modification of carbamidomethyl cysteine, and filtering to a final 1% false discovery rate (FDR) at the peptide, peptide spectrum match (PSM), and protein level. No data normalization was performed. For phosphopeptide enriched samples, BGS settings were modified to include phosphorylation of S, T, and Y as a variable modification and the Significant PTM default settings were used, with no data normalization performed, and the DIA-specific PTM site localization score in Spectronaut was applied.

Mass spectrometry data analysis

Peptide ion intensities from Spectronaut were summarized and processed to detect significant differences between treatments using the R (version 3.6.1) packages artMS (version 1.5.3) and MSstats (version 3.19.5, <https://pubmed.ncbi.nlm.nih.gov/24794931/>). For abundance proteomics, log transformed intensities from all peptides were first normalized between samples using a standard equalize-medians procedure modified so that normalizing factors were calculated using only the peptides with no missing value in any samples. The normalized peptide intensities were then grouped and summarized per protein. For phosphoproteomics, peptides were grouped according to the standard artMS procedure which combines peptides with matching phosphorylated site(s). The summarized intensities (per protein or per combination of intra-peptide phosphorylations) were analyzed by MSstats, which performs linear regressions on each protein or phosphorylation combination treating the conditions as independent categorical variables and log transformed intensity as the response variable. P values were adjusted for multiple tests using the Benjamini-Hochberg procedure for estimating the false discovery rate. Proteins and phosphorylations were considered significantly regulated between conditions if their adjusted p value was less than 0.05 for at least one pairwise contrast, and absolute log₂ fold change was greater than 1.0. The per-replicate intensity patterns of significantly regulated phosphorylations and proteins were clustered using the kmeans function in R on linearly scaled intensities (max per protein/phosphorylation = 1.0) and 100 random starts per number of clusters (k) less than 15, with the final k chosen through visual inspection of the explained-variance per k curve.

References

1. Wein, M.N., Foretz, M., Fisher, D.E., Xavier, R.J. & Kronenberg, H.M. Salt-Inducible Kinases: Physiology, Regulation by cAMP, and Therapeutic Potential. *Trends Endocrinol Metab* **29**, 723-735 (2018).
2. Hsu, A., *et al.* Salt-inducible kinase 1 maintains HDAC7 stability to promote pathologic cardiac remodeling. *J Clin Invest* **130**, 2966-2977 (2020).
3. Simpson, P., McGrath, A. & Savion, S. Myocyte hypertrophy in neonatal rat heart cultures and its regulation by serum and by catecholamines. *Circ Res* **51**, 787-801 (1982).
4. Chen, H.H. & Burnett, J.C. Natriuretic peptides in the pathophysiology of congestive heart failure. *Curr Cardiol Rep* **2**, 198-205 (2000).
5. Wang, Z., *et al.* Quantitative phosphoproteomic analysis of the molecular substrates of sleep need. *Nature* **558**, 435-439 (2018).
6. Lazarini, M., *et al.* ARHGAP21 is a RhoGAP for RhoA and RhoC with a role in proliferation and migration of prostate adenocarcinoma cells. *Biochim Biophys Acta* **1832**, 365-374 (2013).
7. Rosa, L.R.O., Soares, G.M., Silveira, L.R., Boschero, A.C. & Barbosa-Sampaio, H.C.L. ARHGAP21 as a master regulator of multiple cellular processes. *J Cell Physiol* **233**, 8477-8481 (2018).
8. Barcellos, K.S., *et al.* ARHGAP21 protein, a new partner of alpha-tubulin involved in cell-cell adhesion formation and essential for epithelial-mesenchymal transition. *J Biol Chem* **288**, 2179-2189 (2013).
9. Mizuguchi, M., *et al.* Transient alpha-helices in the disordered RPEL motifs of the

- serum response factor coactivator MKL1. *Sci Rep* **4**, 5224 (2014).
10. Vartiainen, M.K., Guettler, S., Larijani, B. & Treisman, R. Nuclear actin regulates dynamic subcellular localization and activity of the SRF cofactor MAL. *Science* **316**, 1749-1752 (2007).
 11. Trembley, M.A., *et al.* Mechanosensitive Gene Regulation by Myocardin-Related Transcription Factors Is Required for Cardiomyocyte Integrity in Load-Induced Ventricular Hypertrophy. *Circulation* **138**, 1864-1878 (2018).
 12. Guo, Y., *et al.* Sarcomeres regulate murine cardiomyocyte maturation through MRTF-SRF signaling. *Proc Natl Acad Sci U S A* **118**(2021).
 13. Sundberg, T.B., *et al.* Development of Chemical Probes for Investigation of Salt-Inducible Kinase Function in Vivo. *ACS Chem Biol* **11**, 2105-2111 (2016).
 14. Hertz, N.T., *et al.* Chemical genetic approach for kinase-substrate mapping by covalent capture of thiophosphopeptides and analysis by mass spectrometry. *Curr Protoc Chem Biol* **2**, 15-36 (2010).
 15. Kim, M.J., *et al.* Salt-Inducible Kinase 1 Terminates cAMP Signaling by an Evolutionarily Conserved Negative-Feedback Loop in beta-Cells. *Diabetes* **64**, 3189-3202 (2015).
 16. Hodge, R.G. & Ridley, A.J. Regulating Rho GTPases and their regulators. *Nat Rev Mol Cell Biol* **17**, 496-510 (2016).
 17. Lauriol, J., *et al.* RhoA signaling in cardiomyocytes protects against stress-induced heart failure but facilitates cardiac fibrosis. *Sci Signal* **7**, ra100 (2014).
 18. Kawamura, S., Miyamoto, S. & Brown, J.H. Initiation and transduction of stretch-

- induced RhoA and Rac1 activation through caveolae: cytoskeletal regulation of ERK translocation. *J Biol Chem* **278**, 31111-31117 (2003).
19. Sah, V.P., Hoshijima, M., Chien, K.R. & Brown, J.H. Rho is required for Galphaq and alpha1-adrenergic receptor signaling in cardiomyocytes. Dissociation of Ras and Rho pathways. *J Biol Chem* **271**, 31185-31190 (1996).
 20. Torsoni, A.S., Marin, T.M., Velloso, L.A. & Franchini, K.G. RhoA/ROCK signaling is critical to FAK activation by cyclic stretch in cardiac myocytes. *Am J Physiol Heart Circ Physiol* **289**, H1488-1496 (2005).
 21. Maillet, M., *et al.* Cdc42 is an antihypertrophic molecular switch in the mouse heart. *J Clin Invest* **119**, 3079-3088 (2009).
 22. Satoh, M., *et al.* Requirement of Rac1 in the development of cardiac hypertrophy. *Proc Natl Acad Sci U S A* **103**, 7432-7437 (2006).
 23. Duan, Q., *et al.* BET bromodomain inhibition suppresses innate inflammatory and profibrotic transcriptional networks in heart failure. *Sci Transl Med* **9**(2017).
 24. Dobin, A., *et al.* STAR: ultrafast universal RNA-seq aligner. *Bioinformatics* **29**, 15-21 (2013).
 25. Liao, Y., Smyth, G.K. & Shi, W. featureCounts: an efficient general purpose program for assigning sequence reads to genomic features. *Bioinformatics* **30**, 923-930 (2014).
 26. Robinson, M.D., McCarthy, D.J. & Smyth, G.K. edgeR: a Bioconductor package for differential expression analysis of digital gene expression data. *Bioinformatics* **26**, 139-140 (2010).
 27. Lun, A.T., Chen, Y. & Smyth, G.K. It's DE-licious: A Recipe for Differential Expression

Analyses of RNA-seq Experiments Using Quasi-Likelihood Methods in edgeR.
Methods Mol Biol **1418**, 391-416 (2016).

Chapter 4: Targeting transcription in heart failure via inhibition of CDK7/12/13

Abstract

Heart failure with reduced ejection fraction (HFrEF) is associated with high mortality, highlighting an urgent need for new therapeutic strategies. As stress-activated cardiac signaling cascades converge on the nucleus to drive maladaptive gene programs, interdicting pathological transcription is a conceptually attractive approach for HFrEF therapy. Here, we demonstrate that CDK7/12/13 are critical regulators of transcription activation in the heart that can be pharmacologically inhibited to improve HFrEF. CDK7/12/13 inhibition using the first-in-class inhibitor THZ1 or RNAi blocks stress-induced transcription and pathologic hypertrophy in cultured rodent cardiomyocytes. THZ1 potently attenuates adverse cardiac remodeling and HFrEF pathogenesis in mice and blocks cardinal features of disease in human iPSC-derived cardiomyocytes. THZ1 suppresses Pol II enrichment at stress-transactivated cardiac genes and inhibits a specific pathologic gene program in the failing mouse heart. These data identify CDK7/12/13 as druggable regulators of cardiac gene transactivation during disease-related stress, suggesting that HFrEF features a critical dependency on transcription that can be therapeutically exploited.

Background

Despite current standard of care, heart failure with reduced ejection fraction (HFrEF) remains associated with excessively high mortality and morbidity, highlighting an urgent need for new therapeutic strategies. Several pharmacotherapies for HFrEF that have been proven to improve outcomes, such as beta-adrenergic receptor antagonists and inhibitors of the renin-angiotensin system, typically interdict signaling at or near the plasma membrane. Ultimately, these stress-activated signaling cascades converge on

the nucleus to drive maladaptive changes in gene transcription, which can chronically compromise cardiac function and fuel the vicious cycle of adverse cardiac remodeling and HFrEF pathogenesis¹. As the gene regulatory machinery functions as a nodal integrator of upstream stress signals, drugging specific components of the transcription apparatus represents a conceptually attractive approach to treat HFrEF.

Previous studies have shown that hyperphosphorylation of RNA Polymerase II (Pol II) by multiprotein kinase complexes such as PTEFb (positive transcription elongation factor b) is a hallmark of pathological cardiac stress in rodent models of heart failure and in failing human hearts^{2,3}, prompting us to hypothesize that inhibition of additional upstream Pol II C-terminal domain (CTD) kinase complexes such as TFIIH could attenuate pathologic transcription during HFrEF pathogenesis. THZ1 is a first-in-class small molecule inhibitor of CDK7 (Cyclin dependent kinase 7), a core kinase in the eukaryotic TFIIH complex upstream of Pol II CTD phosphorylation. THZ1 covalently binds Cysteine-312 on CDK7 at a site spatially distinct from the catalytic pocket, resulting in potent allosteric inhibition of CDK7 kinase activity⁴. THZ1 also inhibits two related Pol II CTD kinases, CDK12 and CDK13, by covalently binding accessible cysteine residues that are homologous to C312 of CDK7⁴. Preclinical studies across a broad array of tumor types have demonstrated that THZ1 can potently suppress transcription of gene programs that drive cancer progression⁴⁻¹⁰. These studies prompted us to explore the role of CDK7/12/13-dependent transcription in HFrEF pathogenesis. Here, we show that inhibition of CDK7/12/13-dependent transcription confers protection against the establishment of HFrEF in cultured

cardiomyocytes and adult mice, providing proof of concept that pathologic transcription activation may be therapeutically exploited to attenuate heart failure.

Results

CDK7/12/13 inhibition in cultured cardiomyocytes inhibits the hypertrophic stress response

We began by studying the effects of inhibiting CDK7/12/13-dependent Pol II CTD phosphorylation via THZ1 (structure shown in Figure 4.1A) in cultured neonatal rat ventricular myocytes (NRVM), a well-established in vitro system to probe adverse cardiomyocyte remodeling¹¹. THZ1 treatment potently attenuated α 1-adrenergic agonist (phenylephrine, PE)-induced cellular hypertrophy (Figure 4.1B) and induction of *Nppa* and *Nppb*, two hallmark markers of pathological cardiomyocyte stress (Figure 4.1C). To determine a specific role for cardiomyocyte CDK7/12/13 activity on phosphorylation of specific serine residues in the C-terminal heptapeptide repeats of Pol II^{12,13}, we performed Western blots using phospho-serine specific Pol II antibodies. We observed increased levels of Ser2P, Ser7P and Ser5P Pol II phosphoforms during PE-mediated hypertrophic stress (Figure 4.1D), consistent with increased Pol II CTD phosphorylation in this setting. THZ1 attenuated the PE-dependent increase in Ser2P and Ser7P (Figure 4.1D). We did not observe a significant effect on bulk abundance of Ser5P in cardiomyocytes, which may reflect redundant regulation of this phosphoform by other Pol II CTD kinases¹⁴⁻¹⁷. The IC₅₀ of THZ1 in these cardiomyocyte assays was 5-10nM, which reflects a sensitivity to THZ1 that is higher than what has been observed in studies of growth inhibition of several cancer cell types^{5-9,18-26} (Supplemental Figure 4.1A). Under baseline conditions,

THZ1 showed no significant effect on NRVM size, *Nppa/Nppb* expression, or cell death (Figures 4.1B-D and Supplemental Figure 4.1B). As a critical negative control, we used THZ1-R, an inactive structural analog of THZ1 with minimal kinase inhibitory activity⁴. THZ1-R did not affect cellular hypertrophy, *Nppa/Nppb* induction, or Pol II CTD phosphorylation (Supplemental Figures 4.1C-E). To validate for our findings using THZ1, we also assessed the anti-hypertrophic effect of the small molecule probe YKL-1-116²⁷ (Supplemental Figure 4.2A), which has substantially lower potency against CDK12/13. YKL-1-116 inhibited cellular hypertrophy and *Nppa/Nppb* induction but required concentrations 50-100 fold higher than THZ1 (Supplemental Figures 4.2B-C)²⁷. These data suggest that potent and combined inhibition of CDK7/12/13 is required for maximal suppression of the hypertrophic stress response in cardiomyocytes.

To provide orthogonal validation for the on-target molecular pharmacology of THZ1 in our experimental system, we utilized specific siRNA probes to individually knockdown *Cdk7*, *Cdk12*, or *Cdk13* as well as triple-knockdown (TKD) of all three kinases (Supplemental Figure 4.3). We found that individual knockdown of *Cdk7*, *12*, or *13* did not consistently attenuate cardiomyocyte hypertrophy, *Nppa* and *Nppb* induction, and Pol II CTD hyperphosphorylation with the same potency of THZ1, indicating that depletion of a single kinase did not fully recapitulate the robust effects of THZ1 (Supplemental Figure 4.3E-F). In contrast, triple knockdown of *Cdk7/12/13* potently attenuated PE-induced hypertrophy, *Nppa/Nppb* expression, and Pol II CTD hyperphosphorylation in a manner that more closely approximated the effects of THZ1 (Figure 4.1E-H). The increased abundance of these specific Pol II phosphoforms during agonist stimulation and its decrease with

CDK7/12/13 inhibition using THZ1 or siRNA confirms that the combined activity of these kinases is specifically increased during hypertrophic stress in cardiomyocytes. Together, our complementary data using chemical probes and RNAi establish a role for CDK7/12/13 as druggable transcription co-activators and positive regulators of pathological cardiomyocyte hypertrophy.

To enhance relevance to human HFrEF, we ascertained whether CDK7/12/13 inhibition with THZ1 could also block pathologic remodeling in human cardiomyocytes. We tested the effects of THZ1 in human induced pluripotent stem cell–derived cardiomyocytes (iPSC-CMs), a well-validated in vitro experimental platform to study human cardiomyocyte stress signaling, using an iPSC line derived from a healthy human donor [iCell Cardiomyocytes, Cellular Dynamics International Inc. (CDI)]²⁸. Previous studies have demonstrated that these cells mount a hypertrophic response to 10nM endothelin-1 (ET-1)^{28,29}. We found that THZ1 attenuated ET-1–mediated hypertrophic growth in human iPSC-CMs in a dose-dependent manner (Figures 4.1I-J) with an IC₅₀ ~10nM, a potency that paralleled our rodent cardiomyocyte data. Consistent with the effects on cellular hypertrophy, qRT-PCR demonstrated that THZ1 suppressed transactivation of *NPPB/BNP* (Figure 4.1K) and other typical marker genes induced in human iPSC-CMs during ET-1 stimulation (Supplemental Figure 4.4A)²⁸. Quantitative enzyme-linked immunosorbent assay (ELISA) confirmed that THZ1 attenuated the ET-1–stimulated secretion of N-terminal pro-BNP protein, a widely used clinical biomarker for human HFrEF (Figure 4.1L).

THZ1 alters gene expression and transcription in NRVM during hypertrophic stress

We next performed RNA-Seq in NRVM to profile the genome wide transcriptional mechanisms underlying the protective effects of THZ1 (Figure 4.2A, Supplementary Data 1). Hierarchical clustering revealed six distinct gene expression patterns, with approximately one-fourth of all expressed genes falling into cluster 5, representing genes induced by PE stimulation and robustly suppressed with THZ1 co-treatment, such as *Nppa*, *Nppb*, and *Xirp2/Myomaxin* (Figure 4.2B). THZ1 also attenuated the PE-mediated downregulation of a subset of genes (cluster 2), further suggesting that primary inhibition of stress-gene transactivation can shift the transcriptome towards the basal state. While THZ1 had no major effect on cardiomyocyte growth or viability at baseline (Figures 4.1B-D and Supplemental Figure 4.1B), there was a subset of genes for which THZ1 altered baseline expression (clusters 1 and 3). Gene ontology analysis for each cluster is provided in Supplementary Data 2.

Given the role of CDK7/12/13 as activators of Pol II and the robust ability of THZ1 to suppress stress-induced cardiomyocyte hypertrophy, we focused our attention on PE-mediated gene transcription by performing ChIP-Seq for total Pol II in NRVM after 48 hours of PE-stimulation. Representative gene tracks for the *Nppa/Nppb* locus (Figure 4.2C) showed that PE-stimulation increased gene body enrichment of Pol II, consistent with stress-activated transcription of these genes. THZ1 attenuated enrichment of Pol II at the *Nppa* and *Nppb* loci, consistent with inhibition of gene transcription. Genome-scale quantification of Pol II density at this 48-hour time point revealed that THZ1 led to a modest increase in Pol II accumulation at transcription start sites (Figure 4.2D), a finding

that suggests a net effect of impaired transcription elongation at this late time point. We assessed the Pol II traveling ratio (defined here as the ratio of Pol II occupancy at the TSS over the gene body; Figure 4.2E), a widely used indicator of genome-scale transcription elongation^{30,31}, for genes regulated by THZ1 during PE-mediated stress. THZ1 elicited a rightward shift in the Pol II traveling ratio curve, also suggesting a net effect of THZ1 in attenuating Pol II elongation in pathologically stressed cardiomyocytes after 48 hours of PE stimulation (Figure 4.2E). These ChIP-Seq data are consistent with the biochemical data demonstrating CDK7/12/13 inhibition blocks stress-dependent accumulation of bulk Pol II Ser2P abundance (Figure 4.1D and F), a post-translational modification indicative of elongating Pol II.

We note that Pol II ChIP-seq in primary cultured neonatal cardiomyocytes, which was performed under experimental conditions that are required for robust agonist-induced hypertrophic responses (low plating density and prolonged serum starvation), did not provide signal robustness that would allow us to make reliable correlations between locus-specific Pol II enrichment and differential gene expression by RNA-seq. Furthermore, we cannot exclude a primary and rapid effect of THZ1 on Pol II initiation, which can influence subsequent rates of Pol II elongation and is an event in the transcription cycle that likely occurs at much earlier timepoints after agonist stimulation compared to the 48-hour time point used in this experiment. Together, these in vitro data support that CDK7/12/13 are cell-autonomous effectors of transcription activation during cardiomyocyte stress and that CDK7/12/13 inhibition attenuates hallmark features of pathologic cardiomyocyte remodeling.

THZ1 improves cardiac function and inhibits a maladaptive gene expression program in a mouse model of heart failure

Our findings in cultured cardiomyocytes prompted us to test whether interdicting CDK7/12/13-dependent transcription using THZ1 could block HFrEF pathogenesis in vivo. We subjected mice to transverse aortic constriction (TAC), a widely used surgical model of left ventricle (LV) pressure overload and progressive HFrEF³², with administration of THZ1 (20 mg/kg/day, intraperitoneally) or vehicle for 60 days (Figure 4.3A). This THZ1 dose has been validated to provide target coverage and efficacy in murine tumor xenograft studies and is generally well tolerated in mice^{4,6,25}, allowing us to test for proof-of-concept in vivo in the context of HFrEF, with the caveat that detailed toxicological analysis has not yet been reported for this chemical probe. We found that THZ1 attenuated several hallmark features of adverse cardiac remodeling and HFrEF pathogenesis including LV systolic dysfunction (Figures 4.3B-C and Supplemental Figure 4.4B), cardiomegaly (Figures 3D-E), LV wall thickening (Supplemental Figure 4.4C), LV cavity dilation (Supplemental Figure 4.4D), cardiomyocyte hypertrophy (Figure 4.3F), and LV fibrosis (Figure 4.3G). THZ1 had no significant effect on cardiac mass, cardiac structure or LV function in the sham group (Figure 4.3E, Supplemental Figures 4.4 B-D). In addition, THZ1 had no effect on body weight (Supplemental Figure 4.4E), consistent with the general tolerability of this compound that has been observed in mouse cancer xenograft studies. THZ1 did not affect systolic or diastolic blood pressure in mice (Supplemental Figures 4.4E-G), suggesting that its salutary effect in HFrEF pathogenesis was not simply due to modulation of systemic blood pressure.

To confirm on-target bioactivity in vivo, we performed Western blotting for Pol II CTD phosphorylation from LV tissue samples. TAC led to increased abundance of Pol II Ser2P and Ser7P, which were both attenuated by THZ1 (Supplemental Figure 4.4H), supporting that cardiac CDK7/12/13 activity is increased during stress and blocked by THZ1 in vivo.

Next, we performed RNA-Seq from LV tissue in each experimental group (Figure 4.4A). PCA clustering showed an overlap of Sham-Veh and Sham-THZ1 groups (Figure 4.4B), revealing that intermittent THZ1 exposure at the doses used here had minimal effect on the transcriptome of non-diseased hearts. This finding is consistent with the observation that THZ1 treatment did not alter cardiac mass, cardiac structure or LV systolic function in the sham group (Figure 4.3). TAC-mediated stress shifted the cardiac transcriptome along PC1, and the major effect of THZ1 treatment during TAC was to revert the gene expression profile back towards the sham group along PC1 (Figure 4.4B). These shifts along PC1 encompassed a broad program of stress-induced genes whose upregulation was blunted by THZ1 (Figure 4.4C), including canonical markers of human HFrEF such as *Nppa*, *Nppb*, *Ctgf*, and *Rcan1* (Figure 4.4D). We identified a set of 800 genes that were upregulated during TAC, of which 401 genes (50%) were significantly suppressed by THZ1 (Figure 4.4E and Supplementary Data 4.3). This gene set showed strong enrichment for functional terms representing several pathological processes that are hallmarks of human HFrEF (Supplemental Figure 4.5A)³³, including cellular growth/anabolism, matrix remodeling, inflammation/fibrosis, and reactivation of striated muscle developmental programs. These findings were corroborated by gene set enrichment analyses, which showed that the THZ1-suppressed gene program was

strongly enriched for targets of EGFR, IL6 and TGF- β signaling (Supplemental Figure 4.5B). Together, these data demonstrate that THZ1 can blunt stress-dependent transcription in the heart and suppress hallmark features of pathologic cardiac remodeling and HFrEF progression in vivo.

Systemic THZ1 administration affects gene expression in multiple cell compartments in the failing mouse heart

While our in vitro data in primary rodent and human iPSC-derived cardiomyocytes support a cardiomyocyte-intrinsic effect of CDK7/12/13 inhibition, we recognize that administration of THZ1 in vivo may simultaneously act on multiple cell compartments that populate the stressed heart, including cardiomyocytes. Our bulk RNA-seq from adult mouse LV tissue suggests that THZ1 affects genes expressed in both cardiomyocytes and non-cardiomyocyte compartments during TAC. To better understand the relative responsiveness of various myocardial cellular compartments to THZ1 treatment during TAC, we curated two published single cell transcriptomic datasets from adult mouse hearts^{34,35} to generate a cellular atlas (Figure 4.4F-G) that allows for compartment-specific “fingerprinting” of our bulk RNA-seq data from LV tissue. Using the set of 401 genes identified to be upregulated in TAC and suppressed with THZ1 treatment in our bulk LV tissue RNA-seq, we cross-referenced these transcripts against our clustered single cell reference dataset to extrapolate the specific cellular compartments from which these dynamically responsive transcripts originated (Figure 4.4G; cell compartment specific heatmaps shown in Supplementary Figure 4.6). Consistent with our cell culture studies, we observed a clear cardiomyocyte signature demarcated by canonical HF-

associated genes (*Ankrd1*, *Xirp2*, *Nppa*, *Nppb*). We also detected a robust signature of genes that were differentially expressed during TAC and sensitive to THZ1 that originated from resident cardiac fibroblasts, particularly the group of *Periostin*-positive cells that demarcate the myofibroblast subpopulation. Other cell compartments in the adult mouse heart that were sensitive to THZ1 included epicardial, endothelial and endocardial cells. Taken together, these results suggest that THZ1 exerts protective effects in the TAC model by inhibiting CDK7/12/13-dependent cell state transitions across cardiomyocyte and non-cardiomyocyte cellular compartments.

Discussion

Collectively, the data presented here demonstrate that CDK7/12/13 activity is a critical effector of stress-dependent cardiac transcription and HFrEF pathogenesis. Using the first-in-class inhibitor THZ1, we provide proof of concept that transcription inhibition can exert effects on the heart during HFrEF pathogenesis in vitro and in vivo. Our in vitro data using chemical inhibitors and siRNA are consistent with a mechanism where CDK7, 12 and 13 have non-overlapping functions in the transcription cycle in cardiomyocytes. In this manner, multi-CDK inhibition of CDK7, 12 and 13 using THZ1 or siRNA is likely exerting additive or synergistic effects on cardiac stress responses by impairing their multiple, non-overlapping functions in the transcription cycle, supporting the concept that inhibition of all three kinases is required to consistently and potently suppress adverse cardiac remodeling. Future studies using cardiovascular cells harboring a CDK7 cysteine substitution allele (Cys312Ser) that is resistant to covalent chemical inhibitors like THZ1 (or equivalent cysteine substitution alleles for CDK12/13), will also help dissect the non-

overlapping functions of these three kinases in cardiac stress responses. While THZ1 can suppress agonist induced hypertrophy in cultured cardiomyocytes, our transcriptomic profiling of adult mouse hearts demonstrates that the protective effects of THZ1 in vivo are associated with dynamic gene expression changes in both cardiomyocyte and non-cardiomyocyte compartments. Often, dissecting the causality of cell-specific contributions during heart failure pathogenesis can be interrogated using conditional gene deletion approaches. However, modeling the pharmacology of THZ1 in vivo using conditional gene-deletion approaches will be particularly challenging because it would likely require simultaneous postnatal deletion of multiple loci (*Cdk7*, *Cdk12* and *Cdk13*). Furthermore, it is expected that gene deletion in any one cellular compartment would only give a partial protection from heart failure pathogenesis and that simultaneous CDK7/12/13 inhibition in multiple cell types, as occurs with THZ1, is required for full therapeutic effects. Finally, in contrast to the intermittent and dose-titratable effects of a chemical probe like THZ1, permanent gene deletion of these 3 kinases may not be as well tolerated. While there are certainly caveats to interpreting the cell compartment and gene-specific effects of THZ1 in vivo, this study highlights some of the advantages of probing disease pathobiology using chemical biological tools.

Previous studies demonstrated that the CDK9/P-TEFb complex played an important role in cardiac hypertrophy². Using pleiotropic chemical inhibitors such as **5,6**-dichloro-**1**- β -D-ribofuranosylbenzimidazole (DRB) or flavopirodol or via adenoviral overexpression of a dominant-negative CDK9 construct, CDK9 inhibition was shown to attenuate cardiomyocyte hypertrophy and Pol II hyperphosphorylation in cultured neonatal rat

cardiomyocytes in vitro. In addition, cardiomyocyte-specific transgenic overexpression of Cyclin-T1, a key component of the CDK9-activating complex, was sufficient to drive pathological cardiac hypertrophy in mice in vivo. These seminal findings suggested a role for the CDK9/PTEF-b transcriptional complex in cardiac hypertrophy, although the therapeutic potential of Pol II kinase inhibition could not be assessed due to lack of potent and specific chemical probes that were suitable for in vivo administration. Interestingly, adenoviral overexpression of a dominant negative CDK7 construct was also shown to modestly attenuate agonist-induced protein synthesis in cultured cardiomyocytes², suggesting parallel approaches to interdict transcription during cardiomyocyte stress responses. Our study demonstrates that simultaneous inhibition of CDK7-, 12- and 13-dependent transcription is required for potent and consistent antihypertrophic responses and establishes proof-of-concept that CDK7/12/13 inhibition using THZ1 can ameliorate pressure overload induced heart failure in adult mice.

Our finding that THZ1 can also suppress pathologic remodeling in human iPSC-CMs at low nanomolar concentration supports the concept that manipulating stress-mediated transcriptional signaling might be an approach to limit adverse cardiac remodeling during human HFREF pathogenesis. However, we acknowledge that systemic exposure to molecules such as THZ1 may have on-target toxicity in extracardiac organs, including effects on neuronal plasticity³⁶ and possibly in highly proliferative tissue compartments such as the intestinal epithelium or bone marrow. Given the generally high bar for safety required for chronically dosed cardiovascular therapeutics, future studies detailing the on-target liabilities of CDK7/12/13 inhibition and the precise cell compartments mediating

therapeutic efficacy will be required to refine such a strategy in the treatment of heart failure. In contrast to several cancer drugs that cause cardiotoxicity³⁷, our data suggest that molecules like THZ1 may be a privileged class of anticancer therapeutics that have cardioprotective properties. More broadly, this work supports the contention that HFrEF pathogenesis, like cancer, features a general dependency on transcription that might be therapeutically exploited.

Figures

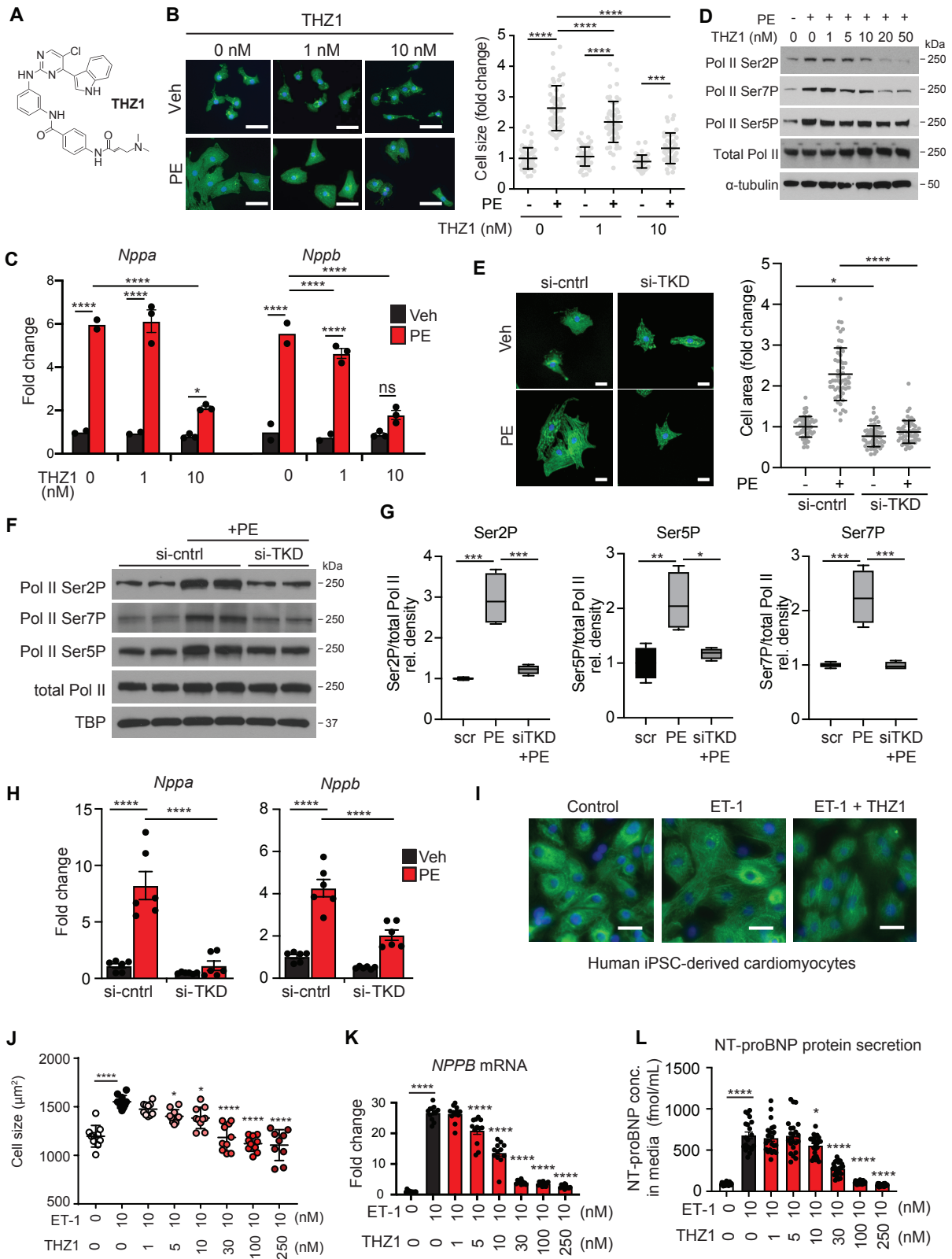


Figure 4.1. CDK7/12/13 inhibition attenuates hallmark features of pathologic cardiomyocyte remodeling in vitro (A) Chemical structure of THZ1. (B) Representative image of NRVM treated \pm THZ1 (at indicated concentrations) and PE (100 μ M) for 48h with cell area quantification (n=50-55 randomly selected cells per condition). Scale bar: 30 μ m. Bars denote mean \pm SD. ***p = .0002. (C) Quantification of expression levels of indicated genes from real-time PCR (n=3 for THZ1 1nM+PE, and THZ1 10nM+PE groups; n=2 for THZ1 0nM+PE and THZ1 1nM -PE). Experiment was repeated three independent times with similar results. (D) Representative Western blots of NRVM with indicated treatment for specific targets. N=3 independent experiments. Pol II phosphoforms and total Pol II were each probed from a separately run gel and membrane, with each lane loaded with an equivalent amount of total protein and lysate volume, derived from a common master stock of protein lysate for each designated condition. The loading control (α -tubulin) was probed on the same blot with Pol II Ser7P. For these Western blots, NRVM were harvested 30 min after exposure to PE. (E) Representative images of NRVM treated \pm si-control (si-cntrl) or si-*Cdk7/12/13* (TKD) and PE (100 μ M) for 48h with cell area quantification (n=55 randomly selected cells per condition). Scale bar: 30 μ m. Bars denote mean \pm SD. *p = 0.0127. (F) Representative Western blots of NRVM with indicated treatment for specific targets. Pol II phosphoforms and total Pol II were each probed from a separately run gel and membrane, with each lane loaded with an equivalent amount of total protein and lysate volume, derived from a common master stock of protein lysate for each designated condition. The loading control (TBP) was probed on the same blot with Pol II Ser7P. For these Western blots, NRVM were harvested 30 min after exposure to PE. Experiment was repeated three independent times with similar results. (G) Densitometry of Western blots in Figure 1F. (n=4 per condition). Box plots show center line as median, whiskers show maxima and minima, and box limits show upper and lower quartiles. ***p = 0.0002 for Ser2P: scr vs. PE, ***p = 0.0004 for Ser2P: PE vs. siTKD + PE, **p = 0.0048 for Ser5P: scr vs. PE, *p = 0.0131 Ser5P: PE vs siTKD + PE, ***p = 0.0006 for Ser7P: scr vs PE, ***p = 0.0005 for Ser7P: PE vs siTKD + PE. (H) Quantification of expression levels of indicated genes from real-time PCR (n=4). (I and J) Representative hiPSC-CM images (alpha-actinin staining in green and DAPI in blue) and quantification of cell size for indicated treatments (n=10 for all conditions except ET-THZ1-250nM for which n=9). Each data point represents the mean cell area for a single cell-culture chamber. For each chamber, 25 cells were randomly selected for area quantification. Scale bar: 30 μ m. Bars denote mean \pm SD. Significance values represent comparisons against the group that was exposed only to ET-1 (10nM). *p = 0.0395 for ET vs. ET-THZ1-5nM, *p = 0.0133 for ET vs. ET-THZ1-10nM. (K) Gene expression levels of *NPPB* in hiPSC-CM with indicated treatments (n=10). Significance values represent comparisons against the group that was exposed only to ET-1 (10nM). (L) Protein concentration of secreted NT-proBNP in hiPSC-CM in the culture medium (n=10). Significance values represent comparisons against the group that was exposed only to ET-1 (10nM). *p = 0.0281 for ET vs ET-THZ1-10nM. Data are shown as means \pm SEM unless otherwise noted. *p < 0.05, **p < 0.01, ***p < 0.001, ****p < 0.0001 for all indicated comparisons. One-way ANOVA with Tukey's multiple comparisons test was used for all statistical analyses. Exact p values are noted when possible.

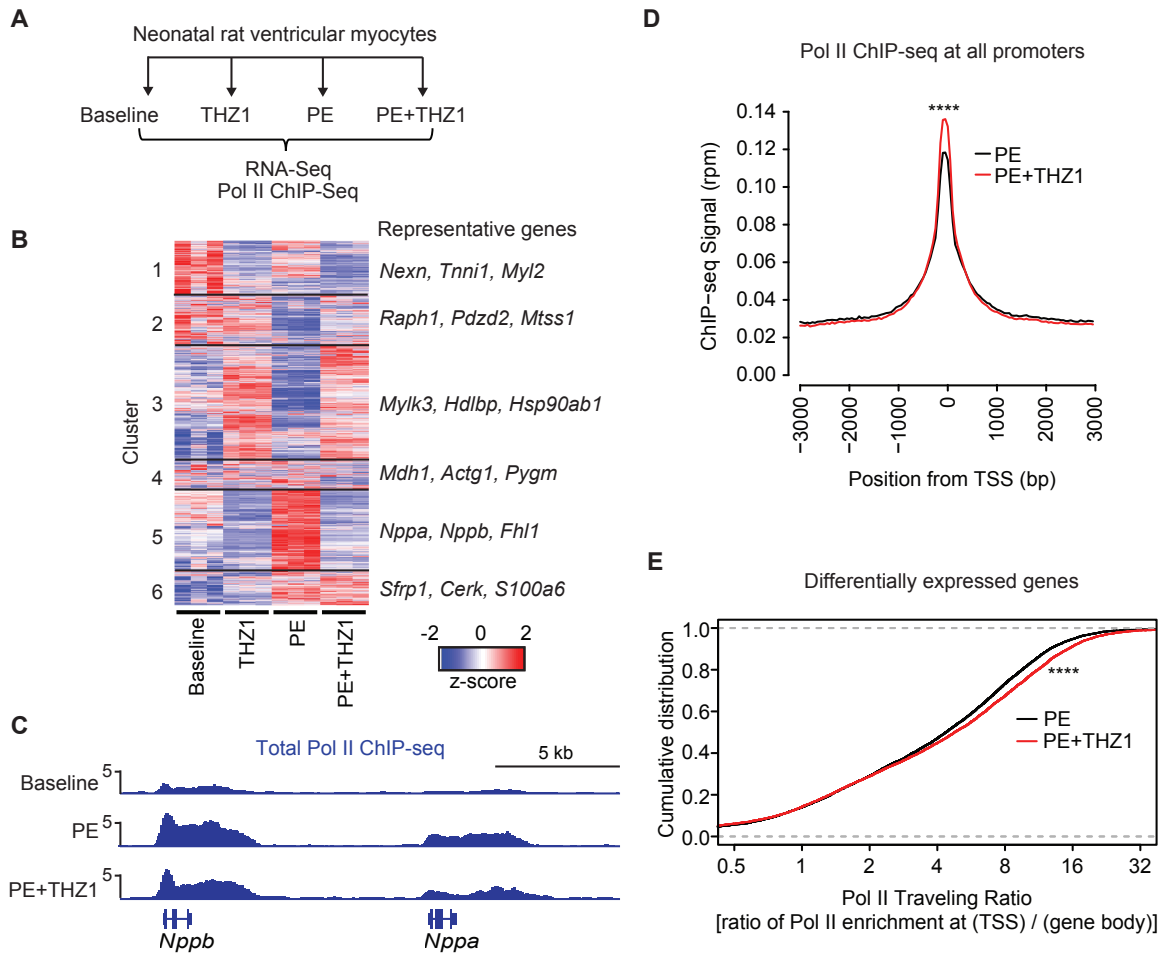


Figure 4.2. THZ1 blocks stress-responsive gene programs and Pol II enrichment in cultured cardiomyocytes. (A) Schema of the experimental design. ChIP-seq for total Pol II was performed for 3 conditions: baseline, PE, and PE+THZ1. **(B)** A heatmap showing clustered, row-normalized global gene expression profile in each sample in the indicated treatment group (n=3) with representative gene callouts. **(C)** Representative gene tracks of Pol II enrichment for canonical hypertrophic marker genes (*Nppb* and *Nppa*). **(D)** Accumulative Pol II occupancy on all promoters. **(E)** Empirical cumulative distribution plots of Pol II traveling ratios (TR) for genes that are differentially expressed in response to PE stimulation (PE vs baseline). TR is defined as the ratio of (Pol II signal at TSS) / (Pol II signal at gene body). **** $p < 0.0001$ for indicated comparisons.

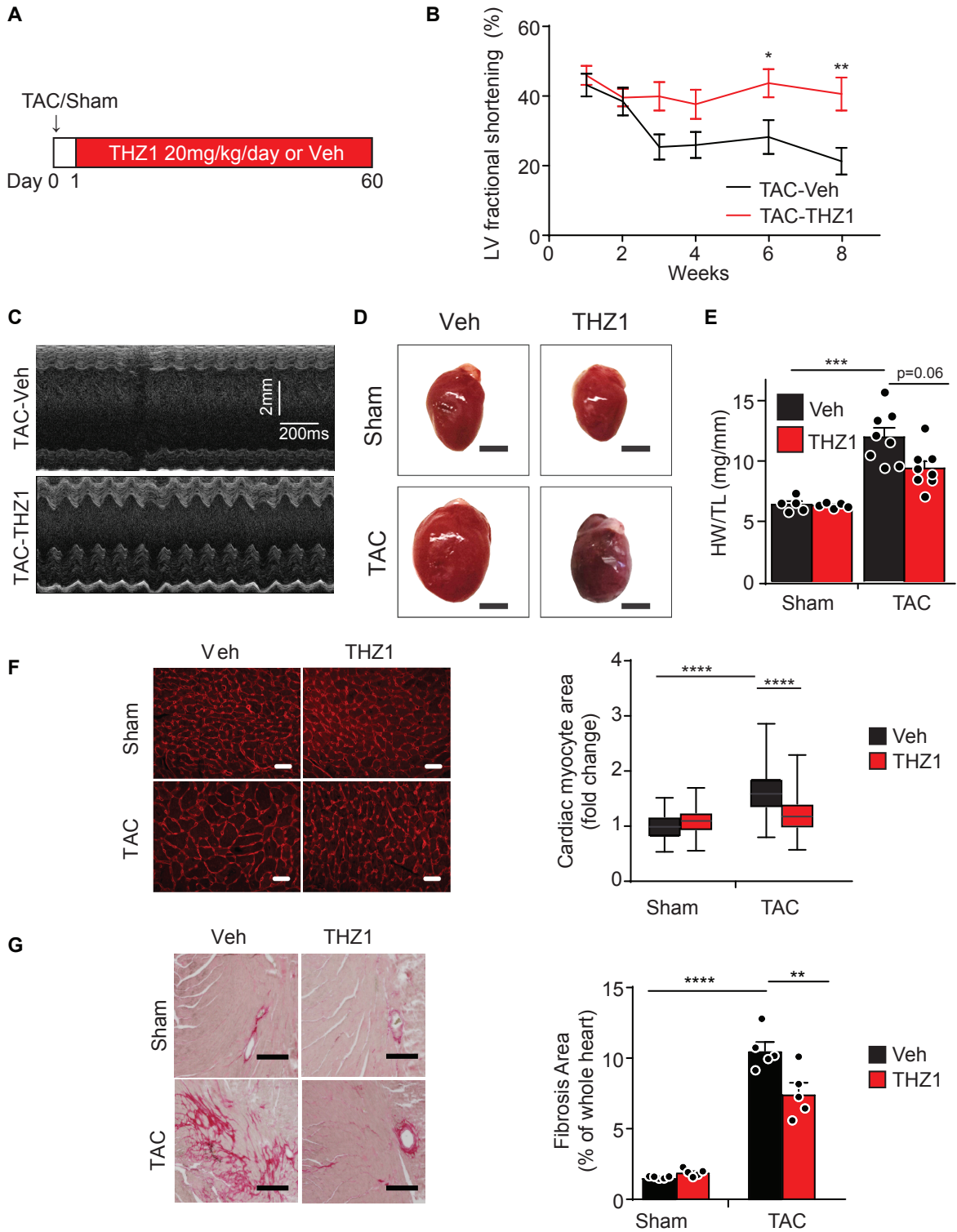


Figure 4.3. THZ1 ameliorates cardinal features of adverse cardiac remodeling and HFrEF pathogenesis in mice. (A) Schema of the experimental design. **(B)** Two-dimensional echocardiographic quantification of left ventricle area fractional shortening in indicated groups (n=8). Echocardiography for the sham groups (Sham-Veh and Sham-THZ1) were performed at the end of the study (week 8) and are plotted alongside the week 8 TAC data in Supplemental Figure 4A-C. * $p = 0.0339$, ** $p = 0.0039$. Two-way ANOVA with Holm-Sidak multiple comparisons correction was used for statistical analysis. **(C)** Representative M-mode echocardiographic images obtained at mid-papillary muscle level from parasternal short-axis view (8 weeks post-TAC). **(D-E)** Representative heart images and quantification of heart weight/tibial length (HW/TL) ratio at 8 weeks post-TAC. Scale bar: 3 mm. **(F)** Representative images of myocardium visualized by wheat germ agglutinin staining (red) and quantification of cardiomyocyte cross sectional area in indicated groups at 8 weeks post TAC (pooled analysis of 150 individual cardiomyocytes randomly selected from hearts of 3 independent animals per experimental condition). Scale bar: 20 μm . Data presented as standard box-and-whisker plots showing median cardiomyocyte area (horizontal line). Upper and lower quartiles are designated by the box and whiskers designate upper and lower extremes. **(G)** Representative heart cross sections stained with picosirius red with quantification of fibrosis area in indicated groups (n=5; 8 weeks post-TAC). ** $p = 0.0027$. Scale bar: 200 μm . * $p < 0.05$, ** $p < 0.01$, *** $p < 0.001$, **** $p < 0.0001$ for all indicated comparisons. Data are shown as means \pm SEM unless otherwise noted. One-way ANOVA with Tukey's multiple comparisons test was used for all statistical analyses unless noted. Exact p values are noted when possible.

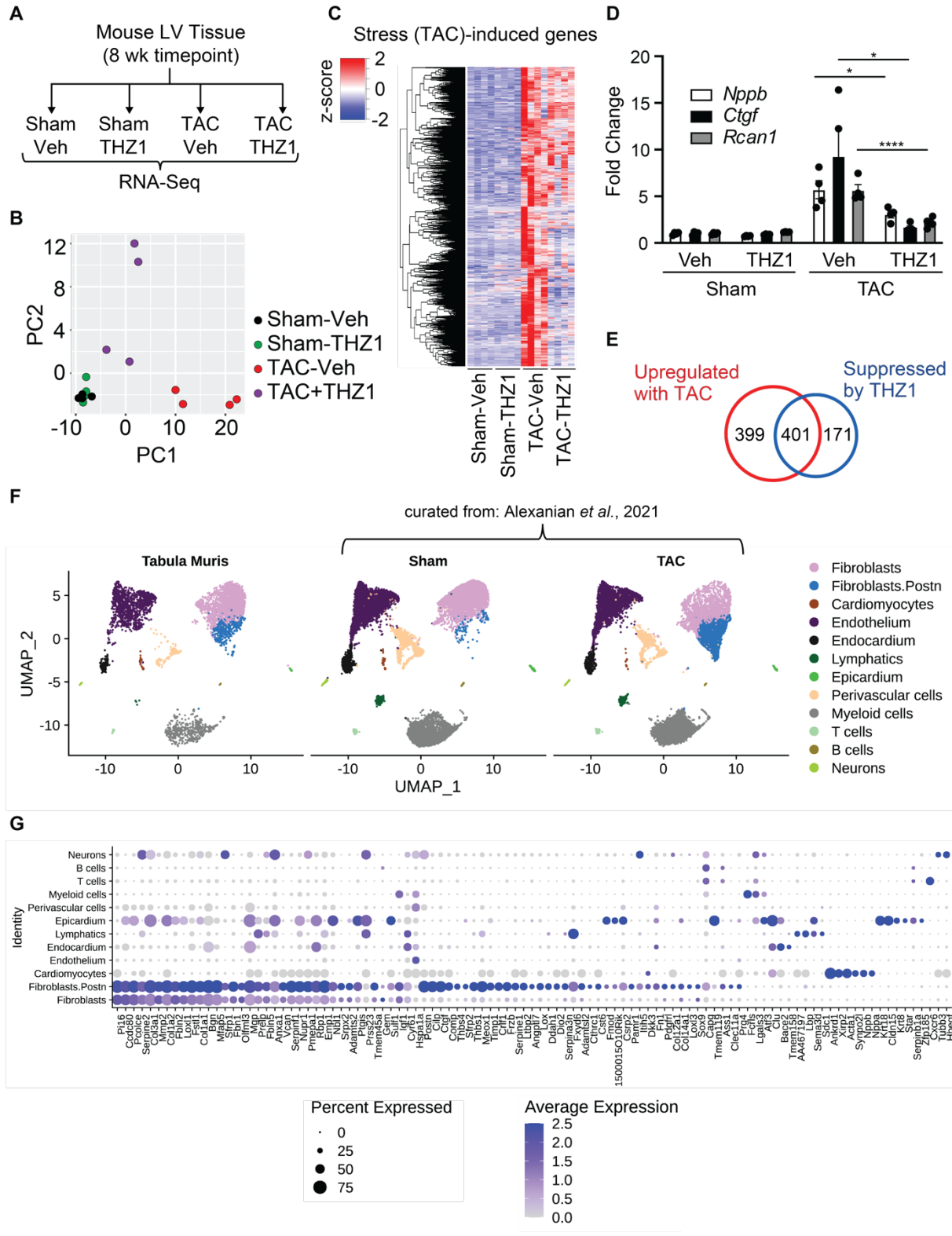
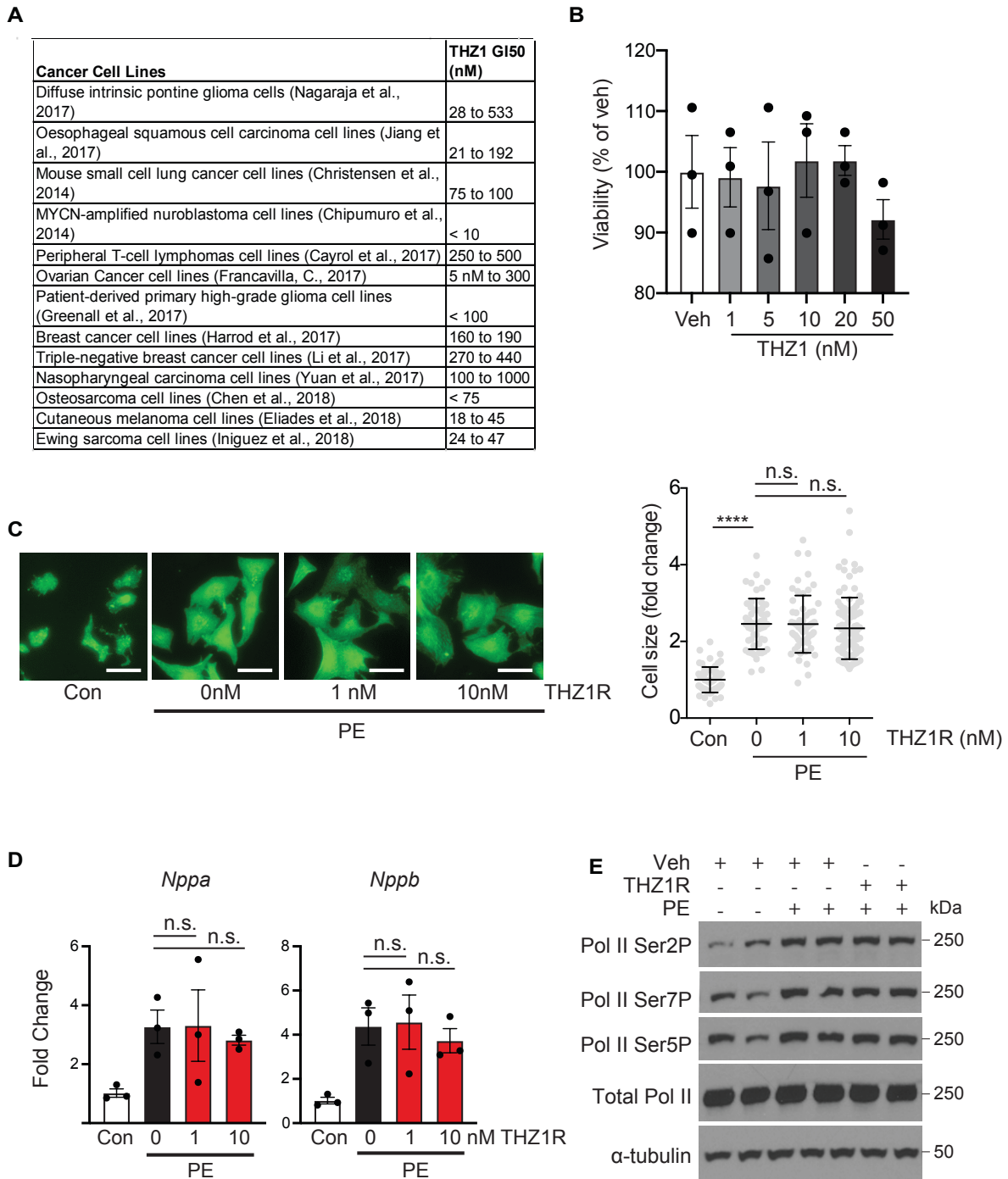
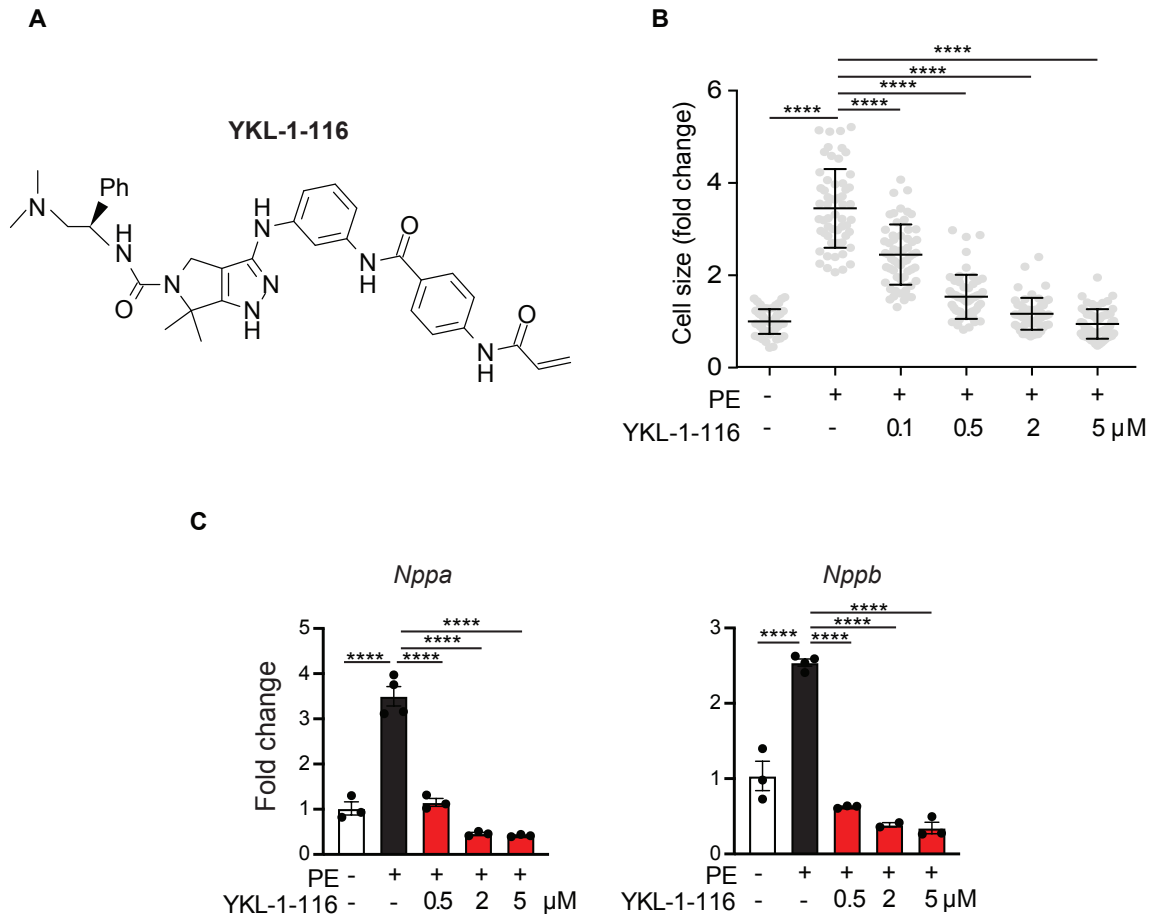


Figure 4.4. THZ1 ameliorates specific pathological gene programs in diverse cardiac cellular compartments in failing mouse hearts. (A) Schema of the experimental design. **(B)** Principal component (PC) analysis showing global gene expression in indicated samples. **(C)** A heatmap showing clustered, row-normalized stress induced gene expression profile in each sample in indicated group (n=4). **(D)** Gene expression levels of indicated representative genes (n=4) calculated from normalized DeSeq2 counts. Significance levels were based on the adjusted p-values reported by DeSeq2. Bars denote mean \pm SD. * $p = 0.0171$ for Nppb: TAC-Veh vs TAC-THZ1, * $p = 0.0178$ for Ctgf: TAC-Veh vs TAC-THZ1. **(E)** Venn diagram demonstrating number of differentially expressed genes in each indicated compartment (cutoffs are specified in Methods section). * $p < 0.05$, **** $p < 0.0001$ for all indicated comparisons. **(F)** UMAP (Uniform Manifold Approximation and Projection) projection of cardiac cell compartments in mouse heart identified by integrating two public mouse heart datasets (n = 32,407 cells). Each dot represents a single cell. Different cell-type clusters are color-coded. **(G)** Gene expression distribution of cell-type enriched genes whose expression is increased with TAC and suppressed by THZ1 (in E) across cell compartments in adult mouse heart. Genes that were induced with TAC and suppressed by THZ1, as determined by bulk RNA sequencing, were cross-referenced with the integrated single cell dataset (in F) to determine the most likely cell type compartment from which each transcript originated. The size of the dot indicates the percentage of cells with at least one compartment-defining transcript detected and the color of the dot represents the scaled average expression level of expressing cells. Representative heatmaps for differentially expressed genes emanating from each identified cell compartment are shown in Supplementary Figure 6. One-way ANOVA with Tukey's multiple comparisons test was used for all statistical analyses. Exact p values are noted when possible.

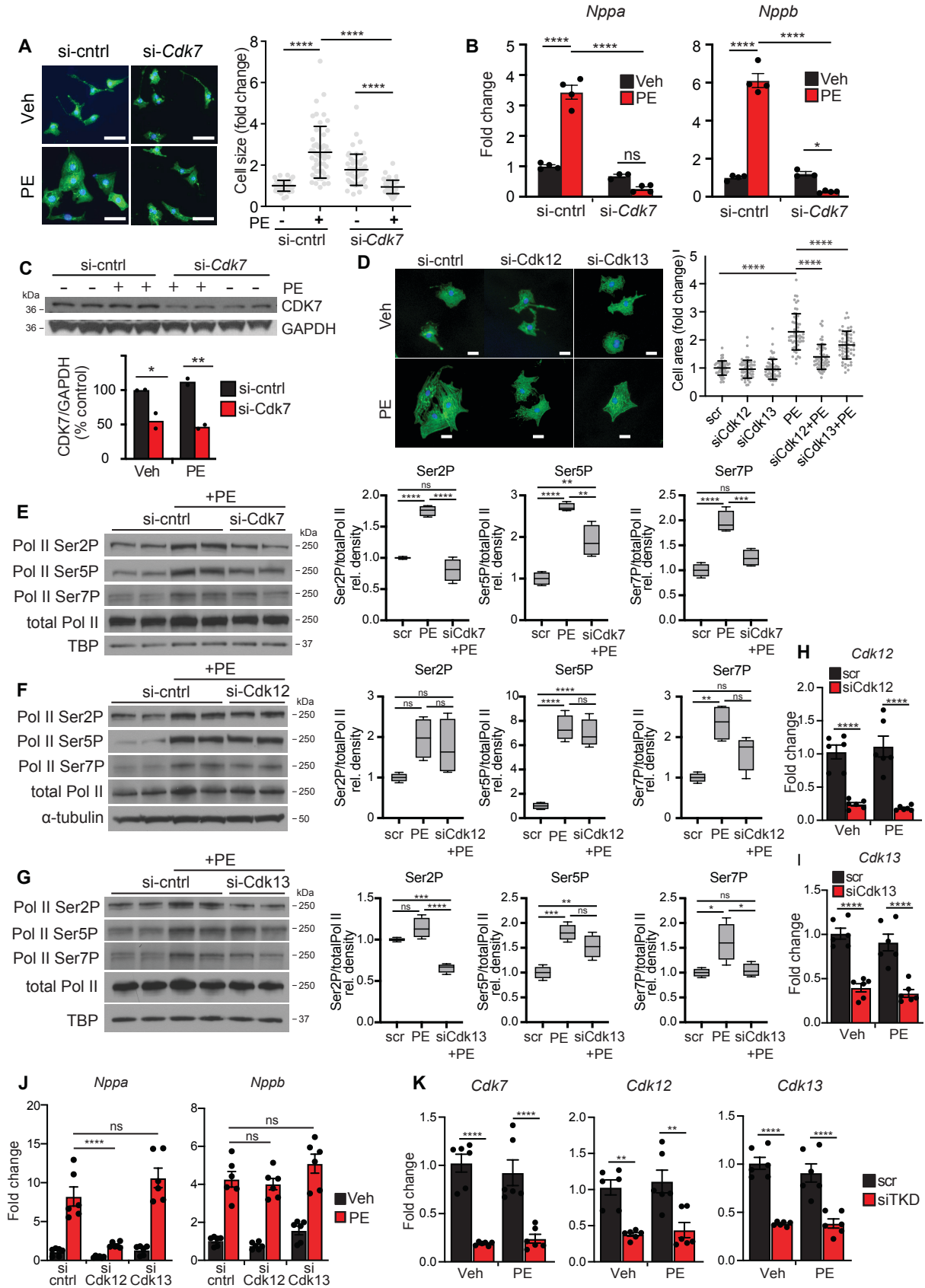


Supplementary Figure 4.1. Effects of THZ1 and THZ1-R. (A) Summary of THZ1 concentrations causing 50% cell growth inhibition (GI₅₀) for indicated cancer cell types. These data have been curated from published literature and summarized here. **(B)** Trypan blue staining for indicated doses of THZ1 (n=3). **(C)** Representative NRVM image (α -actinin in green) and quantification of cell size with indicated treatments (n=59 cells for control, n=51 cells for PE, n=58 cells for THZ1R-1nM + PE, n=100 cells for THZ1R-10nM + PE). Scale bar: 30 μ m. Bars denote mean \pm SD. **(D)** Quantification of expression levels

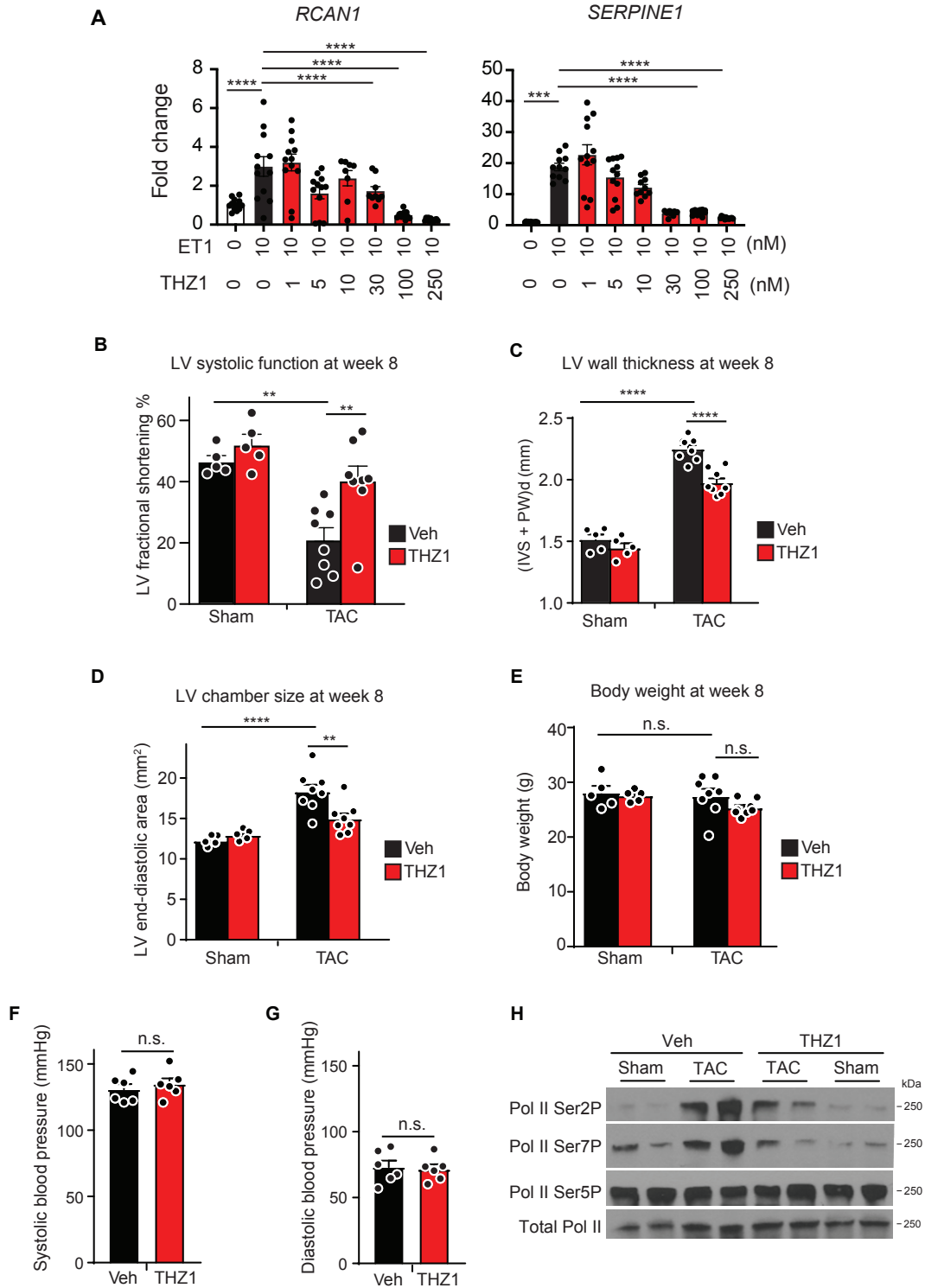
of representative genes (*Nppa* and *Nppb*) with indicated treatments (n=3). **(E)** Representative Western blots of NRVM with indicated treatments for specific targets. Pol II phosphoforms and total Pol II were each probed from a separately run gel and membrane, with each lane loaded with an equivalent amount of total protein and lysate volume, derived from a common master stock of protein lysate for each designated condition. The loading control (α -tubulin) was probed on the same blot with Pol II Ser7P. For these Western blots, NRVM were harvested 30 min after exposure to PE. Experiment was repeated three independent times with similar results. **** $p < 0.0001$, not significant (n.s., $p > 0.05$) for indicated comparisons. Data are shown as means \pm SEM unless otherwise noted. One-way ANOVA with Tukey's multiple comparisons test was used for all statistical analyses. Exact p values are noted when possible.



Supplementary Figure 4.2. YKL-1-116 inhibits agonist-induced hypertrophy in NRVM. (A) Chemical structure of YKL-1-116. **(B)** Quantification of cell area with indicated treatments (n=55-58 randomly selected cells per condition). Bars denote mean \pm SD. **(C)** Gene expression levels of representative genes (Nppa and Nppb) in NRVM with indicated treatments (n=3-4; for Nppb, the YKL 2uM group is n=2). Bars denote mean \pm SEM. ****p < 0.0001 for indicated comparisons. One-way ANOVA with Tukey's multiple comparisons test was used for all statistical analyses. Exact p values are noted when possible.



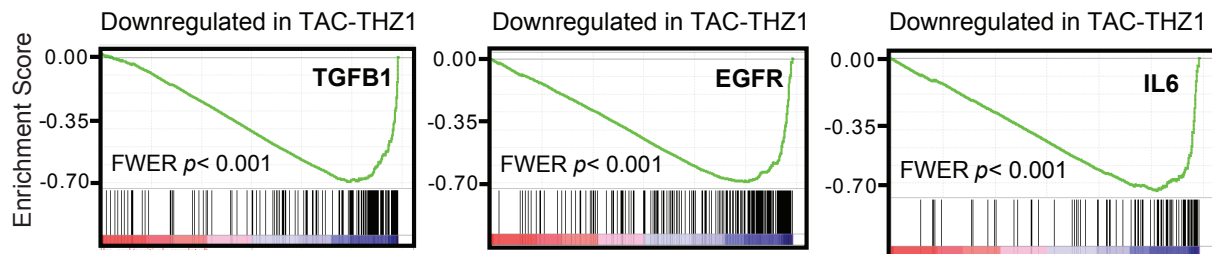
Supplementary Figure 4.3. Effects of si-*Cdk7*, si-*Cdk12*, si-*Cdk13*, and si-TKD (triple knock down) (A) Representative images of NRVM treated \pm si-control (si-cntrl) or si-*Cdk7* and PE (100 μ M) for 48h with cell area quantification (n=40 cells for si-cntrl, n=51 cells for si-cntrl+PE, n=57 cells for si-*Cdk7*, n=53 cells for si-*Cdk7*+PE). Scale bar: 30 μ m. Bars denote mean \pm SD. (B) Quantification of expression levels of indicated genes from real-time PCR (n=3-4). Scale bar: 30 μ m. (C) Representative western blot of NRVM with indicated treatments for the specific targets and quantification of CDK7/GAPDH ratio (n=2). The loading control (GAPDH) was probed on a separate blot from CDK7. Experiment was repeated three independent times with similar results. (D) Representative images of NRVM treated \pm si-control (si-cntrl), si-*Cdk12*, or si-*Cdk13* and \pm PE (100 μ M) for 48h with cell area quantification (n=55 randomly selected cells per condition). Scale bar: 30 μ m. Bars denote mean \pm SD. The experiment for single knockdown of *Cdk12*+PE and *Cdk13*+PE shown here was performed as part of the same experiment for triple knockdown (TKD) of *Cdk7/12/13*+PE that is shown in main Figure 1E. Therefore, these experiments share the exact same control groups for si-cntrl+PE. The representative image and area quantification for the si-cntrl+PE conditions are duplicated here from Figure 1E, as they appropriately serve as the same control groups for these two figures. The panels for triple knockdown were separated and placed into the main Figure 1E to provide clarity during the description of the Results section. (E-G) Representative Western blots of NRVM with indicated treatment for specific targets. Quantification is shown on the right (N=4) with data shown as box plots with error bars representing SD. Pol II phosphoforms and total Pol II were each probed from a separately run gel and membrane, with each lane loaded with an equivalent amount of total protein and lysate volume, derived from a common master stock of protein lysate for each designated condition. The loading control (TBP or α -tubulin) was probed on the same blot with Pol II Ser7P. For these Western blots, NRVM were harvested 30 min after exposure to PE. Box plots show center line as median, whiskers show maxima and minima, and box limits show upper and lower quartiles. **p = 0.0017 for siCdk7 (Ser5P): Scr vs. siCdk7 + PE, **p = 0.0033 for siCdk7 (Ser5P): PE vs siCdk7 + PE, ***p = 0.0008 for siCdk7 (Ser7P): PE vs siCdk7 + PE. **p = 0.0016 for siCdk12 (Ser7P): scr vs PE, ***p = 0.0005 for siCdk13 (Ser2P): scr vs. PE, ***p = 0.0004 for siCdk13 (Ser5P): scr vs PE, **p = 0.0067 for siCdk13 (Ser5P): scr vs siCdk13+PE, *p = 0.0151 for siCdk13 (Ser7P): scr vs PE, *p = 0.0232 for siCdk13 (Ser7P): PE vs siCdk13 + PE. Experiments were repeated three independent times with similar results. (H-K) Quantification of expression levels of indicated genes from real-time PCR (n=6). **p = 0.0021 for Cdk12: scr vs siTKD, **p = 0.0016 for Cdk12: PE vs siTKD + PE. Data are shown as means \pm SEM unless otherwise noted. One-way ANOVA with Tukey's multiple comparisons test was used for all statistical analyses. Exact p values are noted when possible. *p < 0.05, **p < 0.01, ***p < 0.001, ****p < 0.0001, not significant (n.s., p > 0.05) for all indicated comparisons.



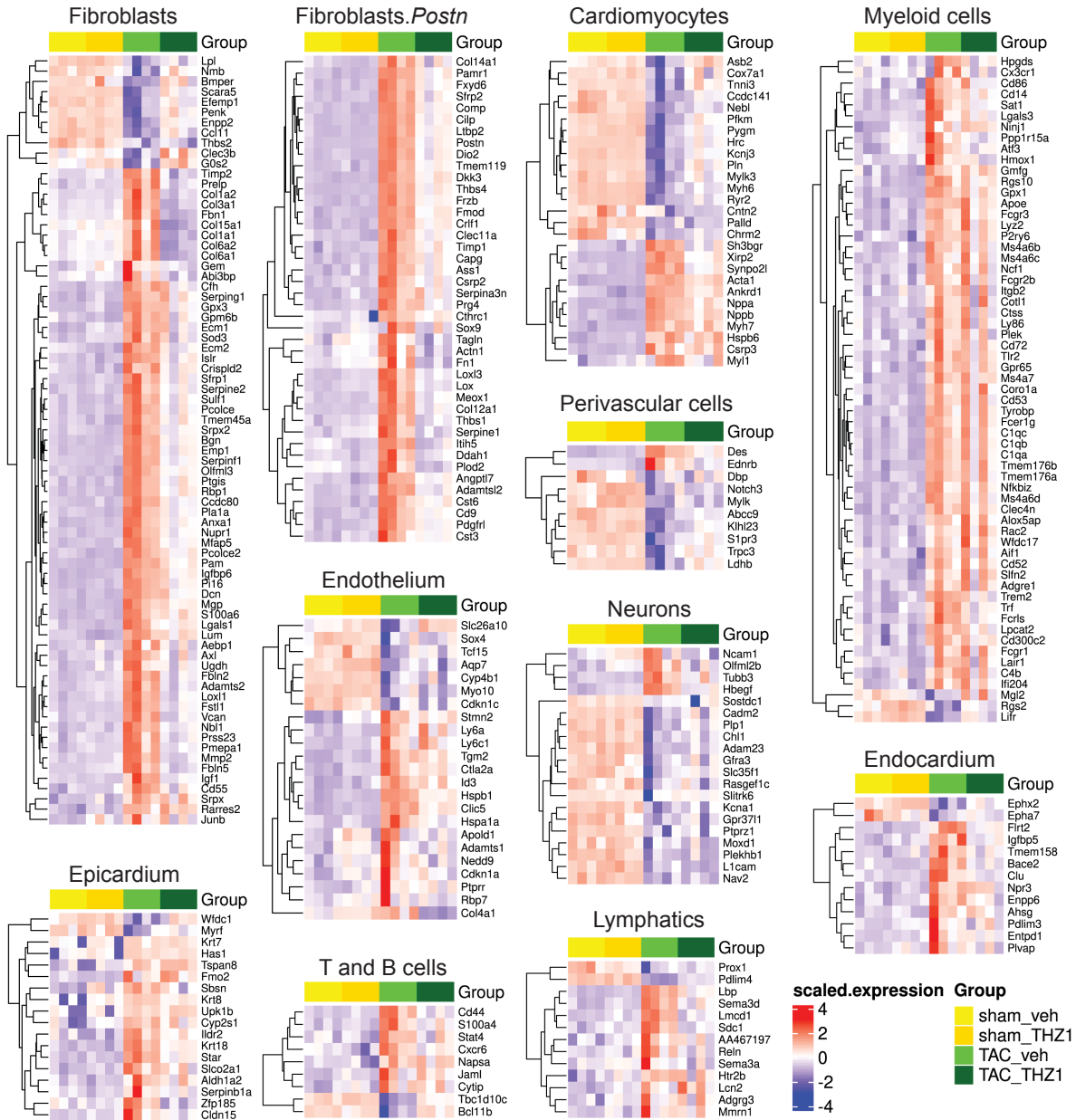
Supplementary Figure 4.4. Effects of THZ1 on hypertrophic marker gene expression in hiPSC-CM and physiological parameters in mice. **(A)** Expression levels of representative genes (SERPINE1 and RCAN1) in hiPSC-CM with indicated treatments (n=12 independent samples for RCAN1: baseline, ET1, THZ1-1nM, THZ1-5nM, THZ1-100nM, THZ1-250nM, n=8 independent samples for RCAN1: THZ1-10nM, n=9 independent samples for RCAN1: THZ1-30nM, n=12 independent samples for SERPINE1: baseline, THZ1-1nM, THZ1-5nM, THZ1-100nM, THZ1-250nM, n=11 independent samples for SERPINE1: ET1, n=10 independent samples for SERPINE1: THZ1-10nM, n=9 independent samples for SERPINE1: THZ1-30nM). ***p = 0.0002. **(B)** Two-dimensional echocardiographic LV area fractional shortening at week 8 post-TAC (n=5 sham; n=8 TAC). **p = 0.0018 for Sham-Veh vs TAC-Veh, **p = 0.0064 for TAC-Veh vs TAC-THZ1. **(C)** Wall thickness as expressed as sum of interventricular septum (IVS) and posterior wall (PW) thickness at week 8 post-TAC (n=5 sham; n=8 TAC). **p = 0.0064 **(D)** Left ventricular (LV) end-diastolic area at mid-papillary muscle level at week 8 post-TAC (n=5 sham; n=8 TAC). **(E)** Body weight at week 8 post TAC (n=5 sham; n=8 TAC). **(F)** Systolic blood pressure in mice treated chronically with THZ1 (n=6). **(G)** Diastolic blood pressure in mice treated chronically with THZ1 (n=6). **(H)** Representative Western blot of heart ventricle tissue with indicated treatment for indicated targets. Samples were harvested 60 days after TAC. Pol II phosphoform and total Pol II were each probed from a separately run gel and membrane, with each lane loaded with an equivalent amount of total protein and lysate volume, derived from a common master stock of protein lysate for each designated condition. Experiment was repeated three independent times with similar results. **p < 0.01, ****p < 0.0001, not significant (n.s., p > 0.05) for indicated comparisons. Data are shown as means ± SEM unless otherwise noted. One-way ANOVA with Tukey's multiple comparisons test was used for all statistical analyses. Exact p values are noted when possible.

A

| Category | Term | % List | FDR(%) |
|------------------|---|--------|----------|
| UP_KEYWORDS | Extracellular matrix | 13.70 | 5.91E-32 |
| KEGG_PATHWAY | mmu04151:PI3K-Akt signaling pathway | 4.96 | 1.54E+00 |
| GOTERM_MF_DIRECT | GO:0005178~integrin binding | 3.79 | 3.08E-03 |
| GOTERM_MF_DIRECT | GO:0008083~growth factor activity | 4.66 | 4.19E-05 |
| INTERPRO | IPR015615:Transforming growth factor-beta-related | 1.75 | 7.69E-02 |
| GOTERM_MF_DIRECT | GO:0005125~cytokine activity | 3.21 | 4.22E-01 |
| KEGG_PATHWAY | mmu04350:TGF-beta signaling pathway | 2.33 | 2.20E+00 |
| GOTERM_BP_DIRECT | GO:0030199~collagen fibril organization | 3.21 | 1.33E-05 |
| GOTERM_BP_DIRECT | GO:0001501~skeletal system development | 2.92 | 2.35E-01 |
| INTERPRO | metalloproteinases-like, OB-fold | 1.46 | 2.10E+00 |

B

Supplementary Figure 4.5. THZ1 inhibits specific gene programs in the adult mouse heart. (A) Gene ontology analysis using DAVID for the set of 401 genes that were TAC-inducible and suppressed by THZ1. A false discovery rate (FDR; shown as percent) of < 5% was considered statistically significant. (B) Gene set enrichment analysis (GSEA) showing down-regulation of TGFB1, IL6 and EGFR signatures in the set of genes that were upregulated by TAC and suppressed by THZ1.



Supplementary Figure 4.6. Differential gene expression from bulk RNA-seq for TAC vs. sham conditions, binned into indicated cellular compartments (related to Figure 4F-G.). Gene signatures of various cellular compartments determined by curating published single cell RNA-seq datasets from the adult mouse heart. Heatmaps show the expression of genes differentially expressed in TAC-veh vs. sham-veh for all four experimental conditions (sham-veh, sham-THZ1, TAC-veh, TAC-THZ1). Heatmaps are generated for each of the following cellular compartments: fibroblasts, Periostin-positive fibroblasts (*Fibroblasts.Postn*), cardiomyocytes, endothelium, myeloid cells, endocardium, perivascular cells, epicardium, T cells, B cells, lymphatics, and cardiac neurons (fold change less than 0.67-fold or more than 1.5-fold, Benjamini-Hochberg adjusted $p < 0.05$).

Materials and Methods

All research studies performed in this study were compliant with the Institutional Animal Care and Use Committees at University of California San Francisco and Case Western Reserve University and conducted in strict accordance with the National Institutes of Health Guide for the Care and Use of Laboratory Animals³⁸

Animal models

Studies were conducted with age matched male C57Bl/6J mice (The Jackson Laboratory, catalog no. 000664). Mice were housed in a temperature- and humidity-controlled pathogen-free facility with 12-hour light/dark cycle and ad libitum access to water and standard laboratory rodent chow.

Chemical Probes

THZ1, THZ1-R and YKL-1-116, all of which have been previously described^{4,27}, were generously provided by Nathanael Gray's lab.

Mouse models of cardiac hypertrophy and heart failure

All mice were male C57Bl/6J mice aged 10 to 11 weeks from The Jackson Laboratory. Mice were placed on a temperature-controlled small-animal surgical table to help maintain body temperature (37°C) during surgery. Mice were anesthetized with 1-3% isoflurane, mechanically ventilated (Harvard Apparatus), and subjected to thoracotomy. To perform transverse aortic artery constriction, aortic arch was exposed and constricted between

the left common carotid and the brachiocephalic arteries using a 7-0 silk suture and a 27-gauge needle as previously described²⁹. Mice in sham group were subjected to the same procedures except the placement of constriction. Daily intraperitoneal injections of vehicle solution (0.15 mL of 10% DMSO and 5% dextrose in water)³⁹ or 20mg/kg THZ1 (dissolved in 0.15 mL of the same vehicle solution) were started on postoperative day 1 until postoperative day 60.

Neonatal rat ventricular myocyte isolation and culture

Neonatal rat ventricular myocytes (NRVMs) were isolated from the hearts of 2-3 day old Sprague-Dawley (Strain #001) rat pups from Charles River and maintained under standard conditions as described previously⁴⁰. After overnight digestion with 0.25% trypsin at 4°C, cells were dissociated from tissue through series of digestion with 300 U/mL collagenase II (Worthington Biochemical Corporation, Lakewood, NJ). The dissociated cells were then pre-plated for 1.5 hours in cell culture dishes followed by 24 hours exposure to BrdU in culture medium to remove contaminating nonmyocytes and inhibit any residual cellular proliferation. Unless otherwise stated, NRVM were plated at a density of 10^5 cells/mL. Cells were initially plated in growth medium (DMEM supplemented with 5% FBS, 100 U/ml penicillin-streptomycin and 2 mM L-glutamine) for 48 hours. Prior to stimulation with agonists or chemical probes, NRVM were maintained in serum-free medium (DMEM supplemented with 0.1% BSA, 1% insulin-transferrin-selenium supplement (Sigma I3146), 100 U/ml penicillin-streptomycin, and 2 mM L-glutamine) for additional 48 hours.

For individual CDK knockdowns, *Cdk7*, *12*, and *13* mRNA were targeted by specific siRNAs (Sigma SASI_Rn02_00333956, SASI_Rn01_00106147, and SASI_Rn02_00272683 respectively) at final concentration of 50nM. For combinatorial triple knockdown of *Cdk7/12/13*, equal concentrations of each siRNA probe were adjusted to maintain a final siRNA concentration of 50nM. Transfection was performed with transfection reagent RNAiMAX (Invitrogen) according to manufacturer's instruction. Control groups were transfected with MISSION siRNA Universal Negative Control #1 (Sigma) at the same final concentration.

For testing effects of small molecule probes in the hypertrophic response, NRVM were incubated with vehicle (DMSO) or inhibitors at indicated concentrations for 3 hours followed by stimulation with phenylephrine (PE) (100 μ M) for various durations. For mRNA level and cell size measurements, NRVMs were stimulated with PE for 48 hours. For evaluating phosphorylation level of RNA polymerase II, NRVMs were incubated with PE for 30 minutes before harvesting.

Human iPSC-CMs culture, qRT-PCR, and BNP enzyme-linked immunosorbent assay (ELISA)

Human induced pluripotent stem cell-derived cardiomyocytes (iCell cardiomyocytes) were purchased from FUJIFILM Cellular Dynamics, Inc. and maintained according to manufacturer's instructions. IRB review was not required. Cells were seeded on 96-well culture plates coated with 5 μ g/mL of fibronectin and maintained in Williams' E Medium supplemented with 1:25 of Cell Maintenance Cocktail B (Thermo Fisher Scientific, CM4000). For subsequent hypertrophic stimulation, quiesced iPSC-CMs were treated

with or without THZ1 at indicated concentrations versus DMSO for 3 hours followed by stimulation with either vehicle or 10 nM endothelin-1 (Sigma) for 18 hours. The complementary DNA was directly synthesized from RNA in cell lysate using the TaqMan Gene Expression Cells-to-CT kit (Thermo Fisher Sci AM1728) according to the manufacturer's instruction. qRT-PCR for human *NPPB* and *B2M* (normalizer) was performed with the Life Technologies TaqMan assays (*NPPB*, Hs00173590_m1; *B2M*, Hs000984230_m1). qRT-PCR for other human genes was performed using TaqMan chemistry including FastStart Universal Probe Master (Roche), labeled probes from the Universal ProbeLibrary (Roche), and gene-specific oligonucleotide primers (list of qRT-PCR primers and TaqMAN probes are provided in Supplementary Data 4). Relative expression was calculated using the $2^{-\Delta\Delta C_t}$ method with normalization to *B2M* expression. ELISA for NT-proBNP protein was performed on 6 ml of medium from each well of a 96-well plate as previously published²⁸ using the following antibodies: anti-proBNP capture antibody (clone 5B6; Abcam ab13111), anti-proBNP HRP conjugate detection antibody (clone 16F3; Abcam ab13124), and purified NT-proBNP (Phoenix Pharmaceuticals, catalog no. 011-42) as a standard.

Western blotting

To extract total cellular protein, cells were lysed in RIPA Buffer (Sigma R0278) supplemented with protease inhibitor (Roche cat. no. 4693132001) and phosphatase inhibitor (Phos-STOP; Roche, 04 906 845 001) tablets. Nuclear protein was isolated using the NE-PER Nuclear and Cytoplasmic Extraction Reagents (Thermo Scientific, 78833) according to manufacturer's instructions. For each sample, 20–50 μ g protein extracts

were separated by 8-12% Bis-Tris gels (Fisher Sci, NW04122BOX), transferred to nitrocellulose membranes. To ensure uniform protein loading for each antibody signal, all protein samples were prepared as a single batch that was adjusted to the same total protein concentration and pre-boiled in loading buffer. Western blots were run by loading equal volumes of this lysate prep to achieve uniform total protein mass and volume loading in each lane. As we were detecting multiple RNA Pol II phosphoforms which run at overlapping mobility from the same sample, determination of signal by serial stripping and reprobing of each membrane did not provide appropriate fidelity for reliable signal discrimination. Therefore, in most cases, Westerns were performed for the various Pol II phosphoforms on individually run gels and membranes. The specific membrane from which the loading control was run is designated for each Western panel in the figure legend. Specific targets were detected with following antibodies: CDK7 Antibody (C-19) (Santa Cruz sc-529) or CDK7 Antibody (C-4) (Santa Cruz sc-7344), alpha-tubulin (Sigma T9026), RNA Polymerase II (1F4B6) (Active Motif 61667), Ser2P RNA Pol II (Abcam, ab5095) or Ser2P RNA Pol II (3E10) (EMD Millipore, 04-1571), Ser5P RNA Pol II (3E8) (EMD Millipore, 04-1572), Ser7P RNA Pol II (4E12) (EMD Millipore, 04-1570).

Immunocytochemistry and immunohistochemistry

Cultured cells: NRVMs were seeded on glass coverslips coated with 0.1% gelatin and fixed in 2% paraformaldehyde for 20 minutes at room temperature followed by permeabilization with PBST plus 0.1% Triton X. NRVMs were incubated in PBST plus 5% horse serum for 1 hour and then stained with primary antibody against α -actinin at 1:800 (Sigma-Aldrich, A7811) for 1 hour. NRVMs were washed 3 times with PBST followed by

staining with secondary antibody at 1:1000 for 1 hour. Cells were washed 3 times with PBST and mounted with Vectashield Hardset mounting medium. For human iPSC-derived cardiomyocytes, cells were plated on Ibidi 8-well chamber slides. Cells were fixed in 2% paraformaldehyde for 20 minutes, permeabilized with PBST plus 0.1% Triton X-100 for 20 minutes, and blocked with PBST plus 5% horse serum for 1 hour at room temperature. Primary antibody against sarcomeric α -actinin was used at a dilution of 1:800 in PBST plus 5% horse serum for 1 hour at room temperature. Secondary anti-mouse antibody was used at a dilution of 1:1000 in PBST plus 5% horse serum for 1 hour at room temperature. Cell area for NRVM and human iPSC-derived cardiomyocytes was quantified from immunofluorescent images as previously described²⁹.

Mouse heart tissue samples: Mouse hearts were harvested, dried and weighed. Tissue was fixed in 10% neutral-buffered formalin overnight at 4°C and transferred to 100% ethanol for 24 hours. Samples were embedded in paraffin blocks, sectioned, and stained with Picrosirius red (Polysciences) or Wheat Germ Agglutinin 488 (Thermo Fisher Scientific, W11261) according to the manufacturers' instructions. Images were captured by fluorescence microscopy, bright field microscopy or high-content imaging platform (IN Cell Analyzer, GE Healthcare Systems) as previously described²⁹. For cardiomyocyte cross sectional area from WGA-rhodamine stained LV tissue samples, we quantified area of 50 randomly selected cardiomyocytes per heart from 3 randomly chosen fields at 200x magnification (from tissue sectioned from the mid-papillary region in the LV short-axis), using Image J. This was repeated in 3 different hearts for each experimental group, leading to a total of 150 individual cardiomyocyte cross-sectional area measurements that were pooled for each experimental condition. Quantification of LV fibrosis from picrosirius

red stained heart tissue sections was performed in 5 independent hearts per experimental group as previously described²⁹.

Echocardiography and blood pressure measurements

For transthoracic echocardiography, mice were anesthetized with 1-2% isoflurane and imaged using Vevo 770 Imaging System (Visual Sonics, Inc.) with RMV-707B probe. Measurements were obtained from M-mode sampling and integrated electrocardiogram-gated kilohertz visualization (EKV) images taken in the LV short axis at the mid-papillary level to generate high spatiotemporal resolution two-dimensional images. LV areas and ejection fraction were obtained from high-resolution two-dimensional measurements at end-diastole and end-systole²⁹.

Non-invasive blood pressure was measured using the BP2000 Blood Pressure Analysis System (Visitech Systems, Inc.) according to manufacturer's instruction. Mice received chronic injections of vehicle or THZ1 (20 mg/kg/day) injections for 1 week. During this period, mice were trained on the Visitech system to enable accurate, standardized BP measurements. Blood pressure was recorded at 24 hours after the most recent injection on 3 different days for each mouse. Data were then pooled and analyzed.

RNA isolation and qPCR

Total RNA was isolated from NRVM using the High Pure RNA isolation kit (Roche 11828665001) with on-column DNAase treatment according to manufacturer's

instruction. For RNA isolation from mouse tissue, a 10–20 mg piece of mouse heart ventricles was mechanically homogenized in PureZOL RNA isolation reagent (Bio-Rad 7326890) on a TissueLyser II (QIAGEN 85300) using stainless steel beads (QIAGEN 69989). Total RNA was purified using the Aurum total RNA purification kit (Bio-Rad 732-6830). The purified total RNA was then reverse transcribed to complementary DNA with iScript RT supermix (Bio-Rad 170-8841) according to manufacturer's instruction. A list of qRT-PCR primers and TaqMAN probes are provided in Supplemental Table 3. Relative expression was calculated using the $2\Delta\Delta C_t$ method with normalization to constitutive genes. Mouse data were normalized to *Ppib*.

Library preparation and next-generation sequencing for RNA-Seq

RNA isolated from tissue and cells were quantified using Qubit fluorometric quantitation and assessed for quality using Agilent Bioanalyzer Nano RNA Chip. Samples with RNA integrity

number larger than 8 were considered high-quality and suitable for RNA-seq. Library preparation was performed using the Illumina TruSeq Stranded mRNA kit or KAPA mRNA HyperPrep Kit (Roche), and the library was sequenced on an Illumina HiSeq 2500 at the Genomics Core Facility of Whitehead Institutes (single-end, 40 base pairs, >50 M reads per sample).

RNA-seq data processing and quantification

Each RNA-Seq sample was aligned independently. Specifically, the raw RNA-Seq reads from each sample were aligned with TopHat v2.1.1 with options “-p 8 -r 300 --library-type

fr-firststrand --no-coverage-search". Each sample was aligned either against the mm9 or rn5 reference genome as appropriate for the sample.

After alignment, the number of mapped reads per gene per sample using *htseq-counts* was quantified. Each application of *htseq-counts* was run with the following options: "-s reverse -f bam". Each sample was quantified against the GENCODE mm9 transcript reference or the UCSC rn5 transcript reference, depending on the source of the sample.

The differentially expressed genes were identified by DeSeq2. The quantifications from *htseq-count* were imported into DeSeq2, and all samples from the same organism were analyzed together in one analytical run. Replicate samples were grouped by their type (e.g., baseline, THZ1-treated) in order to better estimate the sample-level variance for comparison across samples. The standard DeSeq2 workflow followed without modifications, and Benjamin-Hochberg correction was used to control false discovery of differentially expressed genes.

Principal component plots were generated from a matrix of the normalized counts from DeSeq2. Normalized counts were re-centered and scaled per sample prior to the analysis in order to standardize each sample. Heatmaps were generated from the normalized DeSeq2 counts. After row-scaling, individual rows were clustered using hierarchical clustering using a Euclidean distance metric and Ward's clustering. Bar graphs were generated using calculated fold changes of expression of representative genes from DeSeq2 and the adjusted *p*-values reported by the software. The numbers of genes in the Venn diagram were generated using adjusted *p*-value < 0.05 (5% FDR) and Log2 fold change ≥ 1 for comparison between TAC-Veh group vs Sham-Veh group, and adjusted *p*-value < 0.05 (5% FDR) and Log2 fold change ≤ -0.89 for comparison between TAC-

Veh group vs TAC-THZ1 group. For the TAC samples, the fold change cutoff of ≤ -0.89 was chosen to capture differential expression of *Nppb* between TAC-veh vs. TAC-THZ1 in this n=4 sample set, so as to maintain a threshold that appropriately captured a known positive control gene.

DAVID (v.6.8)⁴¹ was used to identify enriched functional annotations in differentially expressed gene ID lists relative to the set of "expressed" genes, defined as having sufficient normalized counts for DESeq2 to calculate a differential expression *p* value, or versus all annotated genes.

For gene set enrichment analysis (GSEA), command line GSEA2 (v.2.2.2, ref.5) was used with MSigDB v.6.1 gene sets⁴⁰. Values were pre-ranked by log₂ fold change, retaining the absolute maximum change per gene where multiple transcripts were assessed. Significance was expressed as family-wise error rate (FWER). FWER *p* < 0.250 represents statistically significant enrichment.

Chromatin immunoprecipitation, library preparation and next-generation sequencing

For ChIP experiments, NRVM were plated in 15 cm dishes at 4×10^6 cells/dish. Chromatin derived from a total of 15 million cells were used for each immunoprecipitation. After indicated treatments, cells were crosslinked with 1% formaldehyde for 10 min at room temperature followed by quenching with 0.125M glycine for 5 min. Cells were then lysed and chromatin was extracted. Isolated chromatin was subjected to shearing with Bioruptor (Diagenode) for 16 cycles (30sec on and 30 sec off/cycle) at high intensity. Small volume of sheared chromatin (50 μ L) from each was stored at -80 °C as input. The

rest of sheared chromatin was then incubated with 5mg RNAPII antibody (clone 8WG16, BioLegend 920102 lot B217159) with 50uL Dynabeads (Invitrogen) overnight at 4 °C. Chromatin was washed, eluted and reverse crosslinked overnight at 65 °C. Genomic DNA was purified from both immunoprecipitated samples and input samples. The library was prepared with TrueSeq ChIP kit (Illumina), and the library was sequenced on an Illumina HiSeq 2500 at the Genomics Core Facility of Whitehead Institutes (single-end, 40 base pairs, >50 M reads per sample).

ChIP-Seq data processing

Each ChIP-Seq sample was processed and aligned using bowtie 1. Each sample was aligned against the rn5 reference genome using bowtie with options “-k 1 -m1”. All gene track and ChIP-seq quantifications were normalized by the number of (uniquely) mapped reads to estimate the “reads per million” (rpm) quantity. Gene track displays were made with Integrative Genome Viewer (IGV).

All density plots for Pol II were made using all rn5 gene promoters based on the rn5 UCSC transcription annotation. Each density plot estimated the average Pol II ChIP-seq signal per promoter within a +/- 5kb window.

Traveling ratios for genes that are differentially expressed genes were estimated as previously described³¹. The PE-responsive differentially expressed genes used in traveling ratio analysis were identified in RNA-Seq data analysis by comparing the PE group to baseline group with an adjusted *p*-value cut-off of 0.1 (10% FDR).

Dissecting the gene expression changes elicited by THZ1 in diverse cardiac cellular compartments by comparing our bulk RNA-seq data with published scRNA-Seq datasets.

To dissect compartment-specific gene expression changes from our bulk RNA-seq data from LV tissue of THZ1-treated mice in the TAC model, scRNA-Seq data performed independently by our group in the mouse TAC model (TAC and sham groups were used) using 10X Genomics were curated from Alexanian *et al.*³⁴. To recover more comprehensive cardiac cell types, including adult cardiomyocytes, and to increase the sensitivity of gene detection, we also downloaded and curated mouse heart scRNA-Seq by Smart-seq2 from the Tabula Muris cohort³⁵. These two scRNA-seq datasets were filtered, normalized, and integrated by Seurat (v4.0.0) R package⁴² with canonical correlation analysis. After performing dimensional reduction by Principal Component Analysis (PCA), the top 30 PCAs were used in graph-based clustering based on Louvain with resolution at 0.5, and cluster specific marker genes were identified using the FindAllMarkers function by Wilcoxon Rank Sum test in Seurat. Cell types were determined by cross-referencing with source data papers and human heart atlas references^{34,35,43,44}. Uniform Manifold Approximation and Project (UMAP) was used to visualize the high dimensional cell cluster distribution. Cell type enriched signature genes were identified using the FindAllMarkers function by Wilcoxon Rank Sum test in Seurat. Cell type enriched genes that were differentially expressed in TAC vs Sham by bulk expression analysis were selected for downstream analysis. TAC altered cell type enriched signature genes was visualized in a graphic heatmap using the ComplexHeatmap (v2.6.2) R package⁴⁵.

Statistical analysis

Measurements were taken from distinct samples. Data are reported as mean \pm SEM unless otherwise indicated in the figure legend. Statistical analysis of LV fractional shortening as a function of time was performed by ANOVA with Holm-Sidak correction for multiple comparisons using GraphPad Prism. All other statistical analyses were performed using ANOVA with Tukey's honest significant difference test correction for multiple comparisons using GraphPad Prism. For all analyses, $p < 0.05$ was considered significant. The statistical methods used in the analyses of RNA-seq and ChIP-seq data are detailed separately above.

References

1. Alexanian, M., Padmanabhan, A., McKinsey, T.A. & Haldar, S.M. Epigenetic therapies in heart failure. *J Mol Cell Cardiol* **130**, 197-204 (2019).
2. Sano, M., *et al.* Activation and function of cyclin T-Cdk9 (positive transcription elongation factor-b) in cardiac muscle-cell hypertrophy. *Nature medicine* **8**, 1310-1317 (2002).
3. Sano, M., *et al.* Activation of cardiac Cdk9 represses PGC-1 and confers a predisposition to heart failure. *EMBO J* **23**, 3559-3569 (2004).
4. Kwiatkowski, N., *et al.* Targeting transcription regulation in cancer with a covalent CDK7 inhibitor. *Nature* (2014).
5. Chipumuro, E., *et al.* CDK7 inhibition suppresses super-enhancer-linked oncogenic transcription in MYCN-driven cancer. *Cell* **159**, 1126-1139 (2014).
6. Christensen, C.L., *et al.* Targeting Transcriptional Addictions in Small Cell Lung Cancer with a Covalent CDK7 Inhibitor. *Cancer cell* **26**, 909-922 (2014).
7. Greenall, S.A., *et al.* Cyclin-dependent kinase 7 is a therapeutic target in high-grade glioma. *Oncogenesis* **6**, e336 (2017).
8. Li, B., *et al.* Therapeutic Rationale to Target Highly Expressed CDK7 Conferring Poor Outcomes in Triple-Negative Breast Cancer. *Cancer Res* **77**, 3834-3845 (2017).
9. Jiang, Y.Y., *et al.* Targeting super-enhancer-associated oncogenes in oesophageal squamous cell carcinoma. *Gut* **66**, 1358-1368 (2017).
10. Zeng, M., *et al.* Targeting MYC dependency in ovarian cancer through inhibition of CDK7 and CDK12/13. *Elife* **7**(2018).
11. Simpson, P., McGrath, A. & Savion, S. Myocyte hypertrophy in neonatal rat heart

- cultures and its regulation by serum and by catecholamines. *Circ Res* **51**, 787-801 (1982).
12. Shiekhattar, R., *et al.* Cdk-activating kinase complex is a component of human transcription factor TFIIH. *Nature* **374**, 283-287 (1995).
 13. Serizawa, H., *et al.* Association of Cdk-activating kinase subunits with transcription factor TFIIH. *Nature* **374**, 280-282 (1995).
 14. Liao, S.M., *et al.* A kinase-cyclin pair in the RNA polymerase II holoenzyme. *Nature* **374**, 193-196 (1995).
 15. Sun, X., *et al.* NAT, a human complex containing Srb polypeptides that functions as a negative regulator of activated transcription. *Mol Cell* **2**, 213-222 (1998).
 16. Trigon, S., *et al.* Characterization of the residues phosphorylated in vitro by different C-terminal domain kinases. *J Biol Chem* **273**, 6769-6775 (1998).
 17. Czudnochowski, N., Bosken, C.A. & Geyer, M. Serine-7 but not serine-5 phosphorylation primes RNA polymerase II CTD for P-TEFb recognition. *Nat Commun* **3**, 842 (2012).
 18. Cayrol, F., *et al.* THZ1 targeting CDK7 suppresses STAT transcriptional activity and sensitizes T-cell lymphomas to BCL2 inhibitors. *Nat Commun* **8**, 14290 (2017).
 19. Francavilla, C., *et al.* Phosphoproteomics of Primary Cells Reveals Druggable Kinase Signatures in Ovarian Cancer. *Cell Rep* **18**, 3242-3256 (2017).
 20. Harrod, A., *et al.* Genomic modelling of the ESR1 Y537S mutation for evaluating function and new therapeutic approaches for metastatic breast cancer. *Oncogene* **36**, 2286-2296 (2017).
 21. Nagaraja, S., *et al.* Transcriptional Dependencies in Diffuse Intrinsic Pontine Glioma.

- Cancer cell* **31**, 635-652 e636 (2017).
22. Yuan, J., *et al.* Super-Enhancers Promote Transcriptional Dysregulation in Nasopharyngeal Carcinoma. *Cancer Res* **77**, 6614-6626 (2017).
23. Zhang, Z., *et al.* Preclinical Efficacy and Molecular Mechanism of Targeting CDK7-Dependent Transcriptional Addiction in Ovarian Cancer. *Mol Cancer Ther* **16**, 1739-1750 (2017).
24. Chen, D., *et al.* Super enhancer inhibitors suppress MYC driven transcriptional amplification and tumor progression in osteosarcoma. *Bone Res* **6**, 11 (2018).
25. Eliades, P., *et al.* High MITF Expression Is Associated with Super-Enhancers and Suppressed by CDK7 Inhibition in Melanoma. *J Invest Dermatol* (2018).
26. Iniguez, A.B., *et al.* EWS/FLI Confers Tumor Cell Synthetic Lethality to CDK12 Inhibition in Ewing Sarcoma. *Cancer cell* **33**, 202-216 e206 (2018).
27. Kalan, S., *et al.* Activation of the p53 Transcriptional Program Sensitizes Cancer Cells to Cdk7 Inhibitors. *Cell Rep* **21**, 467-481 (2017).
28. Carlson, C., *et al.* Phenotypic screening with human iPS cell-derived cardiomyocytes: HTS-compatible assays for interrogating cardiac hypertrophy. *J Biomol Screen* **18**, 1203-1211 (2013).
29. Duan, Q., *et al.* BET bromodomain inhibition suppresses innate inflammatory and profibrotic transcriptional networks in heart failure. *Sci Transl Med* **9**(2017).
30. Wade, J.T. & Struhl, K. The transition from transcriptional initiation to elongation. *Curr Opin Genet Dev* **18**, 130-136 (2008).
31. Lin, C.Y., *et al.* Transcriptional amplification in tumor cells with elevated c-Myc. *Cell* **151**, 56-67 (2012).

32. Rockman, H.A., *et al.* Segregation of atrial-specific and inducible expression of an atrial natriuretic factor transgene in an in vivo murine model of cardiac hypertrophy. *Proc Natl Acad Sci U S A* **88**, 8277-8281 (1991).
33. Hannehalli, S., *et al.* Transcriptional genomics associates FOX transcription factors with human heart failure. *Circulation* **114**, 1269-1276 (2006).
34. Alexanian, M., *et al.* A transcriptional switch governs fibroblast activation in heart disease. *Nature* **595**, 438-443 (2021).
35. Tabula Muris, C., *et al.* Single-cell transcriptomics of 20 mouse organs creates a Tabula Muris. *Nature* **562**, 367-372 (2018).
36. He, G., *et al.* Cdk7 Is Required for Activity-Dependent Neuronal Gene Expression, Long-Lasting Synaptic Plasticity and Long-Term Memory. *Front Mol Neurosci* **10**, 365 (2017).
37. Bellinger, A.M., *et al.* Cardio-Oncology: How New Targeted Cancer Therapies and Precision Medicine Can Inform Cardiovascular Discovery. *Circulation* **132**, 2248-2258 (2015).
38. National Research Council, Guide for the Care and Use of Laboratory Animals, 8th edition. *National Academies Press* (2011).
39. Wang, Y., *et al.* CDK7-dependent transcriptional addiction in triple-negative breast cancer. *Cell* **163**, 174-186 (2015).
40. Anand, P., *et al.* BET bromodomains mediate transcriptional pause release in heart failure. *Cell* **154**, 569-582 (2013).
41. Huang da, W., Sherman, B.T. & Lempicki, R.A. Systematic and integrative analysis of large gene lists using DAVID bioinformatics resources. *Nat Protoc* **4**, 44-57 (2009).

42. Hao, Y., *et al.* Integrated analysis of multimodal single-cell data. *Cell* **184**, 3573-3587 e3529 (2021).
43. van Heesch, S., *et al.* The Translational Landscape of the Human Heart. *Cell* **178**, 242-260 e229 (2019).
44. Litvinukova, M., *et al.* Cells of the adult human heart. *Nature* **588**, 466-472 (2020).
45. Gu, Z., Eils, R. & Schlesner, M. Complex heatmaps reveal patterns and correlations in multidimensional genomic data. *Bioinformatics* **32**, 2847-2849 (2016).
46. Duan, Q. & Day, D. RNA-seq analysis evaluating effects of Cdk7 inhibitor THZ1 on responses of NRVM to adrenergic receptor agonist PE. (NCBI GEO, 2022).
<https://www.ncbi.nlm.nih.gov/geo/query/acc.cgi?acc=GSE151253>
47. Duan, Q. & Zhang, T. RNA-seq analysis evaluating effects of Cdk7 inhibitor THZ1 on responses of mouse hearts to TAC. (NCBI GEO, 2022).
<https://www.ncbi.nlm.nih.gov/geo/query/acc.cgi?acc=GSE151254>
48. Duan, Q. & Day, D. RNA polymerase II (RNAPII) ChIP-seq analysis evaluating effects of Cdk7 inhibitor THZ1 on responses of NRVM to adrenergic receptor agonist PE. (NCBI GEO, 2022).
<https://www.ncbi.nlm.nih.gov/geo/query/acc.cgi?acc=GSE151252>

Publishing Agreement

It is the policy of the University to encourage open access and broad distribution of all theses, dissertations, and manuscripts. The Graduate Division will facilitate the distribution of UCSF theses, dissertations, and manuscripts to the UCSF Library for open access and distribution. UCSF will make such theses, dissertations, and manuscripts accessible to the public and will take reasonable steps to preserve these works in perpetuity.

I hereby grant the non-exclusive, perpetual right to The Regents of the University of California to reproduce, publicly display, distribute, preserve, and publish copies of my thesis, dissertation, or manuscript in any form or media, now existing or later derived, including access online for teaching, research, and public service purposes.

DocuSigned by:

Austin Hsu

10E6977602D44F8...

Author Signature

5/27/2022

Date